5-2018

Study of Magnetization Switching in Coupled Magnetic Nanostructured Systems using a Tunnel Diode Oscillator

Mohammad Asif Khan
University of New Orleans

Study of Magnetization Switching in Coupled Magnetic Nanostructured Systems using a Tunnel Diode Oscillator

An Honors Thesis

Presented to the
Department of Physics
of the University of New Orleans

In Partial Fulfillment
of the Requirements for the Degree of
Bachelor of Science, with University High Honors
and Honors in Physics

by
Mohammad Asif Khan

May 2018

University of New Orleans

Honors Thesis

Study of Magnetization Switching in Coupled Magnetic Nanostructured Systems using a Tunnel Diode Oscillator

Author:

Mohammad Asif Khan

Supervisor:

Dr. Leonard Spinu

Acknowledgements

I am eternally indebted to Dr. Spinu for the love, support, and mentorship he has provided to me for the past four years. Under his benevolent guidance I have been able to acquire the knowledge to work on this project and many others. He has been an exemplary role model who was always here for me throughout my undergraduate studies. It is an understatement to say that this thesis would not have been possible without his supervision and leadership.

I would like to thank Dr. Malkinski, Dr. Ioup, Dr. Stokes and, Dr. Puri for providing me the theoretical knowledge via different courses in class and out of class that I was able to use for this thesis. I would like to thank all my teachers and mentors I have had, because they all have a hand in making this possible.

My mentor, peer, and, friend Daniel Adams has been here since day one to assist when I made a mistake and encourage me when I accomplished a task. Dr. Shankar Khanal, whom I consider an elder brother, was part of our team as a PhD student. He has shared invaluable knowledge with me which he gathered through his studies and experience. Other members of our team, Pratik Poudyal, Pemba Sherpa, Dr. Artur Maksymov, and Ali Radmanesh who have provided help with my research or support as needed; I am thankful to them all.

I would also like to thank Paula Roberta Kern for providing us with the exchange bias samples used for this research.

The dean, Dr. Steve Johnson, whose gracious and compassionate program COSURP has funded my research will always have my gratitude. I would also like to thank AMRI, especially Dr John Wiley, Jennifer Nguyen, and Poncho DeLeon. I would also like to thank Mrs Denise Bauer Banks who has been a guardian to me. I will always be grateful for the guidance and love she has provided.

I would like to thank all my family and friends who have supported me through the different phases of my life. Thank you Roshni for always believing in me.

I would like to thank my parents, Sanaullah Khan and Momina Khan more than anyone. I don't know where I would be without you guys and honestly I cannot put in words how grateful I am to be your son.

Table of Contents

List of Figures **v**

Abstract **ix**

Introduction **1**

1 Basic Theories and Principles of Magnetism **5**

1.1 Magnetic Moment 6

1.2 Magnetic Domain 7

1.3 Magnetic Anisotropy 8

1.4 Magnetic Susceptibility 8

1.5 Ferromagnetism 10

1.5.1 Magnetic Hysteresis 12

1.5.2 Coercivity 13

1.6 Antiferromagnetism 14

1.7 Stoner–Wohlfarth Model 16

1.8 Coupled Magnetic Nanostructures 21

2 Equipment for Static Magnetization Switching Measurement **24**

2.1 Vibrating Sample Magnetometer 25

2.2 Tunnel Diode Oscillator 28

2.2.1 Introduction 28

2.2.2 The Tunnel Diode 30

2.2.3 Tunneling Diode Oscillator Setup in the Laboratory 33

2.3 Double Helmholtz Coil 38

2.4 Critical Curves via Reversible Transverse Susceptibility Measurements 41

3 Static Critical Curves of Synthetic Antiferromagnets **44**

3.1 Synthetic Antiferromagnet Concepts 44

3.2 Synthetic Antiferromagnets Samples 47

3.3 Major Hysteresis Loop of SAF 49

3.4 Static Critical Curve of SAF 52

4 Static Critical Curves of Exchange Bias Samples **58**

4.1 Introduction 58

4.2 Exchange Bias Samples 60

4.3 Major Hysteresis Loop of Exchange Bias Samples 62

Conclusions **66**

A Appendix **68**

A.1 Types of Magnetic Material 68

A.2 Thin Films 70

A.3 Timeline of Experiments Based on Tunnel Diode Oscillator 71

A.4 Magnetic Field between Helmholtz coils 75

References **77**

List of Publications **84**

List of Figures

1.1 An illustration of Magnes the shepherd, the (probably mythical) discoverer of natural magnetism. 5

1.2 Magnetic moments of domains before (left) and the aligned magnetic domain after (right) the application of an external magnetic field 11

1.3 A typical hysteresis loop. The broken line is the initial magnetization curve. The downward curve after saturation, along with the lower return curve, form the main loop. 13

1.4 Schematic showing adjacent magnetic dipole moments with equal magnitude aligned anti-parallel in an antiferromagnetic material. This is only one of many possible antiferromagnetic arrangements of magnetic moments. 15

1.5 Orientation of uniaxial anisotropy axis, magnetization unit vector, **m**, and external field, **h** 17

1.6 Longitudinal hysteresis loop for various angles ϕ (0°, 30°, 60° and 90°) [10] 19

1.7 The ideal switching astroid curve [10] 20

1.8 Schematic Diagram showing the magnetic moments of two ferromagnetic layers separated by a non-magnetic layer without magnetic domains. 22

1.9 Schematic Diagram showing the magnetic moments for parallel and anti-parallel interface coupling in an exchange bias sample. 23

2.1 The Princeton Measurements Corp. Model 3900 MicroMag^{TM} Vibrating Sample Magnetometer (VSM) 26

2.2 Orientation of Magnets, Coils and Sample 27

2.3 Electronic symbols used for a semiconductor diode in a circuit diagram for specific types of diodes. 29
2.4 Theoretical IV curve for a tunnel diode illustrating the negative differential region 32
2.5 Schematic diagram of the tunnel diode oscillator used in our experiments 35
2.6 A typical data sweep via the Labview program illustrating susceptibility signal given by a FeCoB SAF sample 38
2.7 The schematic diagram of a a single Helmholtz coil 39
2.8 Magnetic field lines in a plane bisecting the current loops. The field is approximately uniform in between the coil pair. (In this picture the coils are placed one beside the other; the axis is horizontal.) . . 40
2.9 Schematic of the coordinate system for thin-film samples. 42
2.10 Left: Susceptibility signal χ_{xx} detected along the 0x axis, for increasing (top) and decreasing (bottom) field sweeping for $\theta_H = 25$ and $\theta_K = 90$. Right: Theoretical critical curve (astroid) determined from susceptibility measurements for a uniaxial anisotropy system [18] 43
3.1 Schematic representation of the SAF showing the two ferromagnetic layers antiferromagnetically coupled through an interlayer of nonmagnetic material. 45
3.2 Variation of the indirect exchange coupling constant, j , of a free electron gas in the neighborhood of a point magnetic moment at the origin r = 0 [47] 46
3.3 SAF samples structure (not to scale) 47

3.4 MHL of all SAF samples in the series. The applied field is along the easy axis in all MHLs. J is observed to move from positive to negative and back towards positive again as Ru thickness increases [48]. 49
3.5 MHL for SAF, with Ru thickness 14 Å, displaying easy axis and hard axis. 50
3.6 MHL for SAF, with Ru thickness 16 Å, displaying easy axis and hard axis. 51
3.7 Sample placed inside the measuring coil L with the ac and dc fields in plane. The green arrow and the red arrow are perpendicular to each other. The setup shows only one pair of the Helmholtz coils, the pair coils producing the dc magnetic field is laced in and out of the plane of the paper. 52
3.8 Magnetic susceptibility for R16 sample at 0° orientation. The two minimum are the susceptibility values used to create the critical curve. 53
3.9 Experimental static critical curve for sample with Ru thickness 16 Å determined from TDO susceptibility's curves. 54
3.10 The graph obtained from the first derivative of the susceptibility measurements. 55
3.11 Critical curved obtained through two different data acquisition methods overlapped over each other. It shows the error in this step is minimum. 56
3.12 Experimental static critical curve with Ru thickness 14 Å determined from TDO susceptibility's curves. 57

4.1 Easy-axis magnetization curves of a) a soft ferromagnetic film; b) an antiferromagnetic film and c) an exchange-biased bilayer consisting of a ferromagnet and an antiferromagnet. The susceptibility (slope) of the antiferromagnetic's magnetization curve is exaggerated for clarity. 59
4.2 Exchange bias samples structure (not to scale) 61
4.3 MHL for FeMn thickness 3 nm at four different angle orientation that determines the easy axis and hard axis. 62
4.4 MHL for FeMn thickness 6 nm at four different angle orientation that determines the easy axis and hard axis. 63
4.5 MHL for FeMn thickness 9 nm at four different angle orientation that determines the easy axis and hard axis. 63
4.6 MHL for FeMn thickness 12 nm at four different angle orientation that determines the easy axis and hard axis. 64
4.7 MHL for FeMn thickness 15 nm at four different angle orientation that determines the easy axis and hard axis. 64

Abstract

Static techniques to measure different magnetic properties of coupled magnetic nanostructured systems is researched and documented with an extensive analysis of the tunnel diode oscillator (TDO). The VSM was used to obtain the major hysteresis loop for the samples and the TDO was used to measure the magnetic susceptibility. The magnetic susceptibility was employed to conceive the static critical curve.

The thesis describes both equipments, VSM and TDO, that were used to obtain data for our experiments. Albeit a more comprehensive outlook on the TDO is provided. The theoretical functionality of TDO, previous successful applications for experiments, and the physical setup in the laboratory is explored. The novel addition of the double Helmholtz coil in this setup is described. The viability of replacement of the big electromagnet and the advantages of the Helmholtz coil are discussed.

Magnetization dynamics in a series of FeCoB/Ru/FeCoB synthetic antiferromagnetic samples were investigated via reversible susceptibility measurements acquired through the TDO. The major hysteresis loop generated by the VSM were used to calculate the coercivity and magnetic saturation of the sample.

The VSM and TDO were subsequently used to explore the magnetization switching in a different coupled magnetic system, the exchange bias samples. A range of NiFe/FeMn samples were studied with varying thickness of the antiferromagnetic layer.

Keywords: static techniques, coupled magnetic nanostructured systems, tunnel diode oscillator, magnetic susceptibility, critical curve, synthetic antiferromagnets, exchange bias.

Introduction

The dynamic world of technological advancement is always moving forward, always growing. Computers play a vital role in every aspect of our life. From colossal space stations to the slim mobile-phone we can fit in our pockets, all the computer technology originates from scientific research in material science and electromagnetism. Scientists and developers are always in search for a better (smaller and faster) devices that can keep up with the pace of the current societal needs and demands. This research deals with the study of magnetization switching in coupled magnetic nanostructures that can provide a better insight into materials viable for superior electronics.

All magnetic structures with at least one of three dimensions in nanometers range are characterized as magnetic nanostructures. These can be thin films, wires, dots, or a prudent combination of those[1]. Theoretical calculations in mid 20^{th} century depicted that the interface between two (or more) magnetic layers of reduced dimensions would (in principle) induce a change in the typical magnetic properties of such magnetic materials. The change in properties like magnetic anisotropy, domain structure, and hysteresis was speculated to be useful for various applications.

This thesis will not delve in the world of theoretical physics to derive and illustrate the calculations that described the change in magnetic structures due their size and addition of interface. The PhD theses of my predecessors who also worked under the tutelage of Dr. L. Spinu explored the theoretical aspects of research[1, 2, 3]. The experimental verification of the predictions was made possible recently with the advent of high vacuum deposition systems, technological advancements in magnetometers and other equipments.

Magnetization dynamics is one of the central issues in the physics of mesoscopic magnetic systems [4, 5] and its understanding is important not only for its evident

fundamental interest, but also due to the big impact on magnetic information storage technologies. Mesoscopic physics is the area of condensed matter physics that covers the transition between the regime of macroscopic objects and the microscopic, atomic world.

Reasonable resonant magnetization is essential to provide suitable signal data from a magnetic recording media. Coercivity needs to optimized for most practical data storage purposes. It should be high enough to store information but small enough to avoid unnecessary power consumption. We can observe the coercivity via a major hysteresis loop obtained using a vibrating sample magnetometer.

The critical curve was initially considered by J. C. Slonczewski [6] and then developed further by André Thiaville [7]. However, the term, critical curve is derived from the Stoner-Wohfarth model, which was developed by Edmund Clifton Stoner and Erich Peter Wohlfarth and published in 1948 [8], to describe the simplest case of the uniaxial, single domain particles. The remarkable properties of the critical curve can be used to conceive the hysteresis and the corresponding transverse susceptibility curves, providing a lot of useful information about magnetic materials. This illustrates the fact that the critical curve plays a crucial role in the understanding of the static behavior of magnetic materials.

This work is based on L. Spinu's "Vectorial mapping of exchange anisotropy in IrMn/FeCo multilayers using the reversible susceptibility tensor" [9]. Using a tunnel diode oscillator we obtain data for magnetic susceptibility, which is then used to construct the critical curve. This work will deal primarily with static critical curve which can be used as supplement for extensive probing of magnetic structures; dynamic and theoretical. [10, 11, 12]

The distinction between static and dynamic magnetization experiments depends upon the frequency of the external excitation magnetic field. Experiments like the characterization of major hysteresis loop and susceptibility measurements are classified as static experiments. If experiments require an excitation frequency

comparably lower than the frequency of precession (in the range of Gigahertz), they are categorized as static techniques. Conversely, dynamic experiments require a higher frequency excitation fields.

A more specific overview of the thesis describing each chapter is summarized below:

Chapter 1, *Basic Theories and Principles of Magnetism*, provides a succinct description of various theories of magnetism that are later going to be significant in the later chapters. The chapter describes basic ideas needed to understand the thesis but does not delve into an extensive description of all the necessary theories. The chapter briefly goes over the different types of magnetic materials and magnetic properties that are studied in this research.

Chapter 2, *Equipment for Static Magnetic Switching Measurement*, describes all the different equipment that were used to gather data for the research. The vibrating sample magnetometer used to obtain the hysteresis loops of the samples is described, with its function and model. The chapter attempts to thoroughly elucidate the concept of the tunnel diode oscillator. Provided with a brief historical application in research, the chapter clarifies the functionality of the equipment. The chapter details all the equipment that were part of the setup with a concentration on the double Helmholtz coil.

Chapter 3, *Static Critical Curves of Synthetic Antiferromagnets*, describes the physical structure of one of the coupled magnetic structures we are magnetically probing for this research. The chapter describes basic theory involved in the synthetic antiferromagnets and the thin film structure that makes the sample viable. The origin and synthesis of the synthetic antiferromagnet samples used for the study are provided. The chapter then provides the major hysteresis loops for the sample and the susceptibility measurements obtained through the tunnel diode oscillator. The critical curve is derived from the susceptibility data and analyzed.

Chapter 4, *Static Critical Curves of Exchange Bias Samples*, is relatively similar to chapter 3. The chapter describes the coupled magnetic structure denominated exchange bias. A brief overview of the theoretical aspect giving rise to this phenomenon is provided. The origin and the synthesis of the exchange bias samples are detailed. The chapter then provides the static properties of the exchange bias; the major hysteresis loop and the magnetic susceptibility. The critical curve is obtained through the data which can later be integrated with the dynamic measurements of the sample.

The last chapter, *Conclusion*, presents the reader with a summary of the entire study. The possible consequences of the research are discussed. The chapter also talks about future endeavors that can be undertaken to further this study. The results from the exchange bias sample can be used to publish another paper.

The *Appendix* has some supplements that can be used to acquire a better understanding of the subject matter. The sections in the Appendix are not vital for the comprehension of the study but can provide a more appreciative outlook on the subject matter.

1 Basic Theories and Principles of Magnetism

Magnetism is an enigmatic world full of wonders and applications that has left physicists in awe for over the past two millennia. Magnetism is a class of physical phenomena that are mediated by magnetic fields. Electric currents and the magnetic moments of elementary particles give rise to a magnetic field, which acts on other currents and magnetic moments. All materials experience magnetism, some more strongly than others.

Historically (or rather anecdotally), magnetism is said to be discovered by a shepherd. The said shepherd, sometimes described as Magnes the shepherd boy, is attributed for the discovery of magnetism when the nails of his shoes and the ferrule of his staff attracted naturally magnetized pieces of the mineral magnetite, called lodestones, as he was pasturing his herds. In ancient Greece, Aristotle ascribed the first of what could be called a scientific discussion of magnetism to the philosopher Thales of Miletus, who lived from about 625 BC to about 545 BC. Around the same time, in ancient India, the Indian surgeon Sushruta was the first to make use of the magnet for surgical purposes.

Figure 1.1: An illustration of Magnes the shepherd, the (probably mythical) discoverer of natural magnetism.[1]

[1]Ross Murray's 1882 *Warne's Model Housekeeper*, at page 107

Since then magnetism has been studied consistently and fastidiously as a topic of academic interest, and also to investigate its possible real world applications. The world of magnetism was linked to electricity with the publication of James Clerk Maxwell's 1873 *A Treatise on Electricity and Magnetism* in which the interactions of positive and negative charges were shown to be mediated by one force. This revolutionized how we observed magnetism. Later with advent of quantum mechanics physicists were able to interpret phenomena that were always an enigma. Quantum mechanics explained how the individual particles and their characteristics affected and culminated the magnetic properties of the structure as a whole.

The world of magnetism is vast and intriguing. Theoretical and experimental physicists across the world are working on different considerably varied research topics related to the field of magnetism. This chapter will describe few of the theories and physical principles that were used in the description of the coupled magnetic nanostructures.

1.1 Magnetic Moment

The magnetic moment (μ) is a vector quantity used to measure the tendency of an object to interact with an external magnetic field. The term magnetic moment normally refers to a system's magnetic dipole moment. The magnetic moment of a magnet is a quantity that determines the torque it will experience in an external magnetic field. Mathematically,

$$\boldsymbol{\tau} = \boldsymbol{\mu} \times \boldsymbol{B} \tag{1.1}$$

where $\boldsymbol{\tau}$ is the torque acting on the dipole and $\mathbf{B}$ is the external magnetic field.

In magnetic materials, the cause of the magnetic moment are the spin and orbital angular momentum states of the electrons, and varies depending on whether

atoms in one region are aligned with atoms in another.

The vector field that expresses the density of magnetic dipole moments in a magnetic material is called magnetization vector or magnetic polarization. The magnetization vector, denoted as **M** can be characterized as:

$$\boldsymbol{M} = \frac{d\boldsymbol{m}}{dV} \tag{1.2}$$

where d**m** is the elementary magnetic moment and dV is the volume element. Magnetization is the quantity of magnetic moment per unit volume. Net magnetization results from the response of a material to an external magnetic field, together with any unbalanced magnetic dipole moments that may be inherent in the material itself.

1.2 Magnetic Domain

A magnetic domain is a region within a magnetic material in which the magnetization is in a uniform direction. This means that the individual magnetic moments of the atoms are aligned with one another and they point in the same direction. The magnetization within each domain points in a uniform direction, but the magnetization of different domains may point in different directions. The regions separating magnetic domains are called domain walls. The study of magnetic domains is called micromagnetics.

In 1906 French physicist Pierre-Ernest Weiss [56] postulated the existence of small regions called domains, each spontaneously magnetized. As explained above, a domain which is too big is unstable, and will divide into smaller domains. But a small enough domain will be stable and will not split, and this determines the size of the domains created in a material. This size depends on the balance of several energies within the material. Magnetic materials divide into domains to minimize their internal energy.

1.3 Magnetic Anisotropy

Magnetic anisotropy refers to the directional dependence of a material's magnetic properties. The magnetic moment of magnetically anisotropic materials will tend to align with an easy axis, which is an energetically favorable direction of spontaneous magnetization. The two opposite directions along an easy axis are usually equivalent, and the actual direction of magnetization can be along either of them.

Magnetic anisotropy can be caused by various reasons. Magnetocrystalline anisotropy ensues when the atomic structure of a crystal introduces preferential directions for the magnetization. Shape anisotropy transpires when a particle is not perfectly spherical, the demagnetizing field will not be equal for all directions, creating one or more easy axes. Magnetoelastic anisotropy arises when tension may alter magnetic behaviour, leading to magnetic anisotropy. Exchange anisotropy occurs when antiferromagnetic and ferromagnetic materials interact.

1.4 Magnetic Susceptibility

Magnetic susceptibility is a measure of the magnetic properties of a material that describes the extent to which a substance becomes magnetized when it is placed in an external magnetic field. The susceptibility indicates whether a material is attracted or repelled by an external applied magnetic field, which in turn has implications for practical applications. This response is dependent upon the state of sample and may occur in directions other than that of the applied field. A synonym for susceptibility is magnetizability.

The magnetic susceptibility χ is defined by the ratio between the induced magnetization of a magnetic sample and the inducing magnetic field. Magnetic susceptibility is a dimensionless proportionality constant. The fact that the magnetic field $\mathbf{H}$ and the magnetization $\mathbf{M}$ are both vectors indicates magnetic susceptibility

χ is also a vector.

$$\boldsymbol{M} = \boldsymbol{\chi H} \tag{1.3}$$

M is dependent upon the orientation of the sample and can occur in directions other than that of the applied field **H**. In these cases, volume susceptibility is defined as a second order tensor with dimension (3,3) that depicts the component of magnetization in the i-th direction from the external field applied in the j-th direction. The subscripts i and j refer to the directions (e.g., x and y in Cartesian coordinates) of the applied field and magnetization, respectively.

$$\boldsymbol{M_i} = \boldsymbol{H_j \chi_{ij}} \tag{1.4}$$

The tensor is modified to accommodate the non-linear relationship between **M** and **H** evident in ferromagnetic materials. A more general definition of differential susceptibility[2] is used instead. When the coercivity of the material parallel to an applied field is the smaller of the two, the differential susceptibility is a function of the applied field and self interactions, such as the magnetic anisotropy. When the material is not saturated, the effect will be nonlinear and dependent upon the domain wall configuration of the material. $\boldsymbol{\chi^d_{ij}}$ is a tensor derived from partial derivatives of components of **M** with respect to components of **H**.

$$\boldsymbol{\chi^d_{ij}} = \frac{\boldsymbol{\partial M_i}}{\boldsymbol{\partial H_j}} \tag{1.5}$$

The susceptibility tensor calculates the response of the magnetization in the i-th direction originating from an incremental change in the external applied field in the j-th direction. The susceptibility tensor has nine components, three of which can independent. It can be done by determining appropriate orientation of the body-fixed coordinate system and hence reducing the susceptibility tensor to its

[2]Not to be confused with differential susceptibility hypothesis proposed by Jay Belsky for interpretation of psychological findings.

diagonal form. The diagonalization of the susceptibility tensor is done by aligning the easy axis of the sample parallel with coordinate system's axis.

If the change in the applied field provides only reversible change in magnetization we refer to the process as reversible susceptibility. This indicates there is no hysteresis and hence no energy loss.

1.5 Ferromagnetism

A ferromagnetic material is a magnetic material which possesses a high susceptibility to magnetization, the strength of which depends on that of the applied magnetizing field. Materials classified as such have strongly coupled atomic dipole moments which tend to align to the applied field. Ferromagnetic materials such as iron, contain unpaired electrons, each with a small magnetic field of their own, that readily align with each other in response to an external magnetic field. This alignment tends to persists even after the magnetic field is removed, a phenomenon called hysteresis.

The ferromagnetic Curie[3] temperature, T_f, is a critical temperature above which the spontaneous magnetization of property of the material vanishes. The materials properties at or above Curie temperature are similar to those of paramagnetic materials. Magnetic susceptibility above the Curie temperature can be calculated from the Curie–Weiss law,

$$\chi = \frac{C}{T - T_f} \tag{1.6}$$

where C is a material-specific Curie constant and T is absolute temperature measured in kelvins.

The application of a comparatively small magnetic field produces a magnetic moment which is in many orders of magnitude larger than that produced in para-

[3]named after Pierre Curie

magnetic substances. As mentioned above, a magnetic domain is a region within a magnetic material in which the magnetization is in a uniform direction. This means that the individual magnetic moments of the atoms are aligned with one another and they point in the same direction. The direction of alignment varies from domain to domain in a more or less random manner, although certain crystallographic axis may be preferred by the magnetic moments, called easy axes.

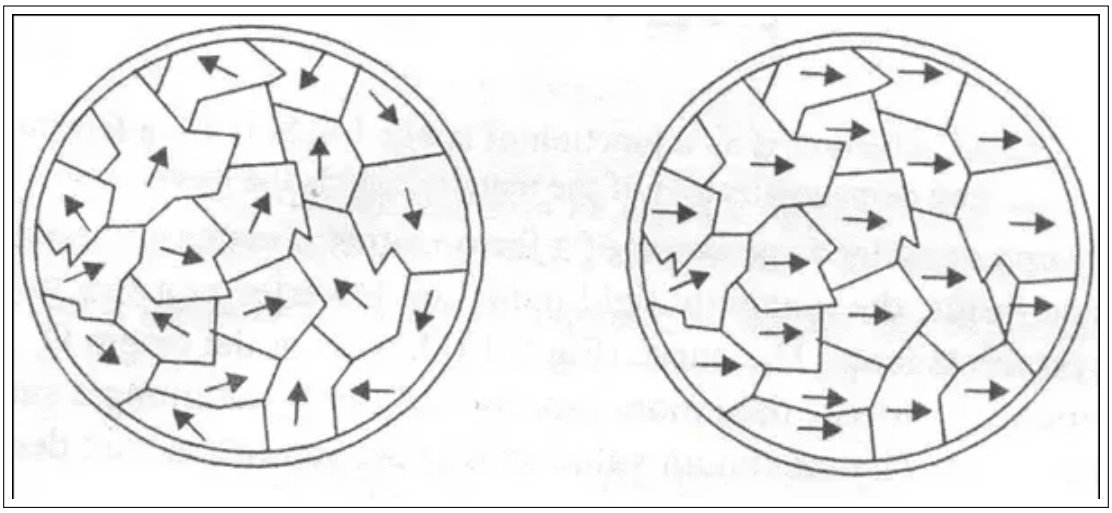

Figure 1.2: Magnetic moments of domains before (left) and the aligned magnetic domain after (right) the application of an external magnetic field

The magnetic moment of a an entire specimen is the vector sum of the magnetic moment of each domain. The direction of magnetization of each domain does not need to be parallel, thus certain domain configuration leads to zero net moment. The application of a relatively small magnetic field changes the domain arrangement, and hence leads to an appreciable net magnetization.

Magnetic domains form in materials which have magnetic ordering; that is, their dipoles spontaneously align due to the exchange interaction. These are the ferromagnetic, ferrimagnetic and antiferromagnetic materials. Paramagnetic and diamagnetic materials, in which the dipoles align in response to an external field but do not spontaneously align, do not have magnetic domains.

Permanent magnets are either ferromagnets or ferrimagnets. Permanent mag-

nets are not abundant in nature, this makes the property of spontaneous magnetization of ferromagnets very useful. Ferromagnetism is crucial in industry, modern technology, and nanoparticle research. Such materials are the basis for many electrical and electromechanical devices including but not limited to electromagnets, electric motors, generators, transformers, and magnetic storage such as tape recorders and hard disks.

1.5.1 Magnetic Hysteresis

Hysteresis is the dependence of the state of a system on its history. A magnetic material like a ferromagnet can have more than one possible magnetic moment in a given magnetic field, depending on how the field changed in the past. Magnetic hysteresis occurs when the atomic dipoles of a ferromagnet align themselves with an applied magnetic field. The alignment of the domains is retained even after the magnetic field is removed. In order to demagnetize the sample requires magnetic field in the opposite direction.

The relationship between field strength H and magnetization M or (induced magnetic flux density B) is not always linear. For a ferromagnetic material that has never been previously magnetized or has been thoroughly demagnetized (H=M=0), M follows the initial magnetization curve. This curve increases rapidly at first and then approaches an asymptote called magnetic saturation. If the magnetic field is now reduced monotonically, M follows a different curve. At zero field strength, the magnetization is offset from the origin by an amount called the remanence or retentivity. If the H-M relationship is plotted over a cycle for all strengths of applied magnetic field the result is a hysteresis loop.

The phenomenon of hysteresis in ferromagnetic materials is the result of rotation of magnetization and changes in size or number of magnetic domains. Once the magnetic domains are reoriented, it takes some energy to turn them back again. This property of ferrromagnetic materials is useful as a magnetic memory,

for example magnetic tape, hard disks, and credit cards.

The simple magnetization hysteresis loops for which the starting and ending fields exceed the saturation field, where the property of hysteresis vanishes are referred to as major hysteresis loops. We only investigate major hysteresis loops (MHL) in our experiments.

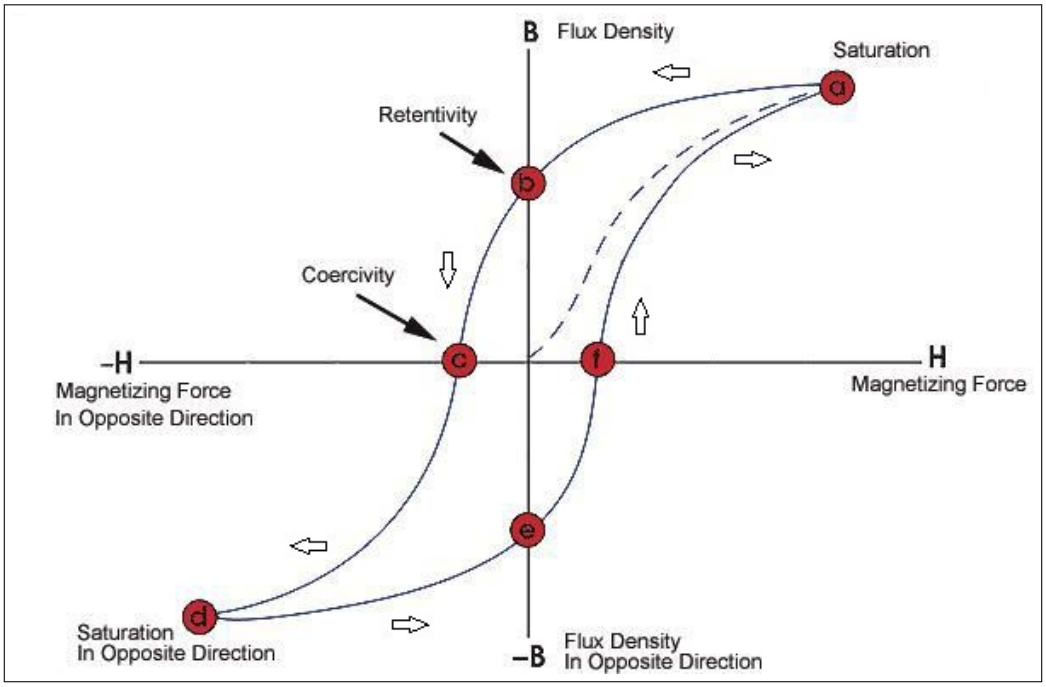

Figure 1.3: A typical hysteresis loop. The broken line is the initial magnetization curve. The downward curve after saturation, along with the lower return curve, form the main loop.

1.5.2 Coercivity

The coercivity, also referred to as magnetic coercivity, coercive field or coercive force, is the resistance of a magnetic material to changes in magnetization, equivalent to the field intensity necessary to demagnetize the fully magnetized material. Coercivity is usually measured in oersted (Oe) or ampere/meter (A/m) units and is denoted H_C. It can be measured using a B-H analyzer or a magnetometer.

The amount of reverse magnetic field which must be applied to a magnetic

material to make the magnetic flux return to zero. This is marked on the hysteresis loop where the magnetization is zero but the magnetic field is nonzero (points c and f).

1.6 Antiferromagnetism

Antiferromagnetism, like ferromagnetism, is phenomena caused by alignment of magnetic moment of individual domain. The atomic dipole spontaneously align themselves into opposite, or antiparallel arrangements across the material such that the vector sum of the magnetic moment of each domain results in a zero magnitude. Antiferromagnets are considerably less abundant in comparison to the other types of magnetic materials, and are ordinarily observed at typical low temperatures.

Antiferromagnetism has an analogue for ferromagnetism's Curie temperature, T_f, called Néel temperature [54], T_N. The ordering of the domains required to exhibit antiferromagnetic properties are only discernible at adequately low temperatures. The susceptibility for antiferromagnetic materials above T_N, obeys the Curie-Weiss law characterizing paramagnets but produces a negative intercept providing evidence for negative exchange interactions.

In 1936, Louis Eugène Félix Néel, a French physicist was the first person to theorize the existence of a novel magnetic material existing at certain temperatures. Louis Néel initially proposed the existence of a magnetic material with two sublatices with antiparallel moment alignment resulting in a net zero moment [55]. Since Néel's original hypothesis, the term antiferromagnetism has been extended to include materials with more than two sublattices and those with triangular, spiral, or canted spin arrangements. The latter arrangements may have a negligible nonzero magnetic moment.

Antiferromagnets exhibit quite distinctive behavior in nature but do not pos-

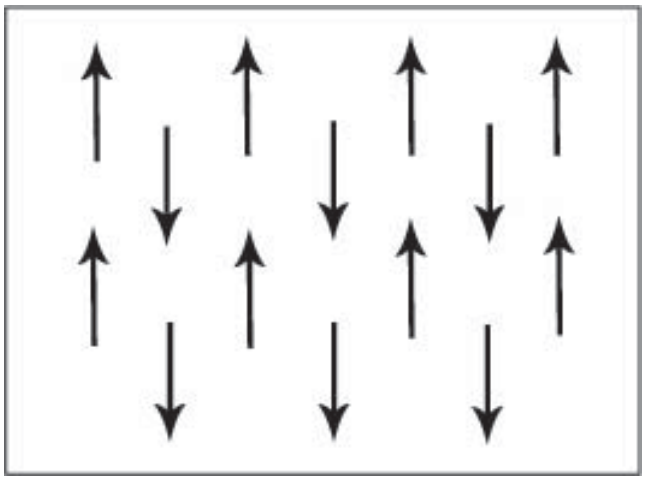

Figure 1.4: Schematic showing adjacent magnetic dipole moments with equal magnitude aligned anti-parallel in an antiferromagnetic material. This is only one of many possible antiferromagnetic arrangements of magnetic moments.

sess a plethora of applications like other magnetic materials. Antiferromagnets are weakly magnetized in the presence (or absence) of an applied magnetic field and the characteristics particular to antiferromagnetic materials are predominantly apparent at substantially low temperatures. This makes the practical application of antiferromagnetic materials difficult. However, the lack an of overall magnetic moment makes them uniquely advantageous for establishing magnetic reference points in magnetic sensors since the structure of antiferromagnets is not sensitive to external fields.

Antiferromagnets may not comprise of an abundance of uses by themselves, but coupled with ferromagnet gives arise to a phenomena called exchange bias. This is particularly useful to pin the harder reference layer in spin valve readback heads and MRAM memory circuits that utilize the giant magnetoresistance or magnetic tunneling effect.

1.7 Stoner–Wohlfarth Model

The Stoner–Wohlfarth (SW) model is one of the simplest models that adequately characterizes the physics of single domain ferromagnetic particle or nanostructure. It is a simple example of magnetic hysteresis and is useful for modeling small magnetic particles in magnetic storage. The Stoner–Wohlfarth model was developed by Edmund Clifton Stoner and Erich Peter Wohlfarth and published in 1948 [8]. It included a numerical calculation of the integrated response of randomly oriented magnets.

The Stoner–Wohlfarth model is based on the simple idea that a ferromagnet can be represented by a single magnetic moment, which represents the state of the all the *actual* magnetic moments. Thus, all multi-domain related effects like non-uniformities or inhomogeneities can be neglected. A single domain occurs when the size of the grain is smaller than some critical length. The model takes the absolute temperature, T = 0 K where a grain carrying a single moment $\mathbf{M}$, is an ellipsoid-shaped object.

The magnetic structure possesses a uniaxial anisotropy in SW model. Upon application of an externally applied static magnetic field $\mathbf{H}$, $\mathbf{M}$ can evolve precisely in a two-dimensional space. Therefore it can be characterized by a single angle Θ, the angle between magnetization vector and the anisotropy axis. Φ is the angle the external applied magnetic field makes with the easy axis.

The free energy of the uniaxial particle per unit volume is comprised of the magnetocrystalline anisotropy energy and the energy of interaction with the external field. The interaction between the magnetization and the external applied field is called the Zeeman energy. The energy density in this case is given by $E_Z = -\mathbf{M} \cdot \mathbf{H}$. The total energy is given by the equation [10]:

$$E_{SW}(\theta, \mathbf{H}) = K_1 \sin^2 \theta - M_S \boldsymbol{H} \cos(\theta - \phi) \tag{1.7}$$

where K_1 is the first-order first anisotropy constant, θ and ϕ the angles made by normalized vectors $\boldsymbol{m} = \dfrac{\mathbf{M}}{M_s}$ and $\boldsymbol{h} = \dfrac{\mathbf{H}}{H_K}$ (where H_k is the anisotropy field),with the easy direction. This is clearly illustrated in the figure below.

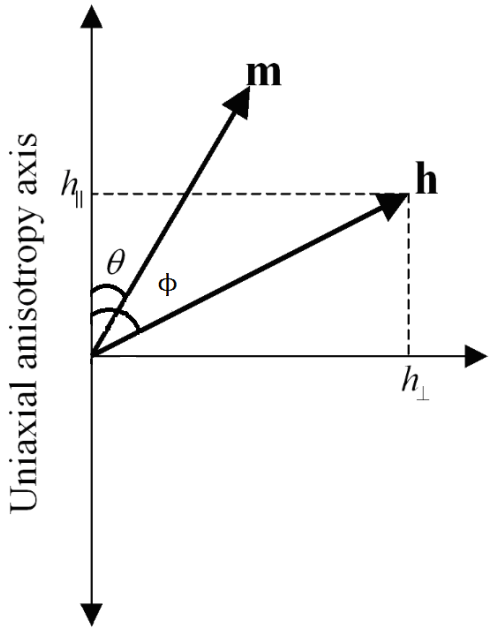

Figure 1.5: Orientation of uniaxial anisotropy axis, magnetization unit vector, **m**, and external field, **h** .

The magnetic moment will orient itself in order to minimize the energy. As in magnetization switching, this process may occur smoothly or abruptly. This indicates that there is a value for **H** where **M** is discontinuous and results in magnetization switching. At equilibrium where the energy is minimum, the vector **M** will be defined by an angle θ^*. First and second order differential equations of the total energy with respect to θ can be used to derive the equations required for the critical switching fields. The conditions of minimum energy at θ^* are

$$\left(\frac{\partial E_{SW}}{\partial \theta}\right)_{\theta=\theta^*} = 0 \qquad \text{and} \qquad \left(\frac{\partial^2 E_{SW}}{\partial \theta^2}\right)_{\theta=\theta^*} > 0 \tag{1.8}$$

This conditions yield the following two equations respectively,

$$[2K_1 \sin\theta\cos\theta - M_S \boldsymbol{H} \sin(\theta - \phi)]_{\theta=\theta^*} = 0 \tag{1.9}$$

$$[2K_1(\sin^2\theta - \cos^2\theta) + M_S \boldsymbol{H} \cos(\theta - \phi)]_{\theta=\theta^*} = 0 \tag{1.10}$$

Equation 1.5 can be reduced to:

$$[2K_1 \cos 2\theta + M_S \boldsymbol{H} \cos(\theta - \phi)]_{\theta=\theta^*} = 0 \tag{1.11}$$

These equations can be normalized by the saturation magnetization and anisotropy field to get:

$$[\sin\theta\cos\theta - \mathbf{h}\cos(\theta - \phi)]_{\theta=\theta^*} = 0 \tag{1.12}$$

$$[\cos 2\theta + \mathbf{h}\cos(\theta - \phi)]_{\theta=\theta^*} = 0 \tag{1.13}$$

Simultaneous solutions of these equations [13] give us the critical field and critical angle at which the magnetization vector will switch.

$$h_c^2 = 1 - \frac{3}{4}\sin^2\theta_c \tag{1.14}$$

$$\tan^3\theta_c = -\tan\theta_k \tag{1.15}$$

The component of M, along H and perpendicular to H is respectively:[4]

$$m_{\parallel} = \cos(\theta - \phi) \tag{1.16}$$

$$m_{\perp} = \sin(\theta - \phi) \tag{1.17}$$

The hysteresis loop for $\phi = 0$, $\theta = 0$ and $\frac{\pi}{2}$, and $m_{\perp} = 0$ results in a square

[4]The indices $\parallel$ and $\perp$ of the demagnetization coefficients denote respectively that they are parallel or perpendicular to the z-axis.

hysteresis loop. On the other hand at $\phi = \frac{\pi}{2}$, $\theta = \frac{\pi}{2}$, and $m_{\parallel} = h$, there is no apparent hysteresis. The figure below shows the theoretical hysteresis loops for different values of ϕ.

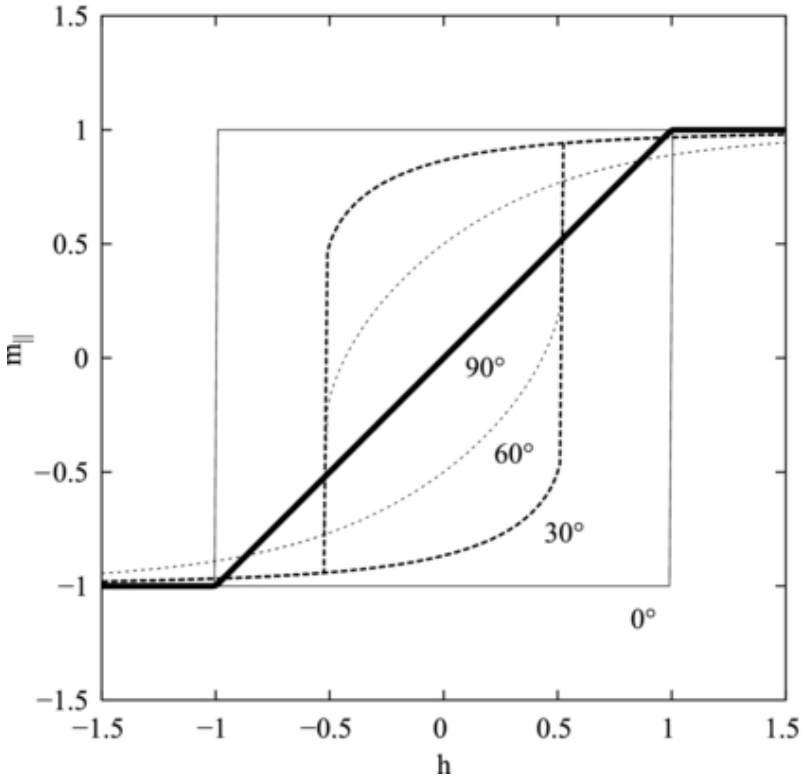

Figure 1.6: Longitudinal hysteresis loop for various angles ϕ (0°, 30°, 60° and 90°) [10]

The Stoner-Wohlfarth astroid, the critical curve for magnetization switching is found as follows [14]. Starting with the anisotropy field,

$$H_K = \frac{2K_1}{M_S}$$

We define this equation in terms of its reduced components parallel ($h_{\parallel}$) and perpendicular ($h_{\perp}$) to the easy axis.

$$h_{\parallel} = \frac{H_{\parallel} M_S}{2K_1} \qquad \text{and} \qquad h_{\perp} = \frac{H_{\perp} M_S}{2K_1} \tag{1.18}$$

The total energy is now written taking both of these fields into account.

$$E_{SW}(\theta, \mathbf{H}) = K_1 \sin^2\theta - H_{\parallel} M_S \cos\theta - H_{\perp} M_S \sin\theta \tag{1.19}$$

Again, taking the first and second derivative of the total energy and equation to zero, we get:

$$\frac{\partial E_{SW}}{\partial \theta} = \sin\theta\cos\theta + h_{\parallel} M_S \sin\theta - h_{\perp} M_S \cos\theta = 0 \tag{1.20}$$

$$\frac{\partial^2 E_{SW}}{\partial \theta^2} = (\sin^2\theta - \cos^2\theta) + h_{\parallel} M_S \cos\theta + h_{\perp} M_S \sin\theta = 0 \tag{1.21}$$

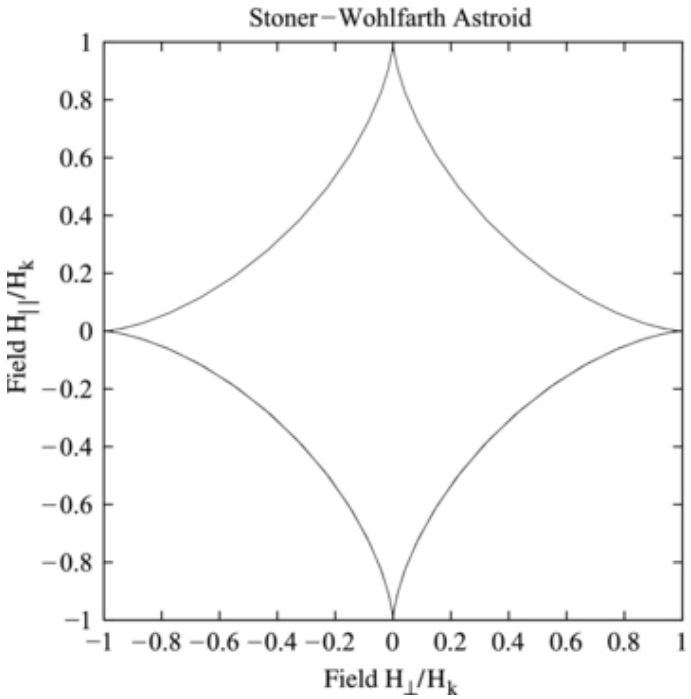

Figure 1.7: The ideal switching astroid curve [10]

Solving the above equations gives the value for the reduced components ($h_{\parallel}$) and ($h_{\perp}$).

$$h_{\parallel} = -\cos^3\theta h_{\perp} = \sin^3\theta \tag{1.22}$$

These equations generate a curve when θ is varied from 0 to 2π. It yields an astroid curve illustrated in the figure 1.7.

This critical curve was developed to realize the points of stability in the magnetic system. The orientation of m for a given h can be found. When the critical curve is crossed during a field change, switching of m may occur, depending on its starting point.

1.8 Coupled Magnetic Nanostructures

Rapid advancement in science and technology has made magnetic structures more controllable on nanoscale. All magnetic structures with at least one of three dimensions in nanometers range are characterized as magnetic nanostructures. These can be thin films, wires, dots, or a prudent combination of those [1]. Theoretical calculations in mid 20^{th} century depicted that the interface between two (or more) magnetic layers of reduced dimensions would (in principle) induce a change in the typical magnetic properties of such magnetic materials. The change in properties like magnetic anisotropy, domain structure, and hysteresis was speculated to be useful for various applications.

Most of the theoretical and experimental research done previously referred mainly to a single layer, like in the Stoner-Wohlfarth method. With the advent of new fabrication techniques that provided minute control over the thickness of the magnetic layers on nanoscale, we can deposit multiple layers of thin films with different magnetic properties. This is essential for technological applications.

Two films that are superposed in closely spaced parallel space are separated enough to avert atomic interaction but compact enough to warrant magnetostatic interaction. The magnetostatically coupled thin films divulge static (and dynamic) behaviors substantially different from single layered thin films.

C. Radu explores the difference between the magnetic switching properties of

uncoupled and couple magnetic nanostructures in his PhD thesis [2]. The magnetic characteristics exhibited by the coupled nanostructures emerge from the interface coupling.

This research focuses solely on two coupled magnetic nanostructured systems, synthetic antiferromagnetic and exchange bias samples. The coupling in synthetic antiferromagnets result from two ferromagnetic layers separated by a nonmagnetic layer. The magnetic moments in the two layers are in aligned anti-parallel, so depending on the thickness of the nonmagnetic layer the sample exhibits antiferromagnetic coupling.

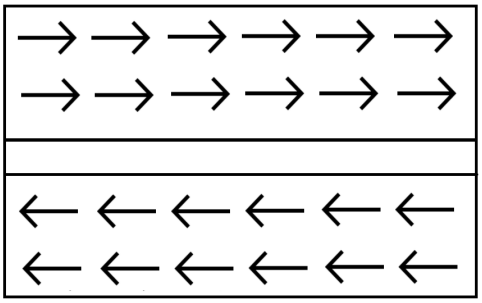

Figure 1.8: Schematic Diagram showing the magnetic moments of two ferromagnetic layers separated by a non-magnetic layer without magnetic domains.

The exchange bias samples on the other hand is formed by coupling a ferromagnetic and an antiferromagnetic layer. Exchange bias samples can be bilayer or multilayer. Depending upon the thickness of each layers, and the property of the individual layers the exchange bias varies [57]. Parallel and anti-parallel interface coupling (as shown in the figure 1.9), result in different exchange bias [58].

The thesis looks into the magnetization switching of these two coupled magnetic nanostructures. The major hysteresis loops of these structures are also explored. The magnetic characteristics exhibited by such samples are clearly different from a single layered or uncoupled sample. The samples and their characteristics are described more thoroughly in Chapter 3 (Static Critical Curves of

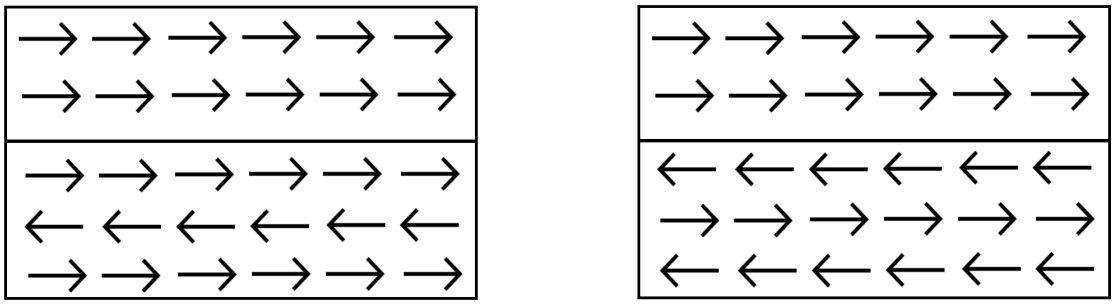

Figure 1.9: Schematic Diagram showing the magnetic moments for parallel and anti-parallel interface coupling in an exchange bias sample.

Synthetic Antiferromagnets) and Chapter 4 (Static Critical Curves of Exchange Bias Samples).

2 Equipment for Static Magnetization Switching Measurement

Proper equipment are undoubtedly one of the most imperative components for experimental physics. There are numerous methods and experimental setups to probe the same characteristic. Each approach comes with its own merits and faults. Physicists have been continually performing experiments with varying equipment to determine the optimum technique to measure certain behaviors. In the study of coupled magnetic multi-layers there are many observable behaviors that can be studied.

This particular study deals with the study of static critical curves by probing the susceptibility for different dc fields applied in the plane of the multi-layered magnetic thin film using a tunnel diode oscillator (TDO) method. The tunnel diode oscillator has been used previously for similar studies, but this particular research uses a double Helmholtz coil as an alternative to the traditional electromagnet. The Helmholtz coil's maximum magnetic field is considerably lower in comparison to the electromagnet but has the advantage of providing a region where the magnetic field is uniform and easily accessible for experiments. This as shown by results provides a much better resolution of the magnetic susceptibility.

The vibrating sample magnetometer (VSM) was utilized prior to measuring susceptibility using the tunneling diode oscillator. The vibrating sample magnetometer was used to measure major hysteresis loops (MHL) for both multi-layered samples. The vibrating sample magnetometer was employed in order to identify an easy axis and the type of coupling present. The hysteresis loop obtained from the vibrating sample magnetometer is also a static curve.

This chapter will go in a little detailed description of the theoretical aspects of the equipment used in this study. The chapter will also describe the setup and procedures that were undertaken to complete this research.

2.1 Vibrating Sample Magnetometer

A magnetometer is an instrument that has the capability to measure the magnetization of a magnetic material like a ferromagnet, or the direction, strength, or relative change of a magnetic field at a particular location. A compass is a simple type of magnetometer, one that measures the direction of an ambient magnetic field. The first magnetometer capable of measuring the absolute magnetic intensity was invented by Carl Friedrich Gauss in 1833. Laboratory magnetometers measure the magnetization, also known as the magnetic moment of a sample material. Such equipment require the sample to be placed inside the magnetometer where factors like temperature, magnetic field, and other parameters of the sample can often be regulated.

The vibrating sample magnetometer (often abbreviated as VSM) is one of the most remarkable implementations of a magnetometer. The VSM is an exceptionally sensitive system for the measurement of magnetic susceptibility. The concept of the design and application of the vibrating sample came from D. O. Smith's [19] vibrating-coil magnetometer. Simon Foner at MIT Lincoln Laboratory invented the novel form of magnetometer coined vibrating sample magnetometer in 1955 and reported it in 1959 [20].

The Princeton Measurements Corp. Model 3900 MicroMag^{TM} Vibrating Sample Magnetometer (VSM) was used to attain the major hysteresis loop (MHL) for this experiment. This particular VSM is highly sensitive and can provide results extending to 0.5 μemu at unit second per point. This compact, computer-controlled susceptibility measurement system is capable of measuring the magnetic properties of a wide range of sample materials. The applied field is continuously monitored via a built-in Hall-effect gaussmeter. A corresponding feedback signal provides precise servoed control in both field sweep or static mode conditions. The mechanical transducer assembly features precision X-Y-Z translation, vibra-

tion isolation, continuous rotation about the Z axis under computer control, and a quick disconnect collet for efficient sample changing.

Figure 2.1: The Princeton Measurements Corp. Model 3900 MicroMag™ Vibrating Sample Magnetometer (VSM)

The MicroMag VSM system includes a PC-compatible computer, Windows operating software, LCD monitor, and color inkjet printer. A comprehensive Windows-based operating software package provides automatic procedures to assist the operator in positioning the sample, demagnetizing and determining various sample parameters, including saturation magnetization, retentivity, switching field distribution, squareness ratio, slope correction, coercivity, coercivity of remanence,

time dependence, etc. from raw data.

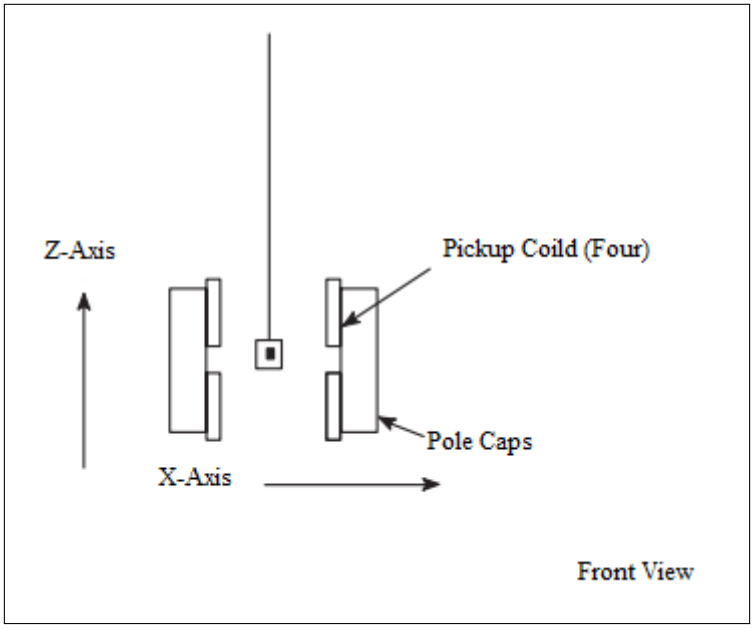

Figure 2.2: Orientation of Magnets, Coils and Sample

A vibrating sample magnetometer, as the name would suggest, by vibrating the magnetic sample. The sample is introduced in a constant uniform external magnetic field generated by electromagnets which induces a magnetization in the sample. The sample is suspended from a non-magnetic rod using vacuum grease. The sample is vibrated vertically at the midpoint of the magnetic field, centered in the small space between the signal pickup coils mounted on the poles of the magnet. As the magnetized sample goes through a controlled vibration, it introduces perturbations in the external magnetic field. The VSM relies on signal processing to ensure that the output perturbation signal is exclusively derived from the magnetization of the material.

An alternating gradient magnetometer (AGM) can also be used to obtain the major hysteresis loop (MHL). As with the VSM, a dc field is produced by a set of coils that magnetized the sample. This is constantly monitored by a gaussmeter. The AGM is more sensitive than the VSM. The AGM is capable of measuring magnetic moments in the range of nano-emu (10^{-9} emu), whereas the VSM is lim-

ited to moments on the order of μemu (10^{-6}emu). In comparison with alternating gradient magnetometer, the VSM is indifferent to mass and size of sample up to a considerable range.[5]

The MHL is an astoundingly convenient characterization technique from which much useful information can be immediately and relatively effortlessly identified through observation . Due to the usefulness and simplicity in obtaining the MHL is often the first method used in magnetic material characterization. In our experiments this convention was observed by obtaining the MHL via the VSM.

2.2 Tunnel Diode Oscillator

2.2.1 Introduction

A diode is one of the elemental components of an electric circuit. A diode is two-terminal electronic component that conducts current primarily in one direction (asymmetric conductance[6]). An ideal diode has zero resistance in one direction and infinite resistance in the other direction. A semiconductor diode is the most common type of diode. It is a crystalline piece of semiconductor material with a p–n junction connected to two electrical terminals. A tunnel diode or Esaki diode is a type of semiconductor that is capable of very fast operation, well into the microwave frequency region, made possible by the use of the quantum mechanical effect called tunneling.

Quantum tunneling[7] is the quantum mechanical phenomenon where a particle tunnels through a barrier that it could not surmount via classical (or Newtonian) mechanics. Fundamental quantum mechanical concepts are central to this phenomenon, which makes quantum tunneling one of the novel implications of

[5]The maximum mass sustained on the MicroMag^{TM} is 10 grams.

[6]Electrical conductance is the ease with which an electric current passes. It is the opposite of resistance

[7]Quantum Theory of Tunneling by Mohsen Razavy is a wonderful book to inquire further into the world of quantum mechanics and specifically quantum tunneling.

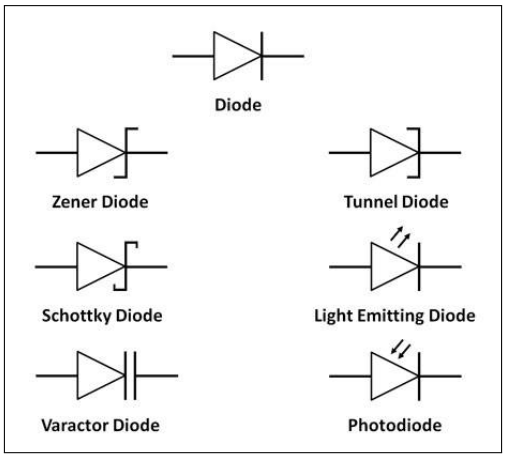

Figure 2.3: Electronic symbols used for a semiconductor diode in a circuit diagram for specific types of diodes.

quantum mechanics. Quantum tunneling is projected to create physical limits to how small transistors can get, due to electrons being able to tunnel past them if they are too small. It has important applications to modern devices such as the tunnel diode, quantum computing, and the scanning tunneling microscope. (Quantum tunneling is not limited to electronics, this phenomena also helps explain cosmological problems about lower temperatures during nuclear fusion that occurs in main sequence stars like the Sun.)

An (electronic) oscillator is an electronic circuit that produces a periodic, oscillating electronic signal[8]. Oscillators convert direct current (DC) from a power supply to an alternating current (AC) signal. An oscillator can be assembled using various electronic components. LC circuit often called tank circuit is one of the primary approaches to an electronic oscillator.

An ideal LC circuit consists of an ideal inductor (zero resistance) of inductance L connected with an ideal capacitor (infinite resistance) of capacitance C. An electrically charged capacitor induces an alternating current in the circuit upon connecting to an inductor. The resonance frequency of the alternating current is dependent of the value of inductance and capacitance of the inductor and the

[8]Often a sinusoidal wave or a square wave.

capacitor respectively, while the amplitude is governed by the total electric charge in the circuit.

The real world is nowhere near ideal. So, the (large, yet) finite resistance of capacitor and (small, yet) finite resistance of the inductor instigate substantial energy loss which dampens the current oscillations exponentially with a time constant dependent on the resistance of the circuit. In order to maintain a steady resonant state in the LC circuit and sustain a constant amplitude of the oscillations, the energy lost during each cycle must be replaced by corresponding amount of energy[9]. This can be done by drawing an essential unit of the output signal, amplifying it and feeding it back to the oscillator. Another way of maintaining steady oscillations in a real circuit is by compensating for the lost energy using a negative resistance of a tunnel diode.

Negative resistance oscillators are used at high frequencies in the microwave range and above, since at these frequencies feedback oscillators perform poorly due to excessive phase shift in the feedback path. Negative resistance oscillators use a resonant circuit like an LC circuit connected across a device with negative differential resistance, such as magnetron tubes, tunnel diodes, IMPATT diodes or Gunn diodes, and a DC bias voltage is applied to supply energy.

2.2.2 The Tunnel Diode

The tunnel diode is the most crucial component of the tunneling diode oscillator. As the name implies, the tunnel diode uses a tunneling effect to provide a negative resistance region in its IV characteristic as the key to its operation. The tunnel diode was invented in August 1957 by Leo Esaki, Yuriko Kurose and Takashi Suzuki when they were working at Tokyo Tsushin Kogyo, now known as Sony [21]. Leo Esaki, also known as Reona Esaki is attributed to the discovery of the phenomenon of electron tunneling, which he later exploited for the invention

[9] A feedback oscillator

of the Esaki diode. Esaki discovered that narrow p-n junctions exhibit a region of negative differential resistance characterized by an increase in voltage as current is decreased [22].

Tunnel diodes were initially manufactured by Sony in 1957. General Electric and other companies followed the trend from about 1960. These diodes are still produced today, but in low volume because other semi-conducting devices with superior qualities have been discovered for most application purposes. Tunnel diodes are usually made from germanium, but can also be made from gallium arsenide and silicon materials. Tunnel diodes have a heavily doped p-n junction that is about 10-15 nm wide. The heavy doping causes a broken band gap, where conduction band electron states on the n-side are more or less aligned with valence band hole states on the p-side.

In a conventional semiconductor diode, conduction takes place while the p-n junction is forward biased and blocks current flow when the junction is reverse biased. This occurs up to a point known as the reverse breakdown voltage at which point conduction begins (often accompanied by destruction of the device). In a tunnel diode, the dopant concentrations in the p and n layers are increased to a level such that the reverse breakdown voltage becomes zero and the diode conducts in the reverse direction. However, during forward-biased, quantum mechanical tunneling gives rise to a region in its voltage-current behavior where an increase in forward voltage is accompanied by a decrease in forward current. This negative resistance region can be exploited in a very fast oscillator, giving rise to the tunneling diode oscillator.

During normal forward bias operation, as voltage is increased, electrons initially tunnel through the very narrow p-n junction barrier. This is possible because filled electron states in the conduction band on the n-side become aligned with empty valence band hole states on the p side of the p-n junction. As the voltage keeps on increasing, these states become more misaligned and the current is re-

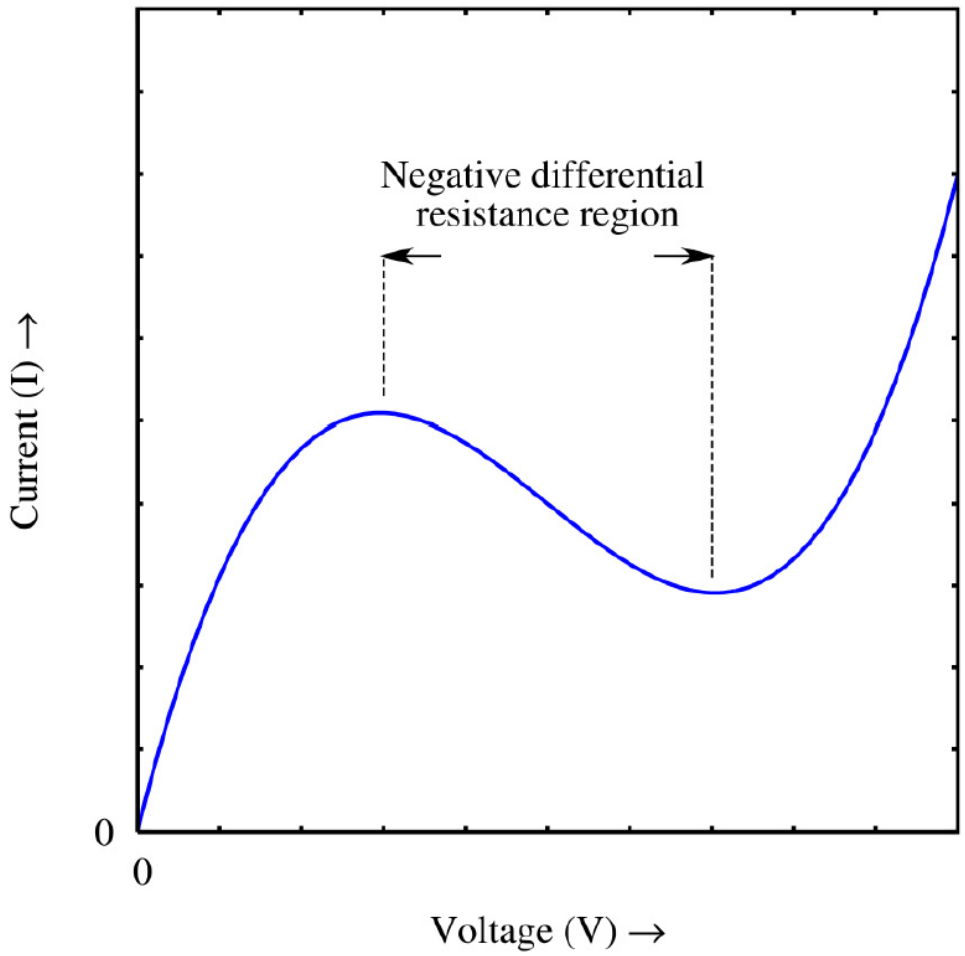

Figure 2.4: Theoretical IV curve for a tunnel diode illustrating the negative differential region

duced. This phenomena is labeled negative resistance because current decreases while the voltage increases. As voltage increases yet further, the diode begins to operate as an ordinary semiconductor diode, where electrons travel by conduction across the p-n junction, and no longer by tunneling through the p-n junction barrier. Therefore, the most important operating region for a tunnel diode is the negative resistance region. This phenomenon of the tunnel diode is illustrated in the following figure. The typical forward bias value necessary to bring the tunnel diode at the middle of the negative resistance region is approximately between 50 and 100 mV. Practical tunnel diodes operate at a few milliamperes and a few

tenths of a volt, making them low-power devices.

Tunnel diodes are notable for their longevity, with devices made in the 1960s still functioning. Writing in Nature, Esaki and coauthors [22] state that semiconductor devices in general are extremely stable, and suggest that their shelf life should be "infinite" if kept at room temperature. They go on to report that a small-scale test of 50-year-old devices revealed a "gratifying confirmation of the diode's longevity." The tunnel diode used for this study (and many experiments before) is a testament to that.

Timeline for different experiments performed using the tunnel diode experiments that provided a better insight in the equipment's application and helped develop maximize its efficiency is provided in the appendix.

Throughout the better half of the last century and this one, the preeminent implementation of TDO related experiments has established as one of the primary techniques in nanostructure studies. These studies vary from London penetration depth[10], for magnetic and meta-magnetic transitions, superconductor's characterization, and the one application applicable for this study: the magnetization switching characterized via susceptibility studies.

2.2.3 Tunneling Diode Oscillator Setup in the Laboratory

The resonant frequency (f_0) of oscillation for a tank circuit with inductance L and capacitance C is characterized by the following formula:

$$f_0 = \frac{1}{2\pi\sqrt{LC}} \tag{2.1}$$

It has been shown in C Radu's PhD thesis [2] that the change detected in the TDO's resonant frequency is proportional to the change in the material's suscep-

[10] Dr. Diaconu's research thesis

tibility via:

$$\frac{\Delta f}{f} \propto \frac{\Delta \chi}{\chi} \tag{2.2}$$

The critical curve can be constructed by performing TDO experiments at different angles in the plane of the sample. In this way, switching information is found at every angle at which the dc field is applied. The switching field is plotted as a point on a polar chart, and each of these is a point on the critical curve. In the TDO the sample is fixed in place within the sensing coil (also fixed) while the dc field is rotated on a plane. The susceptibility observed is a combination of both transverse and longitudinal susceptibilities. This combination still preserves the same singularities characterizing the switching fields.

The schematics of the electric diagram depicted above describes the TDO circuit used for the experiments. The tunneling diode oscillator used in our experiments is derivative of the work of Craig T. Van Degrift [28] and H. Srikanth [32]. Besides that, the configuration and characteristics are mostly original. They were designed and configured by L. Spinu and *et al*.

The crux of the circuit is the tunnel diode marked TD. The diode used for the experiment was manufactured by Aeroflex/Metelics [41]. Model MBD3057-E28X used for our experiments is made of germanium. The tunnel diode possesses a negative slope region where the diode acts as a negative ac resistance that cancels the losses of the LC tank circuit. Characteristics of tunnel diodes do not depend upon magnetic field which makes them suitable over a very wide range of temperature and magnetic field.

The LC tank is comprised of the capacitor C and the inductor L. The capacitor has a capacitance of approximately 39pF while the inductor has an inductance of of 0.2 μH, this results in an operating resonant frequency of approximately 70 MHz. The resistor labelled r, connected in series wit the inductor, indicates the finite resistance of the inductance.

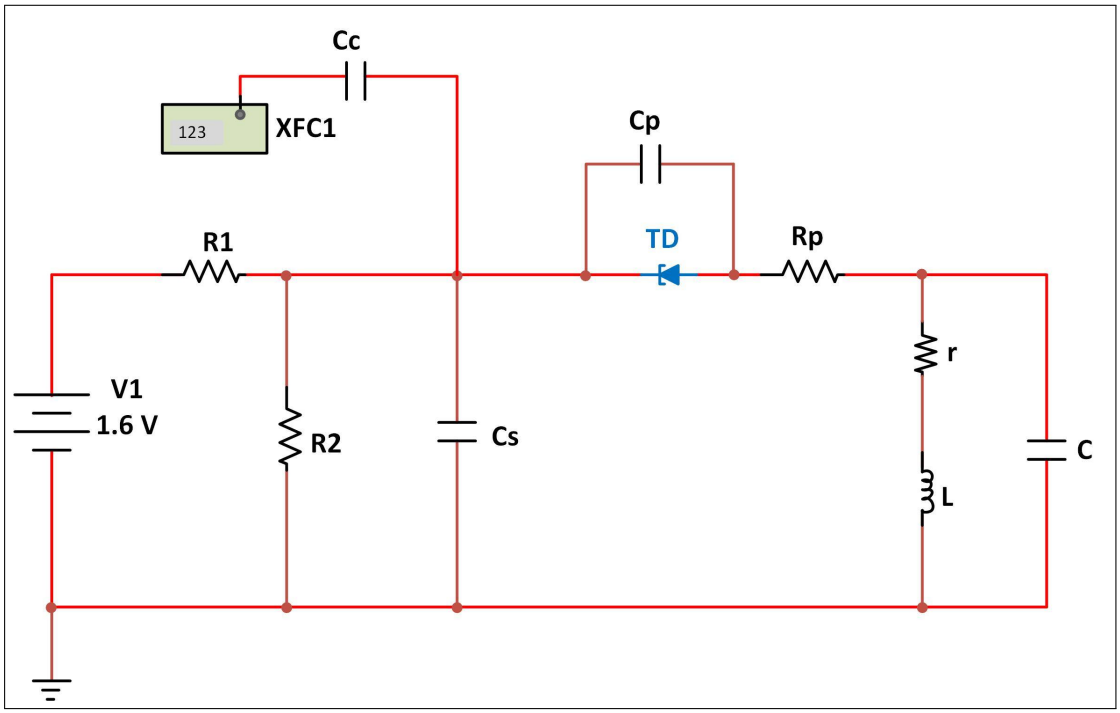

Figure 2.5: Schematic diagram of the tunnel diode oscillator used in our experiments

The output coupling capacitor marked C_c blocks the dc signal but allows the rf signal to pass. The rf signal is then amplified and directed towards the frequency counter. The capacitance of the coupling capacitor was comparatively higher than that of the LC circuit, around 0.1 μF.

The capacitor identified by C_s on the above figure is the bypass capacitor. This capacitor has capacitance high enough to resemble a short circuit at the operation frequency. This component oif the circuit plays a vital role in suppressing the rf noise emanating from the power cables and stopping the transmission towards the dc power supple. The capacitor closes the circuit which results in the separation of the resonant side from the influence of external noise. The determination of C_s (200pF) is a compromise resulting from signal amplitude, external influence and noise.

The capacitor C_p symbolizes the virtual capacitance of the tunnel diode which can be increased by adding a capacitor in parallel with the diode. This optional

use of an additional capacitor can appreciate the rf signal magnitude in the back of the diode and can assist in adjusting the impedance of the diode to match the one of the LC tank.

The resistor marked R1 (22 KΩ) and R2 (390 KΩ) constitute a dc voltage divider. This yields proper dc bias voltage required to obtain the negative resistance region in the tunnel diode.

The parasitic suppression resistor, R_p (47 KΩ) impedes the unintentional oscillations originated from the stray capacitance of the tunnel diode and any inductance from other components. High frequency oscillations can degrade the performance of the circuit.

As established earlier, the tunnel diode is the primary component of the setup. The other devices necessary to acquire a functioning tunnel diode oscillator are tunnel diode's power supply, the frequency counter, the double Helmholtz coil[11], two separate power supplies for the double Helmholtz coil, a 3-D gaussmeter, and of course a functioning computer with the proper programs and softwares. The computer program essentially controls all the variables and records the output data.

Hewlett Packard (predominantly known as hp) Model E3631A triple output DC power supply was used as the power supply for the tunnel diode in the experiments. The E3631A is a high performance 80 watt-triple output DC power supply with GPIB and RS-232 interfaces. The combination of bench-top and system features in this power supply provides versatile solutions for design and experiments. The triple power supply delivers 0 to ± 25 V outputs rated at 0 to 1 A and 0 to +6 V output rated at 0 to 5 A. The ± 25 V supplies also provide 0 to ± 25 V tracking output to power operational amplifiers and circuits requiring symmetrically balanced voltages. We used ± 25 V power supply's output for all the experiments.

[11]The previous experiments used an electromagnet.

The frequency counter used for the experiments was Agilent 53131A 225 MHz Universal Counter. For the Agilent 53131A, frequency and time interval resolutions are 10 digits in one second and 500 picoseconds, respectively. The frequency counter takes in information regarding the frequency of the sample and transmits it to the computer via a GPIB interface. The Agilent 53131A/132A basic measurement functions include Frequency, Period, Pulse Width, Duty Cycle, Rise/Fall Time, Time Interval, Frequency Ratio, Totalize, Phase, and Peak Voltage.

The Helmholtz coil is a novel addition to this setup. The next section goes in depth on this specific apparatus. The power supplies used for the Helmholtz coil are Kepco series Bipolar Operational Power Supply/ Amplifier (BOP). The power supply connected to the bigger set of coils is Model BOP 50-4M. This particular power supply has a maximum DC output of ± 50 V voltage and ± 4 A current. The power supply connected to the smaller pair of coils is of Model BOP 20-10M. This power supply has an output of maximum of ± 50 V voltage and ± 4 A current. Both the power supplies have an output power of 200W.

The 3-D gaussmeter used to calibrate the program and Helmholtz coil was Lakeshore Model 460 3-Channel Gaussmeter. The Model 460 combines the performance of three gaussmeters into one package, making it an excellent value for materials analysis and field mapping applications. It can be can be operated with three individual probes, a single 2-axis probe and one individual probe, or a single 3-axis probe. We used a single 3-axis probe for our experiments. The Model 460 3-channel gaussmeter offers full scale ranges from 300 mG to 300 kG.

The command center of this setup is the computer that reads and controls all the experimental parameters and records the raw data. The computer communicates with all the instruments mentioned above via a GPIB (IEEE 488) interface. In order to automate the experiment, extensive LabView programming was done. The program for the double Helmholtz coil is more automated than the electromagnet because it does not require manual rotation of the sample (electromagnet).

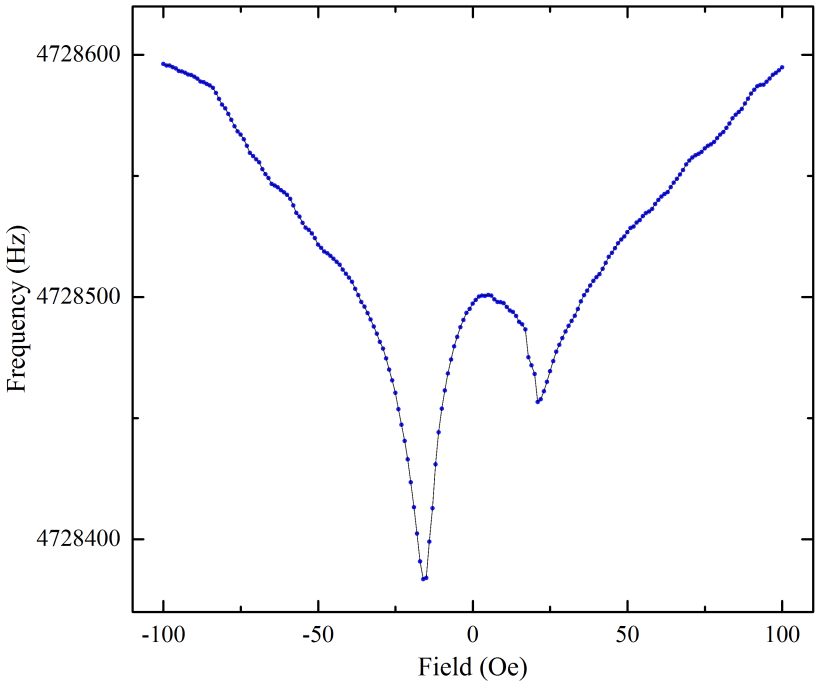

Figure 2.6: A typical data sweep via the Labview program illustrating susceptibility signal given by a FeCoB SAF sample

The LabView program generates a step by step sweep of the dc field while measuring the real magnetic field in the samples space and the resonant frequency of the oscillator.

2.3 Double Helmholtz Coil

Helmholtz coil, named after the renowned German physicist Hermann von Helmholtz, is a device for producing a region of nearly homogeneous magnetic field (Figure 2.8). A Helmholtz coil comprises of two solenoid electromagnets installed on the same axis (Figure 2.7). The distance between two identical coils is equal to the radius of those coils. This characteristics of the Helmholtz coil are depicted in the figures below. Helmholtz coils can also used in scientific apparatuses to cancel external magnetic fields, such as the Earth's magnetic field.

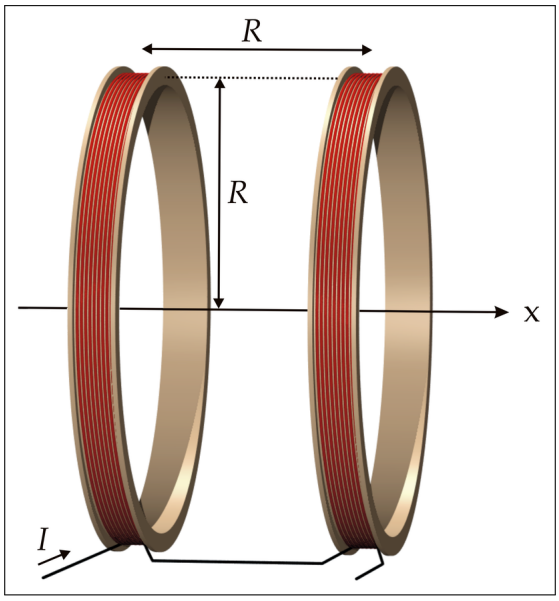

Figure 2.7: The schematic diagram of a a single Helmholtz coil

A Helmholtz pair consists of two identical circular magnetic coils (solenoids) that are placed symmetrically along a common axis. In a double Helmholtz coil there is another pair of identical circular magnetic coils (not identical to the other pair) on an axis perpendicular to the first. The coils on the same axis carry an equal electric current in the same direction. Helmholtz coils use DC (direct) current to produce a static magnetic field. (Figure 2.8)

The double Helmholtz coil used for our experiments was was designed to maximize field using 72 V 6A Kepko Power supplies. Each pair of coils was connected to an independent power supply. The pair of coils on x-axis (arbitrarily marked) are separated by a distance of approximately 18.0 cm. The smaller coils positioned along the y-axis have a radius of approximately 12.0 cm. Despite their size the resistance in both pair of coils is set to be equal by controlling the number of turns and hence the length of the solenoid coil.

The magnetic field generated by the Helmholtz coil is in a strongly linear relation to the coil current. The field strength can be calculated exactly by analytical (or numerical) methods, based on the coils' geometry, the number of turns and

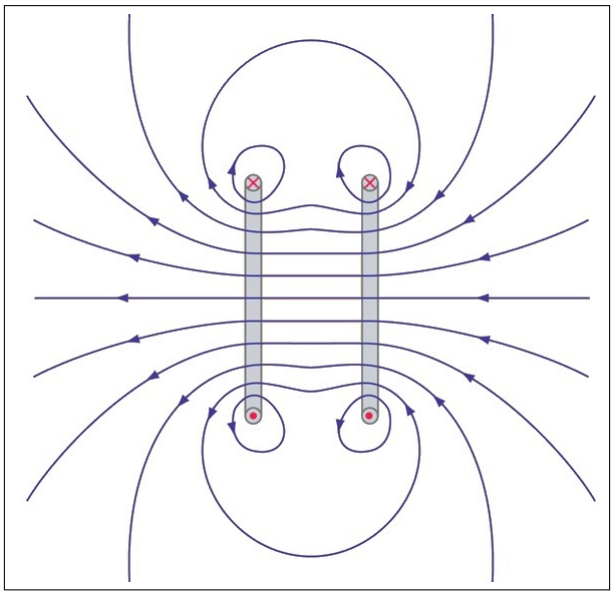

Figure 2.8: Magnetic field lines in a plane bisecting the current loops. The field is approximately uniform in between the coil pair. (In this picture the coils are placed one beside the other; the axis is horizontal.)

the coil current. The calculation illustrated in the appendix gives the exact value of the magnetic field at the center point. If the radius is R, the number of turns in each coil is N and the current through the coils is I, then the magnetic field B at the midpoint between the coils will be given by

$$B = \left(\frac{8}{5\sqrt{5}}\right)\frac{\mu_0 NI}{R} \tag{2.3}$$

where μ_0 is the permeability of free space ($4\pi \times 10^{-7}$ T $\cdot$ m/A).

The Helmholtz coil eliminated the need of physically rotating the electromagnet. This saved time and effort while providing a better result. Since the angle was changed via the Labview program rather than a human intermediary, the error in the angles were significantly reduced. Angles could be varied with a precision of 1 degree, but doing so would be a tedious job culminating in a significant error. The Helmholtz coil does not have this restriction, albeit producing susceptibility measurements for infinitesimally small angle variations will require a large amount

of time to compute the data. So, we varied the angles by 2 degrees which gives comparably enhanced resolution than the 5 degrees variation of the electromagnet.

2.4 Critical Curves via Reversible Transverse Susceptibility Measurements

Transverse Susceptibility was initially explored by Gans in 1909 [15]. The transverse susceptibility (TS) of a material is a measure of the magnetic susceptibility in a direction transverse to an applied bias field, H_{DC} [2]. Arahoni was the first person to mathematically devise a transverse susceptibility tensor almost a half century later in 1957 [16].

Critical curve is a locus of points for which the magnetization reversal occurs. Transverse Susceptibility measurements require two magnetic fields: a DC field H_{DC}, and a small perturbing AC field h_{AC} applied at a right angle to the DC field. Aharoni's model can be employed to deduce that the transverse susceptibility signal would show sharp peaks when the DC field was equal to the sample's anisotropy field or easy axis. This has been proved theoretically and experimentally to be a viable technique for measuring anisotropy of particulate structure. If the DC field is assumed to be applied along the z-axis and the AC field along x-axis of a Cartesian reference system, the susceptibility measured along the x axis is in fact the transverse Susceptibility as shown in the figure.

The reversible transverse susceptibility for small ac field frequency variations that still preserve equilibrium is given by [17]:

$$\chi_{xx} = \frac{M^2}{E_{\theta\theta}E_{\phi\phi} - E_{\theta\phi}^2}\left[\sin^2\theta_M \sin^2\phi_M E_{\theta\theta} + \frac{\sin 2\theta_M \sin 2\phi_M}{2}E_{\theta\phi} + \cos^2\theta_M \cos^2\phi_M E_{\phi\phi}\right] \tag{2.4}$$

where θ_M and ϕ_M are the equilibrium polar and azimuthal angles of magnetization vector $\mathbf{M}$, respectively. $E_{\theta\theta}$, $E_{\phi\phi}$, and $E_{\theta\phi}$ are the second derivatives of the free

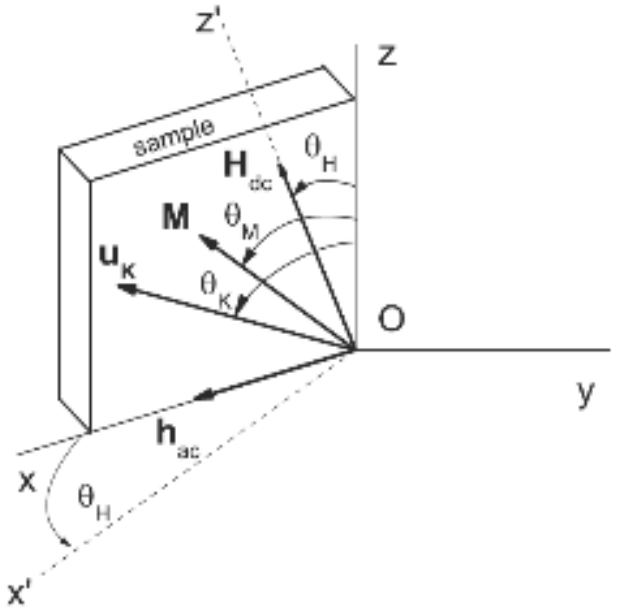

Figure 2.9: Schematic of the coordinate system for thin-film samples.

energy density. This equation shows that TS can be used for probing the switching field since the denominator, $E_{\theta\theta}E_{\phi\phi} - E_{\theta\phi}^2$, is the curvature of the free energy surface at equilibrium. The points for which the denominator is zero are the critical points of transition from one minimum to the other, i.e., the switching points.

The critical curve for a uniaxial system can be acquired through the susceptibility signal measured along 0x axis while the DC field H_{DC} is applied along different directions, θ_H, in the sample's plane. The detected signal for each field orientation shows a sharp peak located at the field values associated with the singularity in the detected signal. This process is illustrated in the figure below.

The critical curve is obtained by plotting the switching field values H_S (θ_H) in polar coordinates. The critical curve could be obtained using only one DC field sweeping direction (either increasing or decreasing) while θ_H was varied through 0° to 360°. However, by using the values of H_S determined from both susceptibility

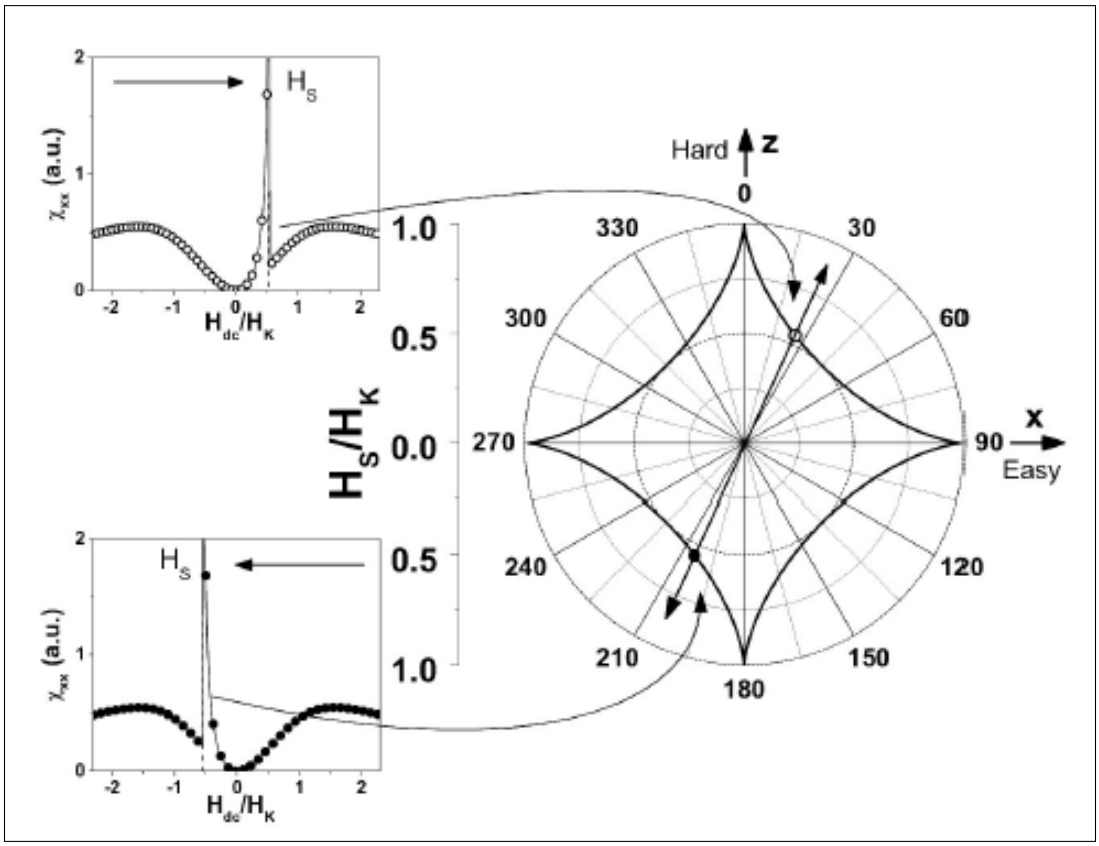

Figure 2.10: Left: Susceptibility signal χ_{xx} detected along the 0x axis, for increasing (top) and decreasing (bottom) field sweeping for $\theta_H = 25$ and $\theta_K = 90$. Right: Theoretical critical curve (astroid) determined from susceptibility measurements for a uniaxial anisotropy system [18]

curves corresponding to increasing and decreasing fields, it is possible to reduce the angular domain for θ_H to $(0°, 180°)$. Thus, the right half of the critical curve will be obtained from the increasing DC field curves while the left half from the decreasing DC field curves.

3 Static Critical Curves of Synthetic Antiferromagnets

The following chapters will focus on coupled magnetic multi-film structures. Considerable research and exploration has been done in the world of single film nanostructures, but recently muti-layered thin films have gotten more attention because of their unique properties. Two films that are superposed in closely spaced parallel space are separated enough to avert atomic interaction but compact enough to warrant magnetostatic interaction. The magnetostatically coupled thin films divulge static (and dynamic) behaviors substantially different from single layered thin films.

This chapter will primarily focus on Synthetic Antiferromagnets. Synthetic Antiferromagnets (often abbreviated as SAF) are magnetic materials where the antiferromagnetic characteristic is induced through the coupling of two or more thin ferromagnetic layers separated by a nonmagnetic layer. Synthetic antiferromagnets are in all essence artificial antiferromagnets without the presence of any categorical antiferromagnetic material.

SAF structures have considerable technological applications which makes the study of these structures academically and financially viable. SAF are frequently exploited for hard layer of coupled composite media [42], soft under-layer for perpendicular recording [43], pinned and free layers for toggle MRAM cells [44], hard disks reading heads, and magnetic sensors [45].

3.1 Synthetic Antiferromagnet Concepts

Synthetic antiferromagnets (SAF) are basically a sandwich between two ferromagnetic thin films [46]. The ferromagnetic samples are separated by a nonmagnetic metallic spacer, usually Ruthenium (Ru), Osmium (Os), Rhenium (Re), Chromium (Cr), Copper (Cu), or Rhodium (Rh)[12]. The thickness of each layer is

[12]Most of them are transitional metals

coordinated to provide the required antiferromagnetic coupling.

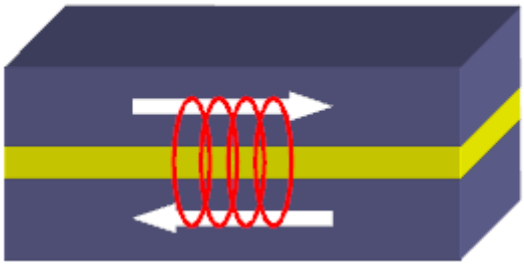

Figure 3.1: Schematic representation of the SAF showing the two ferromagnetic layers antiferromagnetically coupled through an interlayer of non-magnetic material.

Layered structures coupled through Ruderman–Kittel–Kasuya–Yosida (RKKY) interactions such as synthetic antiferromagnets (SAF) have been particularly interesting due to controllable coupling strength. Ruderman–Kittel–Kasuya–Yosida interaction refers to a coupling mechanism of nuclear magnetic moments or localized inner d- or f-shell electron spins in a metal by means of an interaction through the conduction electrons.[13]. The RKKY interaction was originally theorized by M. A. Ruderman and Charles Kittel of the University of California, Berkeley. Tadao Kasuya from Nagoya University and Kei Yosida of the University of California, Berkeley expanded the theory into its current form.

The indirect exchange couples over immense distances in SAF structures. There is almost considerably low or no direct overlap among neighboring magnetic electrons in metals which makes interactions as such dominant exchange interaction. The exchange acts via a mediator; the conduction electrons (itinerant electrons) for metals. The interaction is characterized by a coupling coefficient, j, formulated as [103, Pham]:

$$j(R_l - R_{l'}) = 9\pi \frac{j^2}{\epsilon_F}(2k_F|R_l - R_{l'}|) \tag{3.1}$$

[13]This is why the non-magnetic metallic spacer used is transitional metal

where R_l and $R_{l'}$ are the lattice positions of the point moment, ϵ_F is the Fermi energy, k_F is the radius of the conduction electron Fermi surface, and F is dependent of the length x by:

$$F(x) = \frac{x\cos x - \sin x}{x^4}$$

The RKKY exchange coefficient, j, oscillates between positive and negative values as the separation length, x, increases. The exchange coefficient has damped amplitude as the oscillations proceed. This behaviors of the coefficient is apparent in the figure below. Therefore, a magnetic coupling can either exhibit ferromagnetic or antiferromagnetic characteristics depending upon the separation between a pair of ions. A magnetic ion induces a spin polarization in the conduction electron in its neighborhood. This spin polarization in the itinerant electrons is felt by the moments of other magnetic ions within range, leading to an indirect coupling.

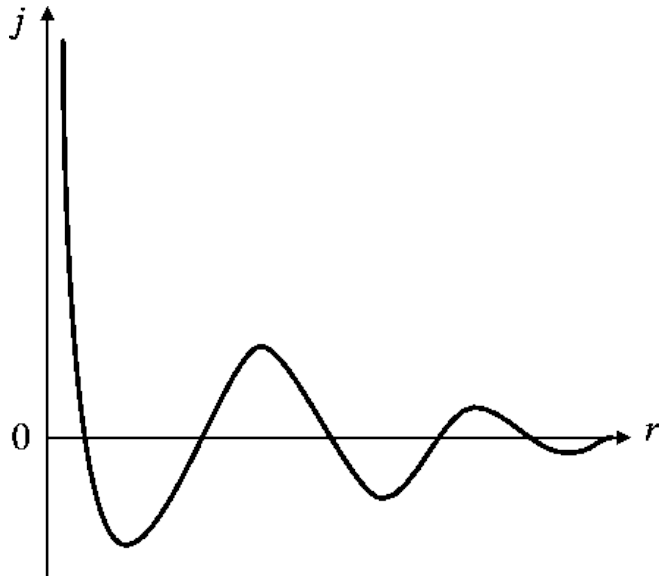

Figure 3.2: Variation of the indirect exchange coupling constant, j , of a free electron gas in the neighborhood of a point magnetic moment at the origin r = 0 [47]

In rare-earth metals, whose magnetic in the $4f$ are shielded by the $5s$ and $5p$ electron. This results into a considerably weak and insignificant direct exchange. The indirect exchange still produces magnetic order via the conduction electron

in these materials.

The SAF samples (as the name would suggest) are designed with separation distance that would demonstrate antiferromagnetic coupling. The physical structure for synthetic antiferromagnets is fairly uncomplicated, regardless SAF is a crucial component of modern magnetic devices with rather sophisticated magnetic behavior.

3.2 Synthetic Antiferromagnets Samples

The SAF samples used to perform the experiment have been used for numerous papers characterizing their various properties throughout last decade by Dr. Spinu and his team. Dr. Ganping Ju from Seagate Technology, Pittsburgh, PA provided the aforementioned samples. The fact that the same samples have been used to contribute such a vast number of scientific papers with novel and exciting conclusions shows how important this field of study is and how much more research is possible in this intriguing sector of nanostructures.

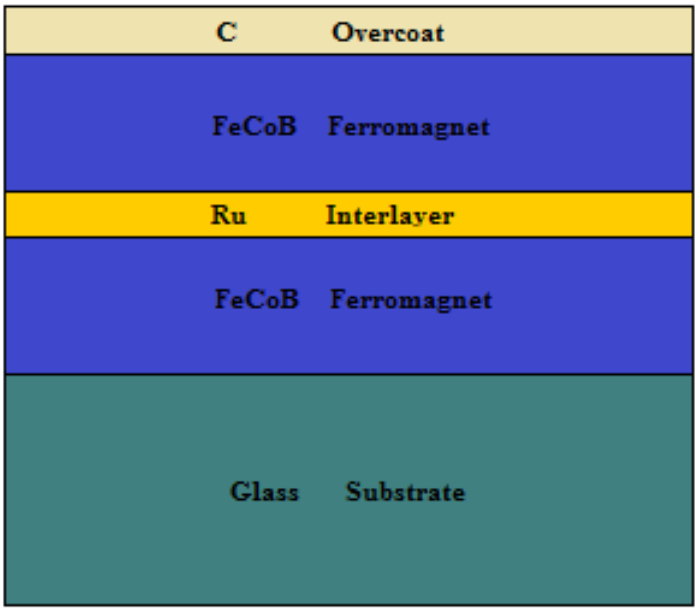

Figure 3.3: SAF samples structure (not to scale)

The SAF samples analyzed were mutilayered thin films structures deposited on a glass substrate. A series of trilayer films of FeCoB/Ru/FeCoB were used. The bottom layer deposited directly over glass substrate is a ferromagnetic layer of FeCoB. The second layer above the FeCoB is a Ru, a non-magnetic metal. On top the non-magnetic spacer is another layer of the ferromagnetic material FeCoB, which is then coated by a layer of carbon (C) to protect the surface from scratches and other minimal damages.

The SAF samples were deposited with a DC magnetron sputtering with a base vacuum pressure below 3×10^{-9} Pa. This process was done at room temperature, with no direct manipulation of temperature. The full thickness of the three-layer samples was approximately 30 nm. Each sample was scrupulously cut in square structures of 5 mm $\times$ 5 mm.

The thickness of each layers (of FeCoB and the Ru) were varied to produce multiple samples. The Ru spacer thickness extended from 0.8 nm to 2 nm. The exact structure that would present with an antiferromagnetic coupling wasn't determined beforehand so it was necessary to produce several series of samples. Among the three varying thicknesses of ferromagnetic layer, the thickness of the Ru layer was manipulated to observe antiferromagnetic coupling.

Among the varied samples only few could be categorized as synthetic antiferromagnets. In the group of SAF structures, only the ones that show substantial SAF behavior were chosen for our experiment. Hysteresis curves, along different directions in the plane of the samples were measured via a vibrating sample magnetometer (VSM) as shown in the following figure. After determining the coupling for the structures using hysteresis loops, the experiment proceeded towards measurement of susceptibility in order to determine the switching characteristics.

3.3 Major Hysteresis Loop of SAF

The samples used for this experiment have equal thickness of FeCoB layer with varied Ru thickness. Four out of seven available samples were studied to observe SAF characteristics. The first sample with Ru thickness 8 Å displayed ferromagnetic characteristics. The samples with Ru thickness 14 Å and 16 Å were found to be coupled antiferromagnetically. The final sample of the series, with Ru thickness 18 Å, shows antiferromagnetic coupling with asymmetric layer switching.

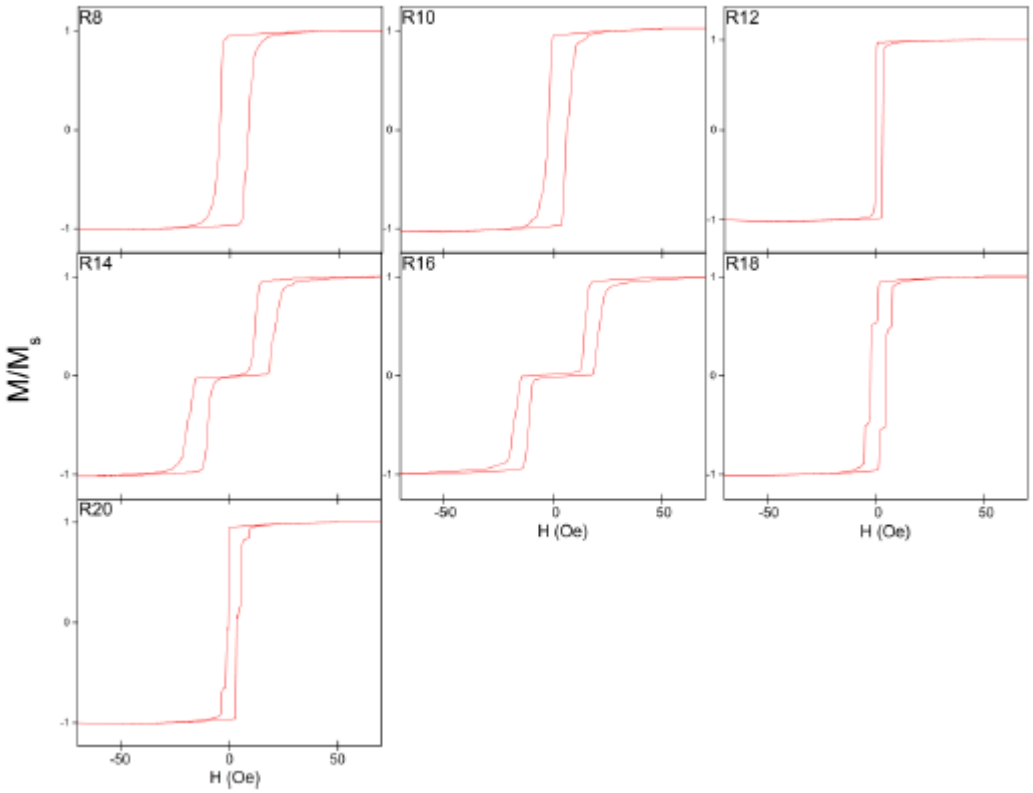

Figure 3.4: MHL of all SAF samples in the series. The applied field is along the easy axis in all MHLs. J is observed to move from positive to negative and back towards positive again as Ru thickness increases [48].

The samples were placed in-plane parallel to external magnetic field direction and field was swept from -250 Oe to 250 Oe with field steps of less than 1 Oe. It was observed that the magnetic coupled structures displayed antiferromagnetic

behavior as the thickness of the Ru layer was increased. The structures exhibited ferromagnetic characteristics after a certain thickness of the Ru layer.

The two samples that featured antiferromagnet coupling were studied more thoroughly. The VSM assisted in identifying the easy axis for the samples. The hysteresis for both the samples were acquired from 0° to 360° with 2° step, but for our research purposes 0° that corresponds to the easy axis, and 90° that corresponds to hard axis are of crucial interest.

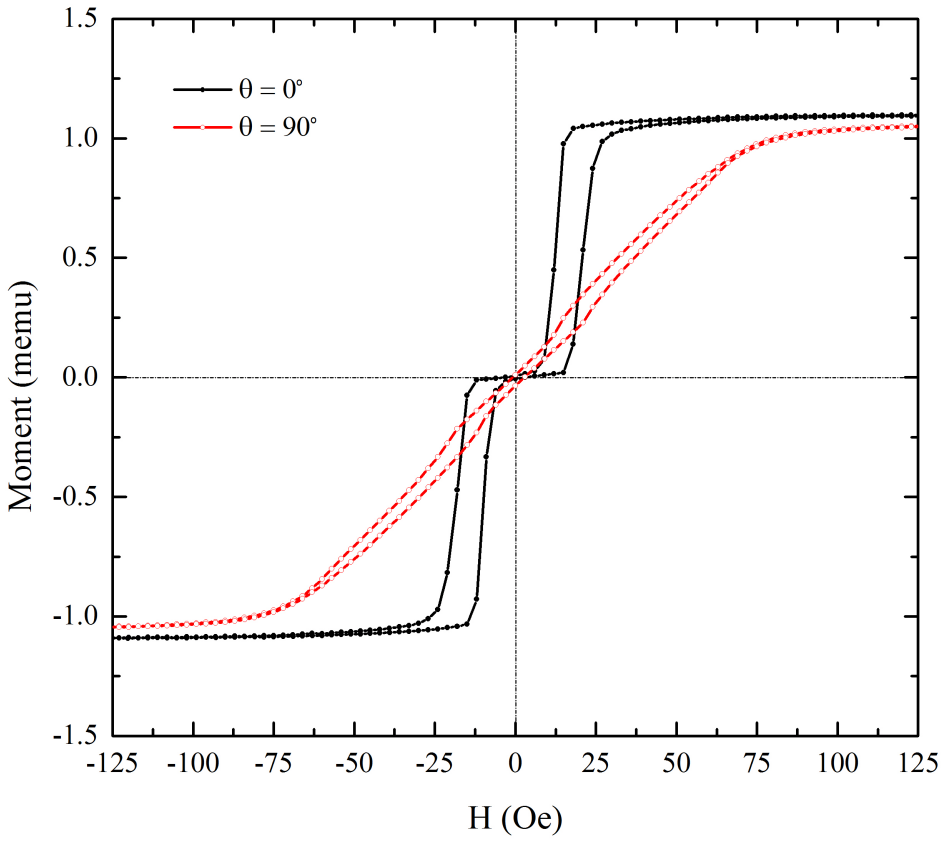

Figure 3.5: MHL for SAF, with Ru thickness 14 Å, displaying easy axis and hard axis.

The two figures above represent the major hysteresis loop for the two antiferrmagnetically coupled samples. This antiferromagnet samples display a unique

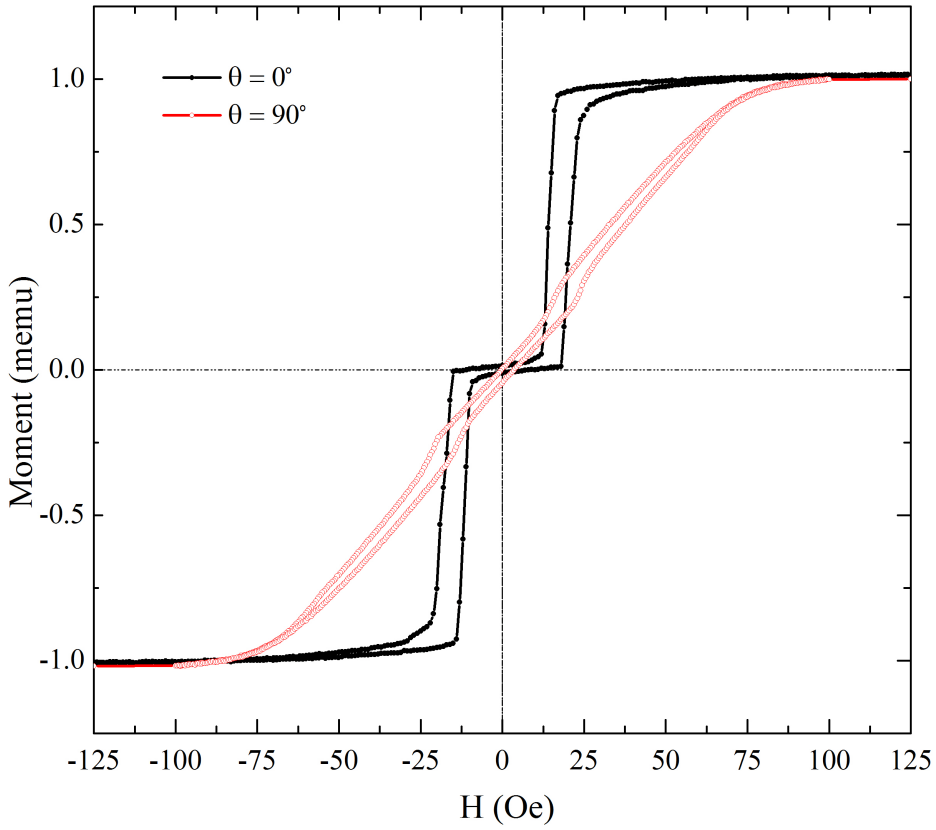

Figure 3.6: MHL for SAF, with Ru thickness 16 Å, displaying easy axis and hard axis.

hysteresis along the easy axis which is the defining characteristic of a synthetic antiferromagnet. The hysteresis loop along the hard axis is that of a typical antiferromagnet. The hysteresis loops also determined that the saturation field for these samples were comparatively low, around 80 Oe for angular orientation. This made it possible to use the TDO in conjunction with the double Helmholtz coil.

The MHLs, along the easy and hard axis, are centered on the y-axis. This tells us there is no bias.

3.4 Static Critical Curve of SAF

The samples were marked in the direction of easy bias after observing their major hysteresis loop. This provided a reference coordinate frame to conduct the susceptibility measurements via the TDO. The sample was carefully placed inside the coil of the TDO system. The sample fixed such that the easy axis of the sample was perpendicular to the AC magnetic field produced by the coil. The initial condition, at 0° was set such that the AC field was perpendicular to the DC magnetic field produced by the double Helmholtz coils. This implies the easy axis was in the same direction as the DC magnetic field.

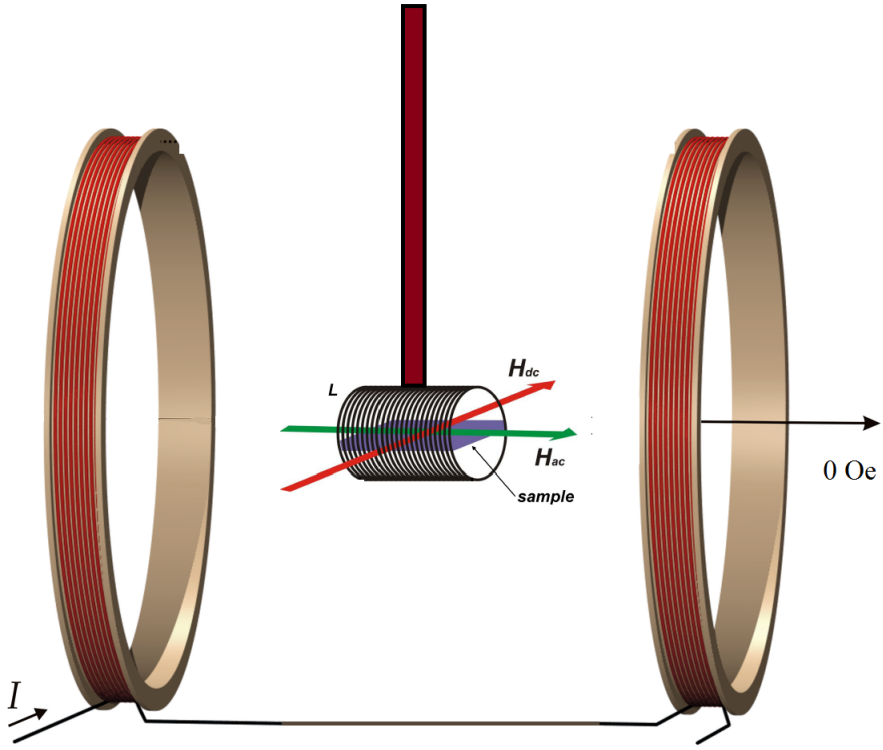

Figure 3.7: Sample placed inside the measuring coil L with the ac and dc fields in plane. The green arrow and the red arrow are perpendicular to each other. The setup shows only one pair of the Helmholtz coils, the pair coils producing the dc magnetic field is laced in and out of the plane of the paper.

Figure 3.7 shows that initially one pair of the Helmholtz coil is kept at zero magnetic field. The DC field present at 0° is solely due to the other pair of coils. The sample was placed such that the easy axis aligns with the H_{dc} (the red arrow in the figure).

After successfully aligning the sample in the appropriate orientation with respect to the coil all the other equipment are turned on. In order, the two Kepco power supplies, the power supply for the TDO and the frequency counter are switched on. The TDO power supply is set at 12 V for this particular TDO circuit. The Labview program is run.

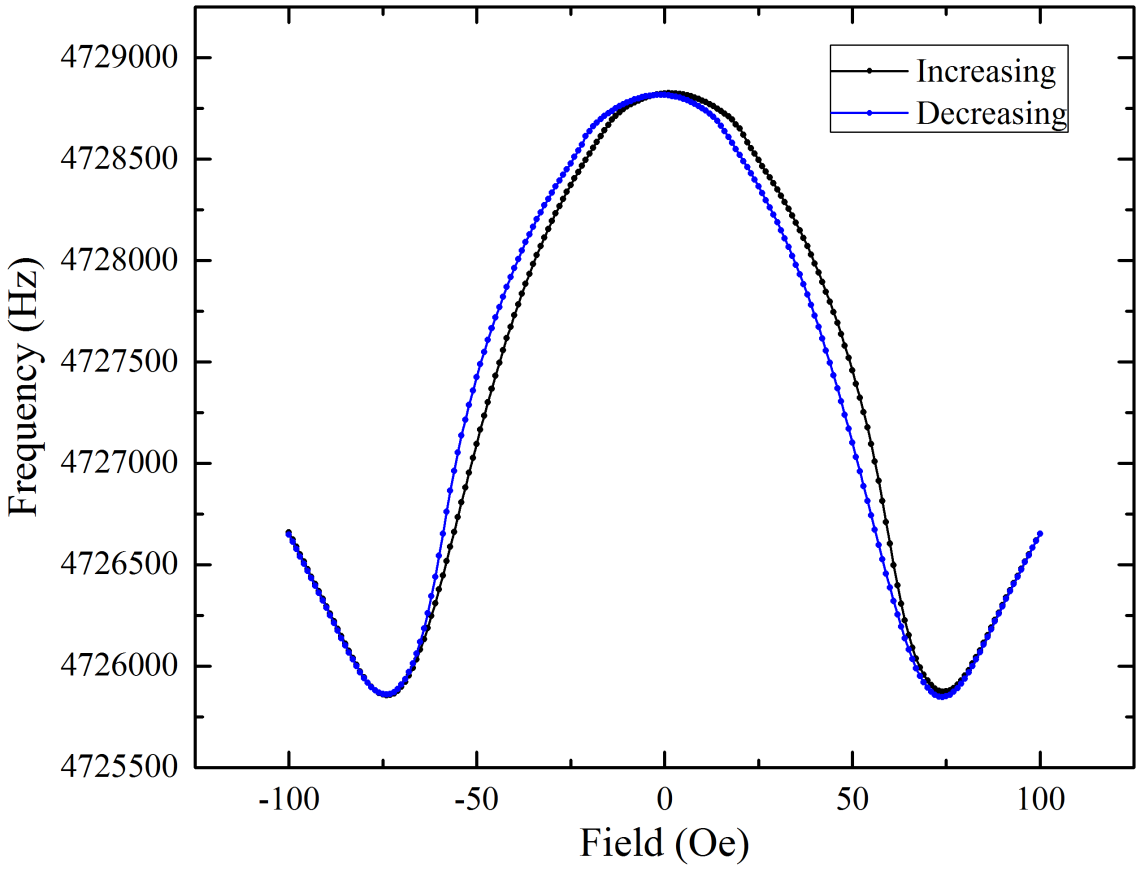

Figure 3.8: Magnetic susceptibility for R16 sample at 0° orientation. The two minimum are the susceptibility values used to create the critical curve.

The Labview program was run from -100 Oe to +100 Oe once (increasing

magnetic field), and back to -100 Oe (decreasing magnetic field). The field step used was 0.25 Oe which is a significant improvement for resolution compared to the old TDO setup using the electromagnet. As mentioned before in Chapter 1.9, the TDO was run from 0° to 180° acquiring susceptibility for increasing and decreasing magnetic field. This helps us create the entire polar critical curve. The angle was increased by two degrees. Data collected from 91 orientation gives us a critical curve.

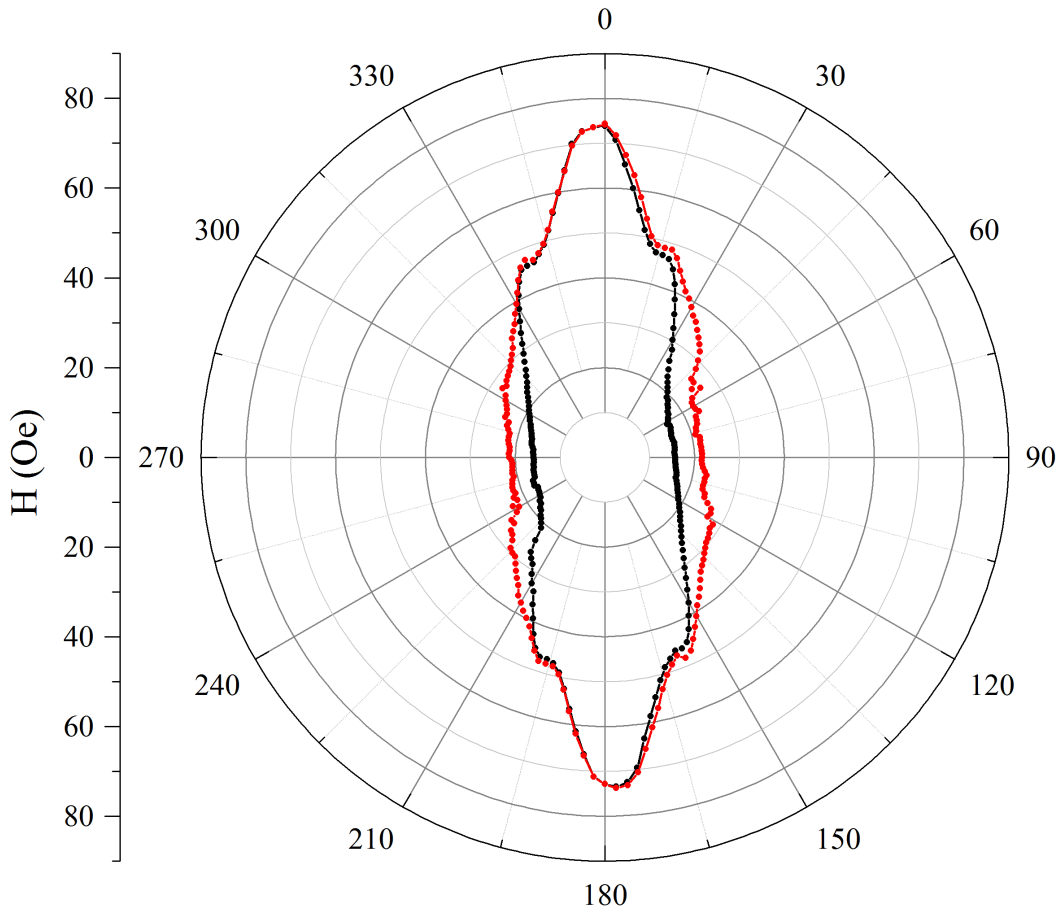

Figure 3.9: Experimental static critical curve for sample with Ru thickness 16 Å determined from TDO susceptibility's curves.

There is a possibility of human error while collecting data for the critical curve via the susceptibility measurements. To check that, the collected data is valid,

a new set of data is collected by differentiating the susceptibility measurements. The figure below shows the differentiated susceptibility graph. The critical curve obtained via the new set of data is close to the original critical curve. This can be done in order to avoid any error in data collection.

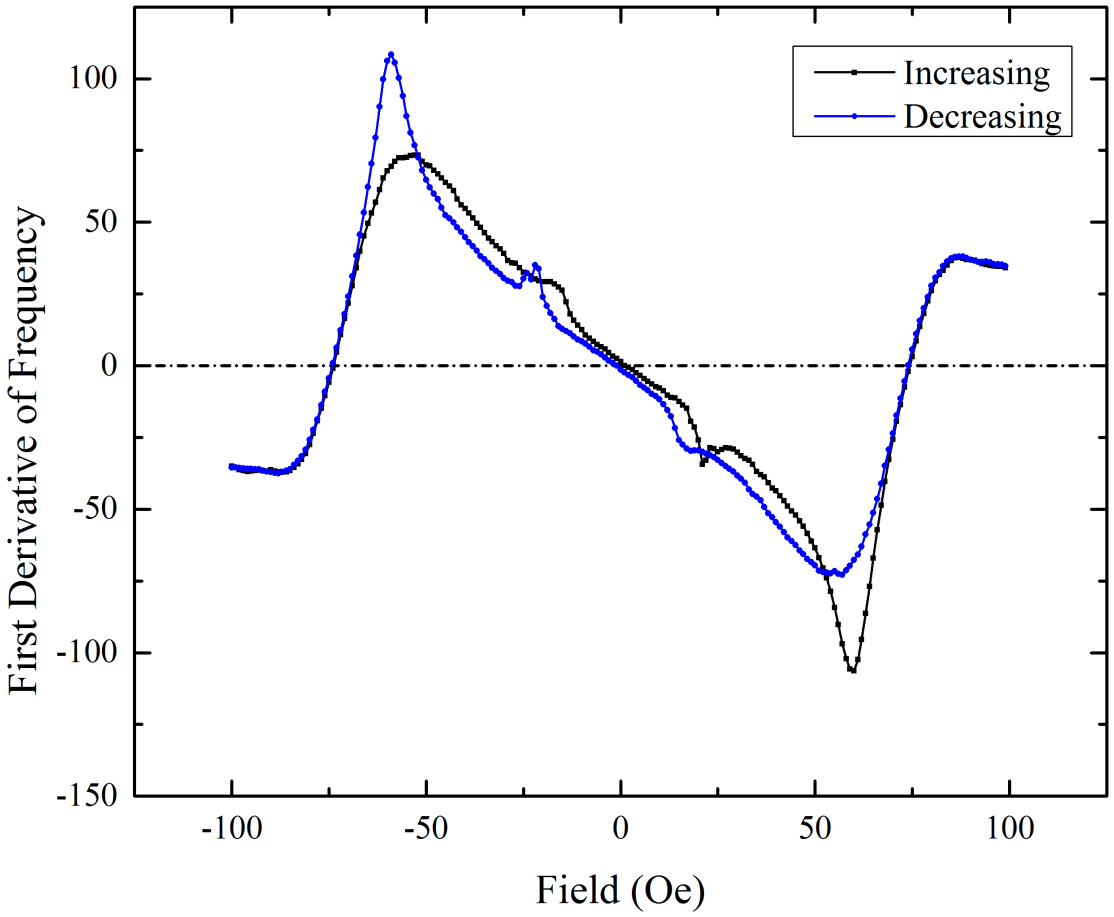

Figure 3.10: The graph obtained from the first derivative of the susceptibility measurements.

The point where the graph crosses the x-axis are the the required data points for the critical curve. It can be observed that there are three such points, but we are only interested in the right and left one. The middle one corresponds to the maximum of the original susceptibility graph.

The original critical curve is still in black and red color as the previous curve. The data points colored in purple and neon overlap the original data point. This shows that the human error, if present, is constant in the least.

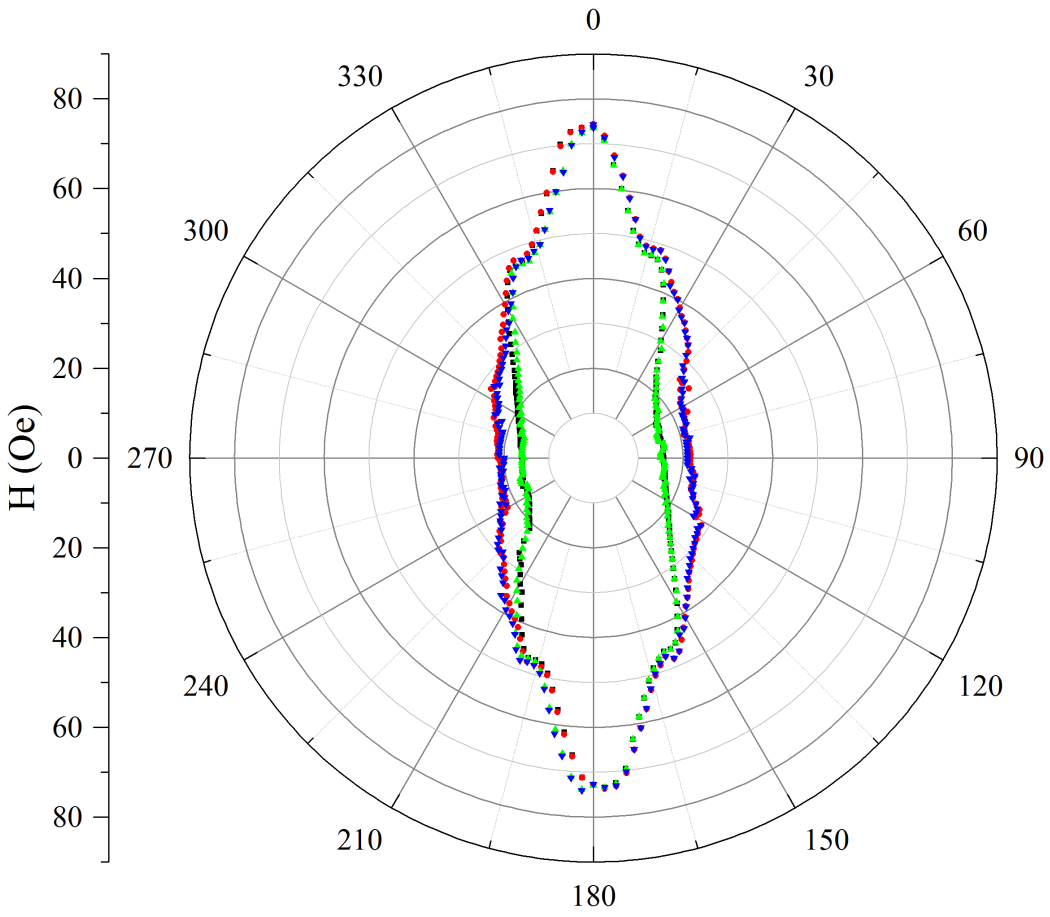

Figure 3.11: Critical curved obtained through two different data acquisition methods overlapped over each other. It shows the error in this step is minimum.

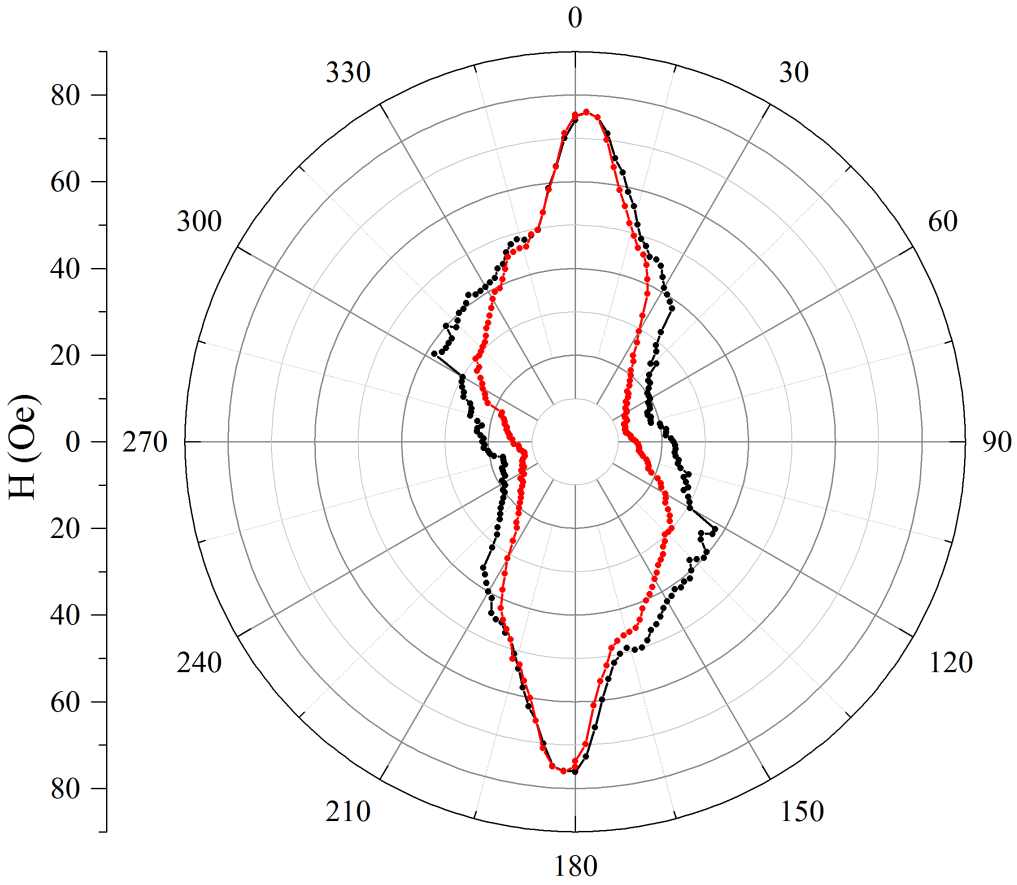

Figure 3.12: Experimental static critical curve with Ru thickness 14 Å determined from TDO susceptibility's curves.

4 Static Critical Curves of Exchange Bias Samples

4.1 Introduction

The remarkable physical phenomenon aptly named exchange bias ensues from the exchange anisotropy at the interface between a ferromagnetic material and an antiferromagnetic material. Exchange bias or exchange anisotropy occurs in bilayers (or multilayers) of magnetic materials where the hard magnetization behavior of an antiferromagnetic thin film causes a shift in the soft magnetization curve of a ferromagnetic film.

Exchange anisotropy was discovered by Meiklejohn and Bean [49] of General Electric in 1956. They happened upon this while studying Co particles embedded in their native AFM (CoO). The exchange bias is prevalent in varying interfaces including but not limited to small particles, inhomogeneous materials, and thin films. Recently, thin films have accumulated a massive research because of their application in magnetic recording devices. And as it is, we will be using thin films for this particular research, too.

When an antiferromagnetic and ferromagnetic phase coexist in a single structure the hysteresis loop of the ferromagnetic material shifts on the H-axis. This phenomena is a defining characteristic of exchange bias and can be observed through the VSM. The phenomena is clearly illustrated in the figure 4.1. The hysteresis loop presented in the figure is purely theoretical, experimental data vary to some extent [50, 51].

When a ferromagnet is simply grown on top of an antiferromagnet the exchange coupling between the two systems only leads to an increased coercivity of the ferromagnet. This is usually attributed to the increased coercivity of interfacial spins which needs to be dragged around by the external field. However,

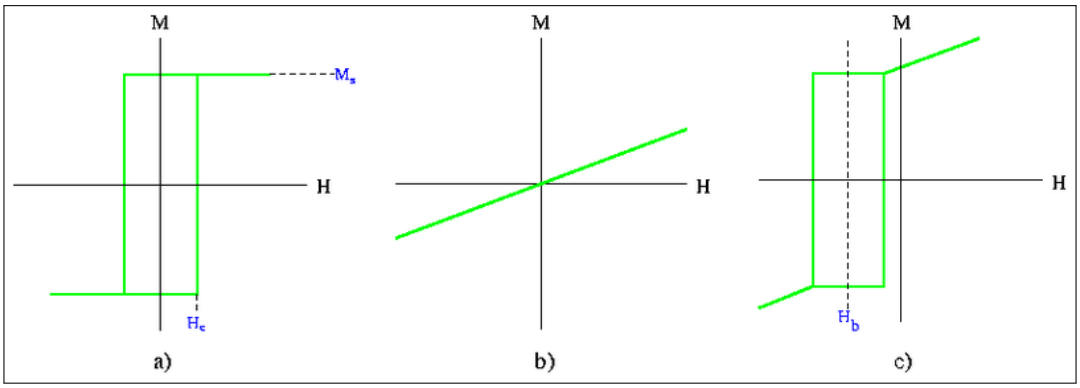

Figure 4.1: Easy-axis magnetization curves of a) a soft ferromagnetic film; b) an antiferromagnetic film and c) an exchange-biased bilayer consisting of a ferromagnet and an antiferromagnet. The susceptibility (slope) of the antiferromagnetic's magnetization curve is exaggerated for clarity.

the ferromagnetic hysteresis loop is still symmetric, indicating two equivalent easy directions. However if the system is grown in a magnetic field or after growth is annealed in a magnetic field to temperatures above the Néel temperature, the hysteresis loop becomes asymmetric and is shifted from zero (Fig. 4.1 (c)). This unidirectional shift is called exchange bias and reflects the fact that there is now a preferred easy magnetization direction for the FM.

Exchange bias effect has tremendous impact on technological applications. One of them is that this effect can be used as sensor to read and write data in magnetic memory [52].

A complete theoretical explanation of the phenomenon of exchange bias has remained a formidable challenge to condensed matter theorists since its discovery. A paper by Miguel Kiwi [50] explores some of the obstacles present in the development of theories that could provide a satisfactory comprehension of the phenomenon. The paper reviews and critically discusses the activities that have acquired considerable attention in the theoretical front. Finally, an evaluation of the progress made, and a critical assessment as to where we stand nowadays along the road to a satisfactory theory, is presented. The author concludes that there are many systems that exhibit exchange bias and it is quite likely that no single

theory will be able to properly fits and describes all of them.

This experiment does not attempt at providing a theoretical explanation of the exchange bias or its properties. The TDO and VSM are used to inspect the static properties of the magnetic nanostructure. We use the TDO as before to measure the susceptibility and produce a viable critical curve for the exchange bias samples.

4.2 Exchange Bias Samples

Our research group has always been interested in the phenomena of exchange bias. Dr. Spinu and his previous students have published multiple papers regarding exchange bias. Most of the research work done prior was with exchange bias in $(NiFe/IrMn)_n$ multilayer films.

The materials considered in this experiment were provided by Paula Kern, a PhD student from Federal University of Santa Maria. Paula came to work with Dr. Spinu's group via student exchange program in 2017. The exchange bias samples were studied using the equipment present at the AMRI laboratories and under the tutelage of Dr. Spinu. The exchange bias sample in question is only bilayer unlike the sample Dr. Spinu had previously employed in his experiments. The compounds used to construct the exchange bias coupling is also different from the ones we have been using the lab.

The exchange bias samples under study for this particular set of experiments are a simple bilayer of $Ni_{81}Fe_{19}$ and $Fe_{50}Mn_{50}$. The base layer is ferromagnetic NiFe and the antiferromagnetic layer, FeMn, is deposited above that. The thin film is deposited over a silicon (100) substrate. A 15 nm thin layer of Tantalum (Ta) was deposited over the silicon substrate. The seed layer of Ta promotes the growth of the ferromagnetic NiFe (111) texture. This crystal structure hence paves the path[14] for the crystallization of the antiferromagnetic FeMn (111) texture.

[14] Quite literally and figuratively.

Another layer of Ta is used as a protective coating on top of the antiferromagnetic layer FeMn. The 15 nm thick layer of Ta protects the otherwise exposed layer of FeMn from oxidization.

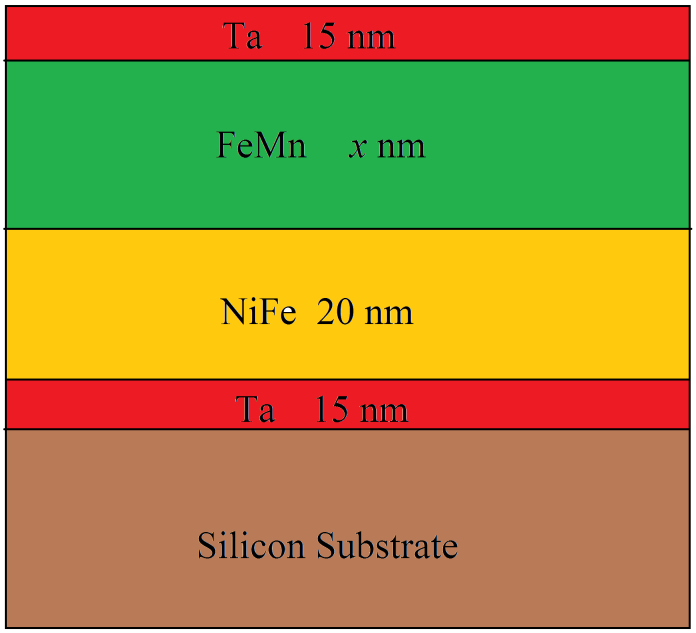

Figure 4.2: Exchange bias samples structure (not to scale)

The exchange bias samples were fabricated via a DC magnetron sputtering system. The base vacuum pressure set was considerably higher than those of SAF samples. The samples were deposited at a base pressure of 5.5×10^{-6} Torr[15]. 2 mTorr Argon pressure was maintained during the deposition of the samples. In order to define the pinning direction a magnetic field of one kOe was applied in the samples' plane during the deposition.

The samples were conceived to investigate the effects of varying antiferromagnetic thickness layer in a bilayer exchange bias sample. Nine exchange bias samples

[15] 1 Torr = 133.322 Pascal

were created with the above deposition technique. All the samples have a constant ferromagnetic thickness of 50 nm NiFe. The ferromagnetic layer of FeMn varies from 3 nm to 30 nm. The samples with major hysteresis loop showing significant exchange bias properties were used for further experiments.

4.3 Major Hysteresis Loop of Exchange Bias Samples

As with Chapter 3.3, major hysteresis loop were obtained via a VSM through the same parameters. The MHL helps to identify the exchange bias nature of the samples and determine an easy axis. The hysteresis loops are determined by the saturation point of the samples to be less than 100 Oe, which meant we could use the double Helmholtz coils for the susceptibility measurements.

Although all the measurements were taken with the same parameters, some of the graphs are scaled down to provide a better view of the major hysteresis loop. The saturation point of the samples varied depending on the thickness of the FeMn layer and this was done to accommodate that. The y-axis is normalized magnetization vector. Exchange bias is present in almost all samples; albeit negligible for the sample with FeMn thickness of 3 nm.

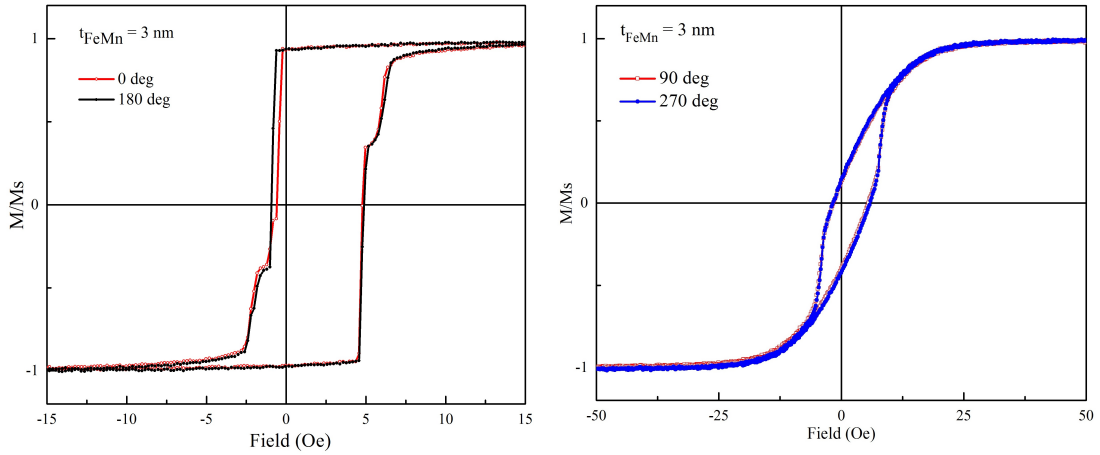

Figure 4.3: MHL for FeMn thickness 3 nm at four different angle orientation that determines the easy axis and hard axis.

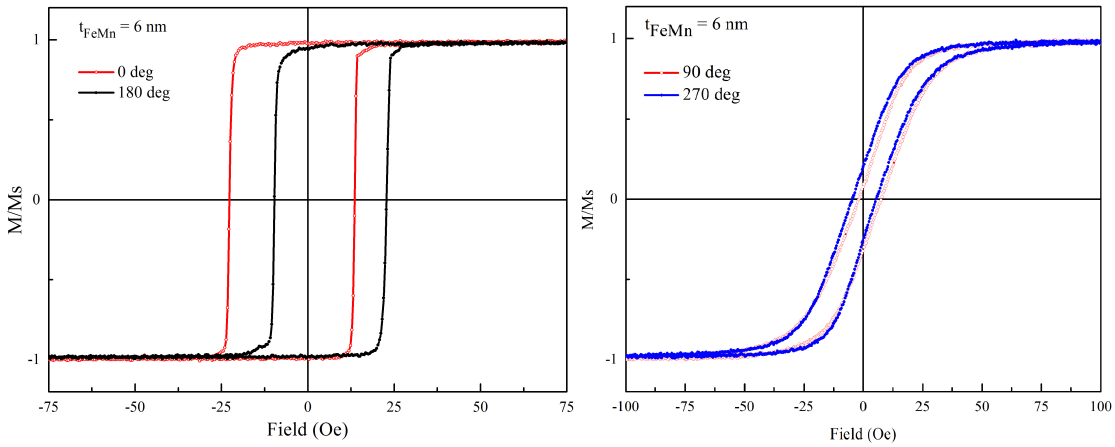

Figure 4.4: MHL for FeMn thickness 6 nm at four different angle orientation that determines the easy axis and hard axis.

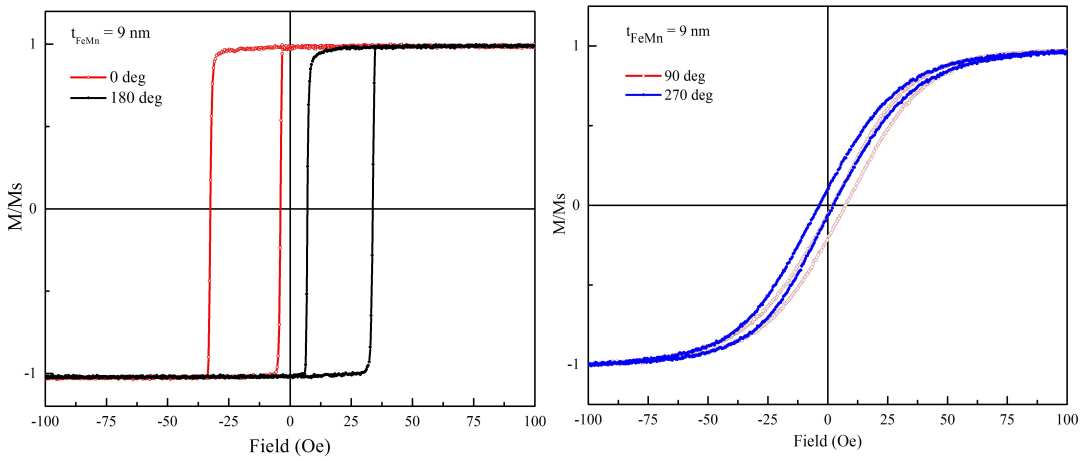

Figure 4.5: MHL for FeMn thickness 9 nm at four different angle orientation that determines the easy axis and hard axis.

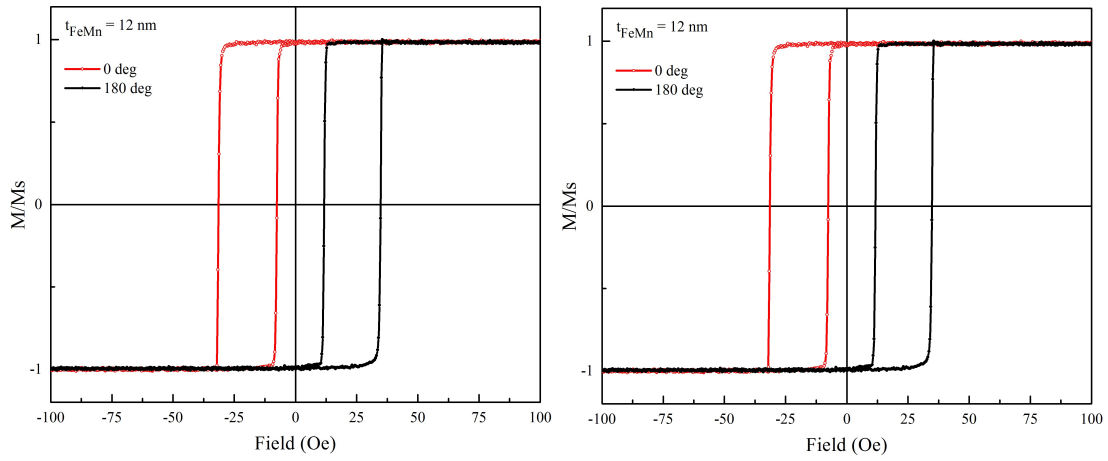

Figure 4.6: MHL for FeMn thickness 12 nm at four different angle orientation that determines the easy axis and hard axis.

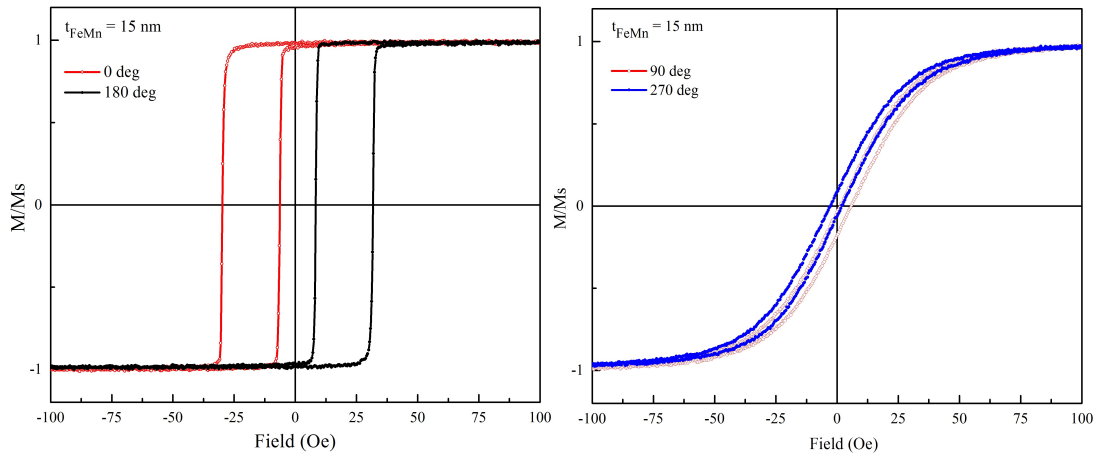

Figure 4.7: MHL for FeMn thickness 15 nm at four different angle orientation that determines the easy axis and hard axis.

The major hysteresis loop for some of the sample along the 90° and 270° were not identical. The MHL along the hard axis not being identical implies that the anisotropy axis an the exchange bias are not perfectly aligned on microscopic level. We are currently working on a method to mathematically calculate the angular difference between the anisotropy axis and the bias via the MHL. [53]

The other four samples, with FeMn thickness of 7.5 nm, 18 nm, 20 nm, and 30 nm, also display exchange bias characteristics. We only chose to study the above five samples with a constant variation of 3 nm in the antiferromagnetic layer. This should help us in devising a mathematical model to further understand the esoteric and quixotic theory of exchange bias that has been eluding physicists for so long.

Conclusions

This thesis is based on experimental research methods that can help us identify different magnetic characteristics of two different type of coupled thin films, synthetic antiferromagnetic and exchange bias samples. We have explored two different techniques that provide static measurements for the magnetic samples. The vibrating sample magnetometer is an excellent piece of equipment to measure the major hysteresis loop. The tunnel diode oscillator has been proven theoretically and experimentally (for different samples) to be a viable method for vectorial mapping using the reversible susceptibility tensor.

The thesis provides a proved and tested method to determine the static critical curve of a structure. The method is based on reversible susceptibility's singularities detection. Magnetic field is swept along easy axis, in both positive and negative direction. The easy axis is determined via the MHL. By performing susceptibility measurements along different angles with respect to the easy axis, the critical curve can be determined.

An extensive programming effort was dedicated to the computer assisted operation of the TDO-based experiments and the result being a user friendly, versatile and error proof research instrumentation. The addition of the double Helmholtz coil provided a novel and more effective method for probing the magnetic susceptibility.

Static and dynamic properties of the FeCoB synthetic antiferromagnetic structures can be used to characterize the anisotropy of the system in a manner reminiscent of the ctitical curve. The critical curve can provide information about the anisotropy through magnetization reversal in each layer. The static switching curve which we obtained through reversible susceptibility measurements can be compared with magnetization dynamics in a synthetic in the sample investigated through microwave absorption spectroscopy. The correlation between static and

dynamic critical curves can be supported by performing macrospin simulations.

The study does not include the results for the static critical of the exchange bias samples. Upon completion of the research, the data can be used as a supplement to the dynamic results Daniel Adams is currently working on. The combination of the static and dynamic measurements can be used to formulate a theoretical explanation for the elusive exchange bias phenomenon.

The dependence of magnetic anisotropies of the exchange-biased NiFe/FeMn bilayers on the antiferromagnetic layer thickness via the measurement of the static and dynamic critical curves can be investigated. Measuring in-plane angular-dependent ferromagnetic resonance fields is another approach to obtain some important data about the sample that can be crucial in understanding the exchange bias in the samples.

The major hysteresis loop for the exchange bias samples revealed an intriguing phenomenon that uniaxial and unidirectional anisotropies coexist in the film plane, however, they are not collinear with each other. The angular difference between the exchange bias and the easy axis can be observed through the major hysteresis loop for the samples. Research can be carried out to formulate a method to calculate the non-collinearity using the hysteresis loops.

This research is mostly academic and helps to provide a better comprehension of the magnetic phenomenon emanating from the interface interaction of couple magnetic nanostructures. The samples studied, synthetic antiferromagnets and exchange bias samples, have technological impact too; thus are of additional interest. Knowing the critical curve of a coupled magnetic structure like synthetic antiferromagnetic structure is essential for devices such as magnetic random access memories.

A Appendix

A.1 Types of Magnetic Material

There are different classes of material that exhibit magnetic properties depending upon their atomic structure and domains. In this section we briefly outline some of those materials. The magnetic materials used for our research purpose are ferromagnetic and antiferromagnetic which are discussed in detail in the first chapter..

Diamagnetism

Diamagnetism is a magnetic property that is exhibited by every material. Substances that are negligibly magnetized in the opposite direction of the applied field are called diamagnetic material. An applied magnetic field creates an induced magnetic field in them in the opposite direction, causing a repulsive force. Diamagnetism is a quantum mechanical effect caused due to the non-cooperative behavior of orbiting electrons when exposed to an applied magnetic field. Diamagnetic substances are composed of atoms which have no net magnetic moments (ie., all the orbital shells are filled and there are no unpaired electrons). However, when exposed to a field, a negative magnetization is produced and thus the susceptibility is negative.

Diamagnetism was first discovered when Sebald Justinus Brugmans observed in 1778 that bismuth and antimony were repelled by magnetic fields. Water is an everyday example of diamagnetic material.

Paramagnetism

Paramagnetism is a form of magnetism whereby certain materials are weakly attracted by an externally applied magnetic field, and form internal, induced magnetic fields in the direction of the applied magnetic field. The magnetic moment

induced by the applied field is linear in the field strength and rather weak. It typically requires a sensitive analytical balance to detect the effect and modern measurements of paramagnetic materials. They have relatively small positive magnetic susceptibility.

Paramagnetism is due to the presence of unpaired electrons in the material, so all atoms with incompletely filled atomic orbitals are paramagnetic. Due to their spin, unpaired electrons have a magnetic dipole moment and act like tiny magnets. Paramagnets do not retain any magnetization in the absence of an externally applied magnetic field.

Ferromagnetism

A ferromagnet, like a paramagnetic substance, has unpaired electrons. However, in addition to the electrons' intrinsic magnetic moment's tendency to be parallel to an applied field, there is also in these materials a tendency for these magnetic moments to orient parallel to each other to maintain a lowered-energy state. Thus, even in the absence of an applied field, the magnetic moments of the electrons in the material spontaneously line up parallel to one another.

Ferromagnetism only occurs in a few substances; the common ones are iron, nickel, cobalt, their alloys, and some alloys of rare-earth metals.

Antiferromagnetism

In an antiferromagnet, unlike a ferromagnet, there is a tendency for the intrinsic magnetic moments of neighboring valence electrons to point in opposite directions. When all atoms are arranged in a substance so that each neighbor is anti-parallel, the substance is antiferromagnetic. Antiferromagnets have a zero net magnetic moment, meaning that no field is produced by them. Antiferromagnets are less common compared to the other types of behaviors and are mostly observed at low temperatures. In varying temperatures, antiferromagnets can be seen to exhibit

diamagnetic and ferromagnetic properties.

Ferrimagnetism

Like ferromagnetism, ferrimagnets retain their magnetization in the absence of a field. However, like antiferromagnets, neighboring pairs of electron spins tend to point in opposite directions. These two properties are not contradictory, because in the optimal geometrical arrangement, there is more magnetic moment from the sublattice of electrons that point in one direction, than from the sublattice that points in the opposite direction.

Superparamagnetism

Superparamagnetism is a form of magnetism which appears in small ferromagnetic or ferrimagnetic nanoparticles where magnetization can randomly flip direction under the influence of temperature. The typical time between two flips is called the Néel relaxation time. In this state, an external magnetic field is able to magnetize the nanoparticles, similarly to a paramagnet. However, their magnetic susceptibility is much larger than that of paramagnets.

A.2 Thin Films

The term thin films usually emanate a sinister scientific connotation that only condensed matter physicist can comprehend. The fact that mirrors, which we use in our daily lives, are also thin films should help diminish that stigma.

A thin film is a layer of material ranging from fractions of a nanometer (monolayer) to several micrometers in thickness. A stack of thin films is called a multilayer. The controlled synthesis of materials as thin films (a process referred to as deposition) is a fundamental step in many applications. A thin film of metal layer is deposited using techniques such as sputtering.

Advances in thin film deposition techniques during the 20th century have enabled a wide range of technological breakthroughs in areas such as magnetic recording media, electronic semiconductor devices, LEDs, optical coatings (such as anti-reflective coatings), hard coatings on cutting tools, and for both energy generation (e.g. thin-film solar cells) and storage (thin-film batteries). It is also being applied to pharmaceuticals, via thin-film drug delivery.

In addition to their applied interest, thin films play an important role in the development and study of materials with new and unique properties. Examples include multiferroic materials, and superlattices that allow the study of quantum confinement by creating two-dimensional electron states.

A.3 Timeline of Experiments Based on Tunnel Diode Oscillator

The potential of the tunnel diode of being able to operate at high frequencies encompassing even the microwave bands made it a suitable candidate as an oscillator and high-frequency (trigger) device. The tunnel diodes have been used for mundane devices like the oscillator for UHF television tuners. Tunnel diodes are mostly employed in research laboratories and technological environment as trigger circuits in oscilloscopes, high-speed counter circuits, and very fast-rise time pulse generator circuits. The tunnel diode can also be used as a low-noise microwave amplifier.

The first formal use of a tunnel diode oscillator (TDO) setup to perform an experiment was recorded in 1969, a decade after its invention, by R. Meservey *et al* [24]. Via the construction and use of a TDO operating at 15 MHz the study provides measurements of kinetic inductance of superconducting linear structures. Meservey and his team used the employed this technique to determine the carrier concentration from penetration depth in films and wires of superconducting

materials. The setup was assembled using two systems. The amplifier, frequency counter and power supply were used at room temperature while the TDO with the LC tank were kept at liquid He temperature. The coil in the LC tank in the oscillator contained the samples under investigation.

R. B. Clover and W. P. Wolf [25] administered a similar circuit a year later in 1970 to demonstrate the paramagnetic susceptibility measurements via the TDO method. The experiments were performed at frequencies from 3 to 55 MHz and at temperatures from 1.2 to 77 K.The magnetic fields were boosted up to 18 kG. They also proposed a semi-empirical formula to describe the frequency of TDO operation.

The following year, in 1971 Y. J. Kingma and V. Dvorak [26] published a new scientific paper regarding the tunneling diode oscillator. The paper proposed to use of the negative differential resistance of a tunnel diode oscillator as a proximity switch based on a study of two mutually coupled resonant circuits. The new study used circuits that had identifiable similarities with the old studies but in addition it had two critically coupled LC circuits. They found that, depending on the coupling strength of the two coils, the TDO can switch oscillation modes.

"A Tunnel Diode NMR Spectrometer" titled paper was published by J. Aslam and W. Weyhmann in 1973 [27]. The study used a tunnel diode oscillator which showed to be useful for NMR studies in ferromagnets at VHF and UHF frequencies. The oscillator could be tuned electronically over octave ranges and could be operated at low temperatures. The sensitivity proved to be comparable to standard cw oscillators, but much more compact and did not require long radio frequency (rf) lines.

Craig T. Van Degrift [28] recorded the construction and the results of a systematic study of the design considerations of a tunnel diode oscillator for 0.001 ppm measurements at low temperatures. Comprehensive calculations regarding the measured frequency, noise and dependence on bias voltage, magnetic field, and

temperature of the TDO circuit are considered to be a momentous contribution for the development of TDO studies. The paper also explored the possibility that the TDO method can be used to detect extremely small changes in a number of material properties such as thermal expansion, surface impedance, and electric and magnetic permeability.

J. G. Brisson and I. F. Silvera [29] published a paper in 1986 exploring the theory and applications behind a transmission-line tunnel diode oscillator (TLTDO) which combines the ease of construction of a discrete element TDO with the quick response times and immunity to stray reactances of the reentrant cavity TDO. Theory and design of four TLTDO's and two characteristic response times for TDO's are also throughly discussed in the paper.

R. Meservey and J.S. Moodera [30] published a new paper in 1986 combining his earlier work and Van Degrift's study. The work developing a low temperature magnetic susceptometer for thin films based on a TDO. The inductance is in this case a superconducting meander line. The device is capable to detect a change in susceptibility equal to that of a change in Fe thin film thickness of 0.03 atomic layers.

In 1993, G. J. Athas *et al.* [31] reported the first application of a tunnel diode circuit to investigate the de Haas–van Alphen effect and superconducting critical field values in small single crystal organic conductors. The study established a marked improvement over previous magnetic methods for the determination of both de Haas–val Alphen signals and for critical field studies. The method was proved to be applicable where such information is required for very small samples.

In 1999 a paper by H. Srikanth *et al.*[16] [32] characterized the use of a TDO for precise measurements of relative magneto-impedance changes in materials directly from the measured shift in TDO resonance frequency. Test measurements on a

[16]The authors worked for Advanced Materials Research Institute, University of New Orleans, New Orleans LA 70148

manganese-based perovskite sample exhibiting colossal magneto-resistance (CMR) indicated that this method is well suited to study the magneto-impedance in these materials.

T. Coffey et al. [33] presented the details of an apparatus that extended the tunnel diode techniques to measure the properties of materials in pulsed magnetic fields in their paper. in the year 2000. The sample is placed in the inductor of a small radio frequency (rf) tank circuit powered by a tunnel diode where the conductivity, magnetization, or penetration depth can be measured. The property measured immensely depends on the sample and configuration of the radio frequency field. A major innovation reported was the stabilization of the TDO during a magnet pulse by using compensated coils in the tank circuit.

In 2000 L. Spinu *et al.* [34] published a paper which analyzed and implemented the application of the resonant TDO technique to prove the field response of dynamic transverse susceptibility in magnetic nanoparticle systems. This procedure helped to attain precise mapping of fundamental parameters like the anisotropy and switching fields which is essential to understand the influence of the relaxation, interactions and other phenomena that govern the dynamic magnetic properties in magnetic nanostructures. The tunnel diode oscillator has proved to be a great tool in probing the transverse magnetic susceptibility of novel materials and structures such as magnetic nanostructures [35, 36], nanoparticle systems [34, 36, 37] and arrays [37, 38], magnetic multilayered structures [9, 18], and synthetic antiferromagnets [39, 40].

Over the past two decades L. Spinu and his research team have provided exhilarating results in the world of magnetic nanostructures using the tunnel diode oscillator. Daniel J Adams *et al.* [10, 11, 12] published papers in 2017 and 2018 exploring the angular dependence of resonant absorption in FeCoB synthetic antiferromagnets and critical switching curves of FeCoB synthetic antiferromagnets. The TDO was used to provide the static critical curve in both studies. Simi-

lar studies were done to probe the temperature dependence of exchange bias in $(\mathrm{NiFe/IrMn})_n$ multilayer films studied through static and dynamic techniques.

A.4 Magnetic Field between Helmholtz coils

In physics, specifically electromagnetism, the Biot–Savart law is an equation describing the magnetic field generated by a stationary electric current. The Biot-Savart Law states the magnetic field B from a wire length **dl**, carrying a steady current I is given by:

$$\mathbf{B(r)} = \frac{\mu_0}{4\pi} I \int \frac{\mathbf{dl} \times \mathbf{r}}{|r|^3} \tag{A.1}$$

where μ_0 is the permeability of free space and **r** is the displacement vector from the current element **dl** to a point P where the magnetic field is to be evaluated. This equation can be used calculate the magnetic fields for arbitrary current distributions such as circular or rectangular loops.

The magnitude of the magnetic field B along an axis through the center of a circular loop, like that of a Helmholtz coil, carrying steady current I can be expressed as:

$$B(x) = \frac{\mu_0 I R^2}{2(R^2 + x^2)^{3/2}}$$

The Helmholtz coils consists of N turns of wire, so the equivalent current in a one-turn coil is N times the current I in the N-turn coil. Substituting NI for I in the above formula gives the field for an N-turn coil:

$$B(x) = \frac{\mu_0 N I R^2}{2(R^2 + x^2)^{3/2}} \tag{A.2}$$

where R is the radius of the loop and x is the coil distance, on axis, to a point. In a Helmholtz coil, a point halfway between the two loops has an x value equal to

R/2, so calculate the field strength at that point:

$$B\left(\frac{R}{2}\right) = \frac{\mu_0 N I R^2}{2(R^2 + (R/2)^2)^{3/2}}$$

There are also two coils in a system of Helmholtz coils instead of one. The coil above is at $x = 0$ while the second coil is positioned at $x = R$. From symmetry, the field strength at the midpoint will be twice the single coil value.

$$B = \left(\frac{8}{5\sqrt{5}}\right)\frac{\mu_0 N I}{R} \tag{A.3}$$

References

1. Khanal, Shankar, "Study of Static and Dynamic Properties of Magnetic Nanostructures" (2017). University of New Orleans Theses and Dissertations. 2382.

2. Radu, Cosmin, "Study of Magnetization Switching in Coupled Magnetic Nanostructured Systems" (2008). University of New Orleans Theses and Dissertations. 894.

3. Diaconu, Andrei, "Ultra-low Temperature Measurements of London Penetration Depth in Iron Selenide Telluride Superconductors" (2013). University of New Orleans Theses and Dissertations. 1731.

4. B. Hillebrands and K. Ounadjela, Spin dynamics in confined magnetic structures I.Berlin ; New York: Springer, 2002.

5. B. Hillebrands and K. Ounadjela, Spin dynamics in confined magnetic structures II.Berlin ; New York: Springer, 2003.

6. J. C. Slonczewski, IBM Research Center Poughkeepsie Research Memorandum R.M. 003.111.224, 1956.

7. A. Thiaville, "Extensions of the geometric solution of the two dimensional coherent magnetization rotation model," Journal Of Magnetism And Magnetic Materials, vol. 82, pp. 5-18, Feb 1998.

8. E. C. Stoner and E. P. Wohlfarth, "A mechanism of magnetic hysteresis in heterogeneous alloys," Philosophical Transactions of the Royal Society of London, ol. A240, pp. 599-644, 1948.

9. L. Spinu, A. Stancu, Y. Kubota, G. Ju, and D. Weller, "Vectorial mapping of exchange anisotropy in IrMn/FeCo multilayers using the reversible susceptibility tensor," Physical Review B, vol. 68, p. 220401, 2003.

10. Adams, Daniel J., et al. "Angular Dependence of Resonant Absorption in FeCoB Synthetic Antiferromagnets." AIP Advances, vol. 7, no. 5, 2017, p. 056322

11. Adams, et al. "Critical Switching Curves of FeCoB Synthetic Antiferromagnets." Journal of Physics D Applied Physics, 1 Feb. 2018,

12. Adams, Daniel J., et al. "Temperature Dependence of Exchange Bias in (NiFe/IrMn)n Multilayer Films Studied through Static and Dynamic Techniques." AIP Advances, vol. 8, no. 5, 2018, p. 056302.

13. Cullity, B.D., Introduction to Magnetic Materials 1972, New Jersey: Addison-Wiley Publishing Company.

14. Tannous, C, and J Gieraltowski. "The Stonerâ-Wohlfarth Model of Ferromagnetism." European Journal of Physics, vol. 29, no. 3, 2008, pp. 475–487

15. Gans, R., Zur Theorie des Ferromagnetismus: Die reversible longitudinale und transversale Permeabilitat. Ann Phys, 1909. 29: p. 301-315.

16. Aharoni, A.F., E. H.; Shtrikman, S.; Treves, D., The Reversible Susceptibility Tensor of the Stoner- Wohlfarth Model Bulletin of the Research Council of Israel, 1957. 6A: p. 215-238.

17. Spinu, L., et al., Transverse susceptibility as the low-frequency limit of ferromagnetic resonance. Journal of Magnetism and Magnetic Materials, 2006. 296(1): p. 1-8.

18. L. Spinu, H. Pham, C. Radu, J. Denardin, I. Dumitru, M. Knobel, L. Dorneles, L. Schelp, and A. Stancu, "Probing two-dimensional magnetic switching

in Co/ SiO multilayers using reversible susceptibility experiments," Applied Physics Letters, vol. 86, p. 012506, 2005.

19. Smith, D. O. (1956). "Development of a Vibrating-Coil Magnetometer". Rev. Sci. Instrum. 27 (261): 261.

20. Foner, Simon (1959). "Versatile and Sensitive Vibrating-Sample Magnetometer". Rev. Sci. Instrum. 30 (7): 548–557.

21. Diode type semiconductor device United States patent 3,033,714

22. L. Esaki, "New Phenomenon in Narrow Germanium p-n Junctions," Physical Review, vol. 109, pp. 603-604, 01/15/ 1958.

23. Esaki, Leo; Arakawa, Yasuhiko; Kitamura, Masatoshi (2010). "Esaki diode is still a radio star, half a century on". Nature. 464 (7285): 31.

24. R. Meservey and P. Tedrow, "Measurements of the kinetic inductance of superconducting linear structures," Journal of Applied Physics, vol. 40, pp. 2028-2034, 1969.

25. R. Clover and W. Wolf, "Magnetic susceptibility measurements with a tunnel diode oscillator," Review of Scientific Instruments, vol. 41, pp. 617-621, 1970.

26. Y. Kingma and V. Dvorak, "A negative resistance oscillator with two modes†," International Journal of Electronics Theoretical and Experimental, vol. 30, pp. 1-17, 1971.

27. J. Aslam and W. Weyhmann, "A tunnel diode NMR spectrometer," Review of Scientific Instruments, vol. 44, p. 71, 1973.

28. C. T. Van Degrift, "Tunnel diode oscillator for 0.001 ppm measurements at low temperatures," Review of Scientific Instruments, vol. 46, pp. 599-607,

1975. 32

29. J. G. Brisson and I. F. Silvera, "Transmission-line tunnel diode oscillator: A sensitive, fast, and flexible low-temperature detection system," Review of scientific instruments, vol. 57, pp. 2842- 2847, 1986

30. R. Meservey and J. S. Moodera, "Performance of a magnetic susceptometer for thin films and surfaces," Journal of Applied Physics, vol. 60, pp. 3007-3014, 1986.

31. G. Athas, J. Brooks, S. Klepper, S. Uji, and M. Tokumoto, "Tunnel diode oscillator application to high sensitivity de Haas–van Alphen and superconducting critical field studies of anisotropic organic conductors," Review of scientific instruments, vol. 64, pp. 3248-3251, 1993.

32. H. Srikanth, J. Wiggins, and H. Rees, "Radio-frequency impedance measurements using a tunneldiode oscillator technique," Review of scientific instruments, vol. 70, pp. 3097-3101, 1999.

33. T. Coffey, Z. Bayindir, J. DeCarolis, M. Bennett, G. Esper, and C. Agosta, "Measuring radio frequency properties of materials in pulsed magnetic fields with a tunnel diode oscillator," Review of Scientific Instruments, vol. 71, pp. 4600-4606, 2000.

34. L. Spinu, H. Srikanth, E. Carpenter, and C. OConnor, "Dynamic radio-frequency transverse 34susceptibility in magnetic nanoparticle systems," Journal of Applied Physics, vol. 87, pp. 5490- 5492, 2000.

35. L. Spinu, C. O'Connor, and H. Srikanth, "Radio frequency probe studies of magnetic nanostructures," Magnetics, IEEE Transactions on, vol. 37, pp. 2188-2193, 2001.

36. P. Poddar, Y. Sahoo, H. Srikanth, and P. Prasad, "Ferromagnetic ordering in nanostructured Mndoped InP," Applied Physics Letters, vol. 87, pp. 062506-062506-3, 2005.

37. L. Spinu, H. Srikanth, J. Wiemann, S. Li, J. Tang, and C. O'Connor, "Superparamagnetism and transverse susceptibility in magnetic nanoparticle systems," Magnetics, IEEE Transactions on, vol. 36, pp. 3032-3034, 2000.

38. P. Poddar, J. Wilson, H. Srikanth, D. Farrell, and S. Majetich, "In-plane and out-of-plane transverse susceptibility in close-packed arrays of monodisperse Fe nanoparticles," Physical Review B, vol. 68, p. 214409, 2003.

39. C. Radu, D. Cimpoesu, E. Girt, G. Ju, A. Stancu, and L. Spinu, "Reversible susceptibility studies of magnetization switching in FeCoB synthetic antiferromagnets," Journal of applied physics, vol. 101, pp. 09D109-09D109-3, 2007.

40. H. Van den Berg, J. Altmann, L. Bar, G. Gieres, R. Kinder, R. Rupp, M. Vieth, and J. Wecker, "Magnetic tunnel sensors with Co-Cu artificial antiferromagnetic (AAF) hard subsystem," Magnetics, IEEE Transactions on, vol. 35, pp. 2892-2894, 1999

41. Aeroflex-Metelics, "MBD Series Planar Back Tunnel Diodes A17077 " 2005.

42. S. Hernandez, M. Kapoor, and R. H. Victora, "Synthetic antiferromagnet for hard layer of exchange coupled composite media," Applied Physics Letters, vol. 90, p. 132505, Mar 26 2007.

43. S. C. Byeon, A. Misra, and W. D. Doyle, "Synthetic antiferromagnetic soft underlayers for perpendicular recording media," IEEE Transactions on Magnetics, vol. 40, pp. 2386-2388, Jul 2004.

44. L. Savtchenko, B. N. Engel, N. D. Rizzo, M. F. Deherrera, and J. A. Janesky, "Method of writing to scalable magnetoresistance random access memory element " US Patent 6,545,906 B1: Motorola, Inc. (Schaumburg, IL) 2003.

45. A. Veloso and P. P. Freitas, "Spin valve sensors with synthetic free and pinned layers," Journal of Applied Physics, vol. 87, pp. 5744-5746, May 2000.

46. M. Forrester and F. Kusmartsev, The nano-mechanics and magnetic properties of high moment synthetic antiferromagnetic particles, physica status solidi a 211, 884–889 (2014)

47. M. A. Ruderman and C. Kittel, "Indirect Exchange Coupling of Nuclear Magnetic Moments by Conduction Electrons," Physical Review, vol. 96, p. 99, 1954.

48. Adams, Daniel J., "Ferromagnetic Resonance Studies of Coupled Magnetic Systems" (2016). University of New Orleans Theses and Dissertations. 2121.

49. Meiklejohn, W. H.; Bean, C. P. (1957-02-03). "New Magnetic Anisotropy". Physical Review. 105 (3): 904–913

50. M. Kiwi, "Exchange bias theory," Journal of Magnetism and Magnetic Materials, vol. 234, pp. 584-595, 2001.

51. J. Nogués and I. K. Schuller, "Exchange bias," Journal of Magnetism and Magnetic Materials, vol. 192, pp. 203-232, 1999.

52. S. Parkin, K. Roche, M. Samant, P. Rice, R. Beyers, R. Scheuerlein, et al., "Exchange-biased magnetic tunnel junctions and application to nonvolatile magnetic random access memory," Journal of Applied Physics, vol. 85, pp. 5828-5833, 1999.

53. Hyeok-Cheol Choi, Chun-Yeol You, Ki-Yeon Kim, Jeong-Soo Lee, Je-Ho Shim, and Dong-Hyun Kim "Antiferromagnetic layer thickness dependence of noncollinear uniaxial and unidirectional anisotropies in NiFe/FeMn/CoFe trilayers", Phys. Rev. B 81, 224410 (2010).

54. Néel, Louis (1948). "Magnetic Properties of Ferrites: Ferrimagnetism and Antiferromagnetism". Ann. Phys. (Paris). 3: 137–198.

55. L. Néel, Ann. phys (Paris) 17, 64 (1932)

56. P. Weiss (1906) La variation du ferromagnetisme du temperature, Comptes Rendus, 143, p.1136-1149, cited in Cullity, 2008, p.116

57. Nogués, J., C. Leighton, and Ivan K. Schuller. "Correlation between Antiferromagnetic Interface Coupling and Positive Exchange Bias." Physical Review B. American Physical Society, 01 Jan. 2000.

58. Ohldag, Hendrik, Hongtao Shi, Elke Arenholz, Joachim StÃ¶hr, and David Lederman. "Parallel versus Antiparallel Interfacial Coupling in Exchange Biased Co/FeF2." Physical Review Letters 96.2 (2006)

List of Publications

1. Adams, Daniel J., Dorin Cimpoesu, **Mohammad Asif Khan**, Pratik Poudyal, and Leonard Spinu. "Critical Switching Curves of FeCoB Synthetic Antiferromagnets." Journal of Physics D: Applied Physics, 12 Jan. 2018.

2. Adams, Daniel J., Shankar Khanal, **Mohammad Asif Khan**, Artur Maksymov, and Leonard Spinu. "Temperature Dependence of Exchange Bias in (NiFe/IrMn)n Multilayer Films Studied through Static and Dynamic Techniques." AIP Publishing. AIP Publishing LLC, 4 December 2017.

3. Adams, Daniel J., **Mohammad Asif Khan**, Pratik Poudyal, and Leonard Spinu. "Angular Dependence of Resonant Absorption in FeCoB Synthetic Antiferromagnets." AIP Publishing. AIP Publishing LLC, 1 Mar. 2017.

IOP Publishing Journal of Physics D: Applied Physics

J. Phys. D: Appl. Phys. **51** (2018) 055005 (8pp) https://doi.org/10.1088/1361-6463/aaa271

Critical switching curves of FeCoB synthetic antiferromagnets

Daniel J Adams[1], Dorin Cimpoesu[2], Mohammad Asif Khan[1], Pratik Poudyal[1] and Leonard Spinu[1]

[1] Department of Physics and Advanced Materials Research Institute, University of New Orleans, New Orleans, LA 70148, United States of America
[2] Faculty of Physics, Department of Physics, 'Alexandru Ioan Cuza' University, Iasi 700506, Romania

E-mail: LSpinu@uno.edu

Received 17 October 2017, revised 5 December 2017
Accepted for publication 18 December 2017
Published 12 January 2018

Abstract

Magnetization dynamics in a synthetic antiferromagnet with magnetic layers of FeCoB were investigated through microwave absorption spectroscopy. Resonant absorption signal detected along different directions in the plane of the films was analyzed through a graphical representation reminiscent of the critical switching curves. The advantage of this representation is that anisotropy and coupling effects can be determined by inspection. Further, this data can then be readily compared to the static switching curve which we obtained through reversible susceptibility measurements. The correlation between static and dynamic critical curves is supported by macrospin simulations.

Keywords: magnetization dynamics, ferromagnetic resonance, critical curve, magnetization switching

(Some figures may appear in colour only in the online journal)

1. Introduction

Layered structures coupled through Ruderman–Kittel–Kasuya–Yosida (RKKY) interactions such as synthetic antiferromagnets (SAF) have been particularly interesting due to controllable coupling strength. The interlayer exchange coupling in these structures plays an important role in their application in devices such as recording media [1, 2] and magnetoresistive random access memories (MRAM) components [3–11], as the operation of these devices relies on the individual magnetization reversal of the ferromagnetic layers. Recently, it has been shown that SAF nanoparticles show potential for use as contrast agents in magnetic resonance imaging [12]. It is also been suggested that SAF structures may help to understand spin–orbit torque switching [13]. In order to determine the anisotropy, coupling effects, and magnetization reversal, it is important to study magnetization properties of these systems in the plane of the device with an applied magnetic field along different orientations with respect to the easy axis.

The critical curve (CC) is the locus of points for which the irreversible magnetization reversal occurs [14], and several methods have been developed to determine the CC [15–20]. One of the most sensitive techniques for probing the switching fields is transverse susceptibility [21]. It is known that the CC for coupled magnetic systems is more complex than the switching curve of typical uncoupled ferromagnetic samples [15]. The CC in the case of SAF contains two curves, where the region outside of the outermost curve corresponds to the fields for which the magnetizations of the two layers are parallel to one another while the innermost curve is the CC for switching [22].

In the static regime, SAF switching properties have been investigated by the method mentioned above. More recently, these properties have been studied by manipulating layer thicknesses to alter the layer switching order as a function of field sweep rate and direction [23]. Further, the microwave properties of SAF have been well investigated through ferromagnetic resonance (FMR) spectroscopy to characterize a number of features including linewidth, absorption position, coupling strength, intensity, angle- and temperature-dependence of resonant absorption, and manipulation of resonant modes [24–31]. Devices utilizing SAF as a component have also

been investigated through FMR to study the different anisotropies among device layers [32]. A dynamic generalization of static CC for SAF structures was theoretically proposed in [33] for SAF elements subjected to pulsed magnetic fields, showing the possibility of the reduction of the switching field amplitude by varying the pulse shape and length.

In this work, we seek to probe the anisotropy of our system through angular-dependent FMR in a manner analogous to the CC. We report experimental studies and macrospin simulations of both the in-plane magnetization reversal and the angular-dependent FMR absorption in a SAF structure, similar to a study previously reported for 2D array of magnetic nanowires [34]. The analysis of the static magnetization reversal is presented graphically in the form of the static CC following the initial concept developed under the Stoner–Wohlfarth (SW) model [35] for systems with uniaxial anisotropy [36]. The FMR absorption at several frequencies is also graphically presented through a CC-like approach in what we call a dynamic critical curve (dCC). The advantage of this representation over typical broadband or continuous-wave (CW) frequency absorption is that information about the anisotropy and angular-dependence of interactions is available upon inspection.

Previously, we have reported the experimental dCC of Ru coupled FeCoB layers selected from a series of samples [37]. However, here we wish to advance our focus only using a sample in which the magnetic layers are coupled antiferromagnetically and to provide a theoretical validation of the observed experimental data. The experimental design of our previous study limited us to FMR characterization for frequencies greater than or equal to 2.5 GHz, and it was not clear if FMR at lower frequencies was achievable for this structure. Another constraint of our previous work is that the hard axis characterization was lost, since in this region the dc magnetic field and the microwave magnetic field were parallel, and therefore the dCC's presented were somewhat incomplete. In this study, both of these limitations are overcome in ways detailed in following sections. Our results here are supported by simulations under a macrospin model.

2. Experiment

The sample under study was a trilayer stack of thin films composed of two ferromagnetic layers of FeCoB coupled antiferromagnetically across a Ru spacer of 1.6 nm, deposited on glass at room temperature through dc magnetron sputtering with a small magnetic field applied in the plane of the sample to induce an anisotropy axis. The dimensions were 5 mm × 5 mm, with a total sample thickness of approximately 30 nm. Major hysteresis loops (MHL) were measured using a vibrating sample magnetometer along different directions in the plane of the sample. The anisotropy is evident in the MHL in figure 1.

The static CC was obtained by measuring the susceptibility for different dc fields applied in the plane of the thin films using the tunnel diode oscillator (TDO) method similar to that proposed in [20]. The sample was placed in a sensing coil with both the ac and dc magnetic fields in the plane of the sample.

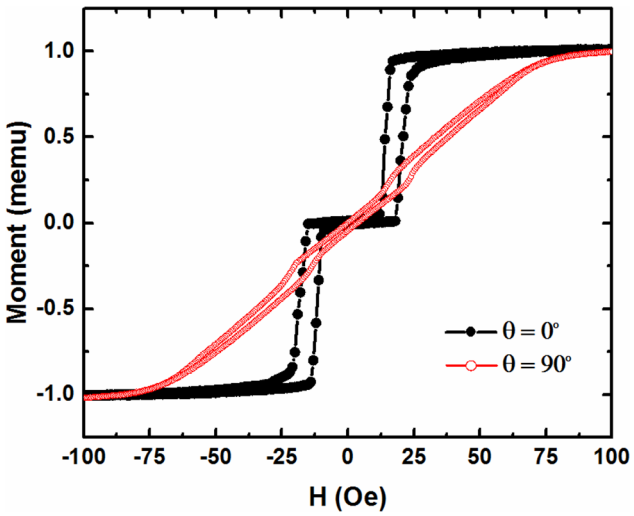

Figure 1. MHL along the easy (black) and hard (red) axes.

A dc magnetic field ($\mathbf{H_{dc}}$) was created by a double Helmholtz coil capable of creating a uniform magnetic field in any direction within the plane of the sample. The susceptibility signal was recorded as a function of applied magnetic field. $\mathbf{H_{dc}}$ was applied at different orientations in the plane of the sample in the range from 0° to 180° with respect to the easy axis in 2° increments, while the sensing coil remained fixed in place. For each angle, $\mathbf{H_{dc}}$ was ramped down from positive saturation to negative saturation, and then from negative saturation to positive saturation, while the susceptibility signal was recorded at every field step for a 360° characterization. From the change in susceptibility measured as a function of applied field, the static CC seen in figure 2 can be constructed.

When a microwave field is present, the static CC is no longer valid and must be replaced by a representation which takes into account the dynamic effects. In order to accomplish this, we probe the magnetization dynamics through vector network analyzer (VNA) FMR using a coplanar waveguide (CPW). It has been shown that VNA-FMR using a CPW is in good agreement with theoretical investigations as well as with conventional FMR techniques, and in general gives a high signal-to-noise ratio [38], and this technique has become a common practice [39–41].

The sample was placed on a commercial-grade CPW connected to a microwave VNA such that the magnetic field component of the microwave ($\mathbf{h_{ac}}$) was directed along the hard axis of the sample. $\mathbf{H_{dc}}$ was applied by a projected field electromagnet to produce a uniform magnetic field in the plane of the sample. The magnet was mounted on a rotation stage capable of 360° rotation. FMR absorption was measured by probing the S_{21} transmission coefficient as a function of applied field for a desired CW frequency. In analogy to the measurement of the CC, $\mathbf{H_{dc}}$ was applied at a number of angles in the plane of the sample with respect to the easy axis for a 360° characterization. $\mathbf{H_{dc}}$ was swept from positive saturation to negative in steps of approximately 1.5 Oe. At each angle, the measurement of the S_{21} parameter was performed at every field step. This geometry of the ac and dc fields relative to each other and to the anisotropy axis can be seen in figure 3(a). The sample was then turned 90° on the CPW such that the microwave

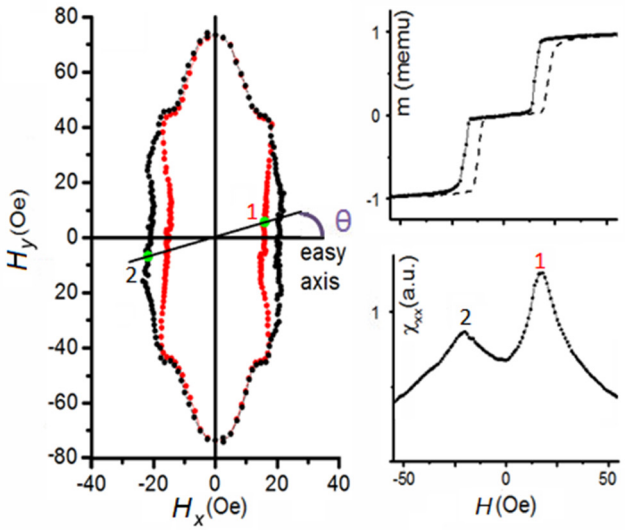

Figure 2. Experimental static CC determined from TDO susceptibility's curves (bottom right), as the in-plane dc field is applied at different orientations θ, and the experimental hysteresis loop (top right) for the indicated orientation.

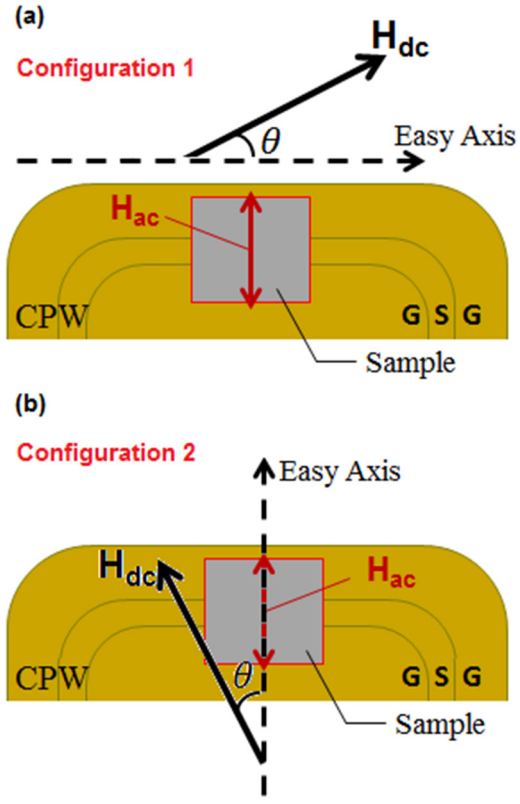

Figure 3. Schematic representation of sample on CPW and orientation of magnetic fields for (a) configuration 1 and (b) configuration 2 of FMR experiments.

magnetic field was along the easy axis (figure 3(b)) and the full angular FMR measurements repeated.

3. Results

As seen in the MHLs in figure 1, strong antiferromagnetic coupling between the FeCoB layers is observed in this sample.

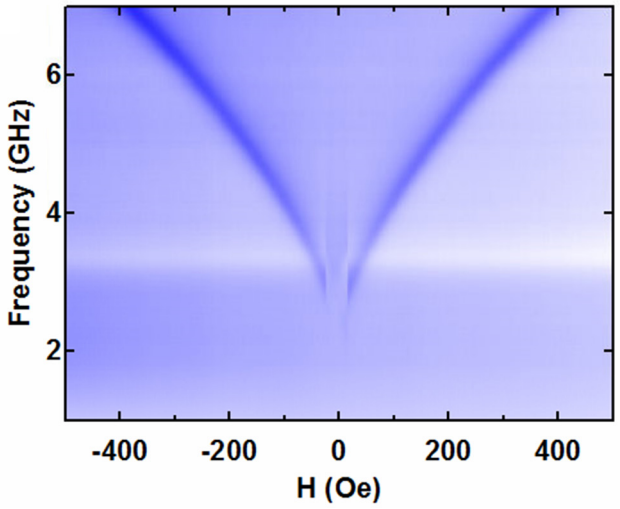

Figure 4. Broadband FMR signature for dc field applied along the sample's easy axis.

Due to the non-synchronous layer switching, the CC (figure 2) contains both the inner and outer curves we expect. This is different from the case of an uncoupled magnetic system where a static CC with a single branch is expected and experimentally observed [21]. As shown in figure 2 the inner and outer branches of the SAF's CC are obtained from different peaks of the susceptibility signal which correspond to the switching of the two ferromagnetic layers. Thus, as the field is ramped down from positive saturation to negative saturation the first observed peak (peak '1') in the susceptibility signal will correspond to the inner portion of the CC, while the second peak will determine the outer branch of the CC. The corresponding MHL branch is shown with continuous line in the right top panel of figure 2 while the upward MHL branch from negative to positive saturation is shown with dotted line. It should be noted that in the previous report of the experimental CC for a SAF [20] there was not a clear separation between the two branches, inner and outer, due to a smaller coupling between the layers in the SAF sample from that study. This will be further discussed in the next section where the simulated CC are presented.

An overview of the FMR absorption across the frequency range for the dc field applied along the easy axis is shown in figure 4. The easy axis broadband FMR spectrum in figure 4 is obtained using Configuration 1 (figure 3(a)) while the magnetic field is ramped down from positive saturation to negative saturation. In the lower field/lower frequency range, a splitting of the FMR absorption curve is observed, corresponding to the switching fields observed in the easy axis MHL in figure 1. In order to dynamically probe the anisotropy effects, a similar absorption curve can be obtained for different orientations of the dc field, as presented in the previous section. The FMR absorption data obtained by angular-dependent CW-FMR spectroscopy can be conveniently analyzed for each frequency using the polar contour representation of figure 5, i.e. dCC. As seen in the absorption curves, the coupling effects are particularly evident between 3 and 3.5 GHz where double resonances occur, which can be expected based on the broadband

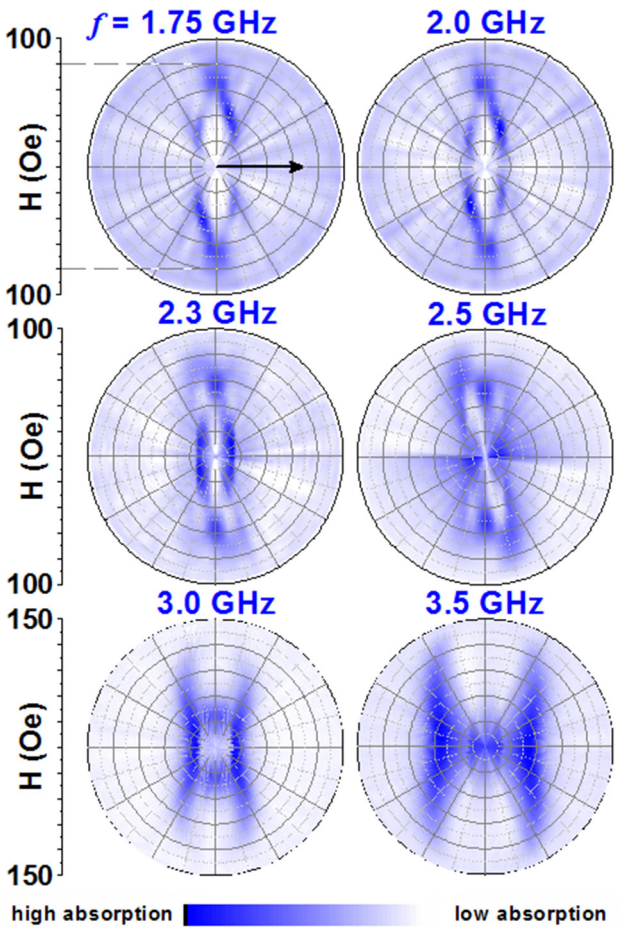

Figure 5. Polar contour representation of experimental FMR absorption spectra. The black arrow along the 0° direction indicates the easy axis.

curve in figure 4. The observed double resonance is associated with the successive switching of SAF's ferromagnetic layers, as the magnetic field is decreased from positive saturation to negative saturation. At lower frequencies, the dCC takes on a shape much more similar to the static CC. The two different types of CCs, static and dynamic, are compared directly in figure 6. One particularly interesting feature occurs at 2.3 GHz and lower frequencies, when the dCC is observed to go inside of the CC. This corresponds to the area of the MHL unique to SAF—the state in which the magnetization in one ferromagnetic layer has switched directions, creating a 'split' in the MHL as well as the broadband FMR curve. Another interesting observation in the low frequency dCC's is that they are closed at the 90° orientation, i.e. when $\mathbf{H_{dc}}$ is parallel to $\mathbf{h_{ac}}$. Normally, one would not expect to see clear FMR in this orientation. The reason this occurs is that when $\mathbf{H_{dc}}$ is applied at 90°, the magnetic moment $\mathbf{m}$ is aligned with it only for fields outside of the CC. Inside of the CC there is a non-zero angle between $\mathbf{H_{dc}}$ and $\mathbf{m}$ and between $\mathbf{h_{ac}}$ and $\mathbf{m}$. Consequently, the ac field is able to determine an oscillation of the magnetic moments' orientation.

The advantage of the polar curve is that it eliminates the need for a frequency versus applied field curve at a number of angles. The curves shown in figure 5, particularly at higher frequencies, are limited in that information about the anisotropy is lost as the dc magnetic field becomes parallel to the ac magnetic field and the magnetic moments are oriented almost along them. In the geometry of Configuration 1 (figure 3(a)), we lost the characterization along the hard axis. To correct this, a second polar curve must be constructed through measurements done in Configuration 2 (figure 3(b)) for a given frequency. This second curve will be lacking an easy axis characterization. Superimposing these curves gives a polar contour graph which contains complete information about the sample's anisotropy at higher frequencies. Examples of this superposition for selected frequencies can be seen in figure 7.

A previous difficulty in obtaining usable FMR spectra at low frequencies was due to the masking of the signal by noise. To overcome this, the signal to noise ratio was improved by using vibration isolation of the experimental setup. Further, post-measurement signal processing techniques using the Fast Fourier Transform and low-pass filter helped to smooth out the noise and make the FMR signal stand out.

The static switching as well as FMR absorption spectra were further analyzed by comparing the experimental data with simulation results. These were obtained using a macrospin approximation based on a generalized SW type model [42] which is able to describe the switching field in non-single-domain magnetic particles.

4. Theory

4.1. Static CC

In order to describe the SAF system in the simplest way, our model assumes that the magnetization in each layer can be described as a pseudo-single ferromagnetic particle. The effective fields for the two layers consist of the applied fields, anisotropy field, a phenomenological demagnetizing field perpendicular to the plane, and the antiferromagnetic coupling between the two layers. In order to overcome the limitations of the classical SW model [36] that, for a single-domain ferromagnetic particle with uniaxial anisotropy, predicts the same saturation field along and perpendicular to the easy axis in contradiction with the experiment, we have used the generalized SW model [42]. This generalized model offers a way to describe the angular dependency of the switching field in non-single-domain particles, essentially by including the effects of inhomogeneities (as nonuniform or vortex magnetization configurations) on the magnetization processes only in the anisotropy energy and maintaining the macrospin hypothesis. The nonuniform magnetic states are generally characterized by relatively complicated spin configurations which cannot be described by explicit solutions/functions, except in some particular cases. Therefore, the generalized SW model uses a phenomenological expression for the anisotropy energy with the aim to describe various experimentally observed dependencies of the switching field as a function of the field's orientation, and in the same time preserving as much as possible the elegance of the SW model and its numerical tractability, and the concept of CC [14, 35]. Essentially, the generalized SW model uses the parameter ξ to describe the ratio between the saturation fields perpendicular and along the easy axis, and

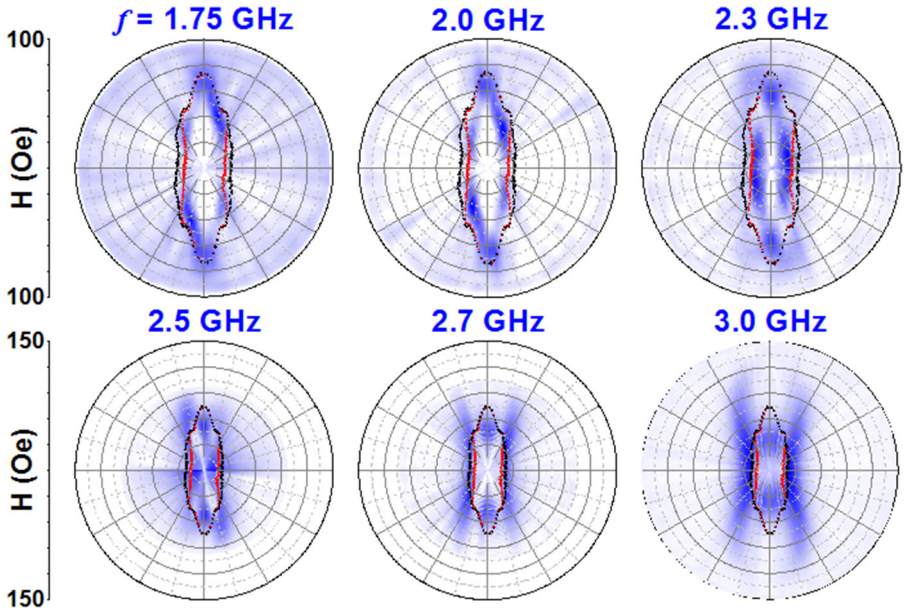

Figure 6. Static CC compared to dCC for selected frequencies.

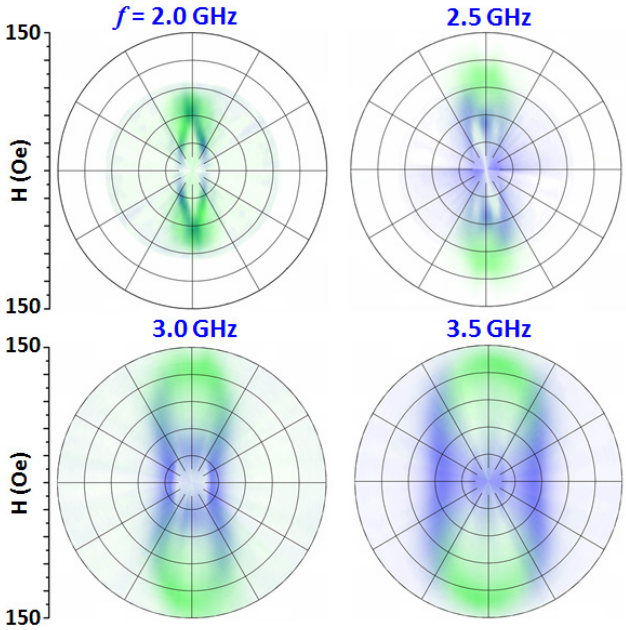

Figure 7. Superposition of dCC obtained for selected frequencies in configuration 1 (blue) and 2 (green), i.e. with ac magnetic field perpendicular to and parallel to the easy axis, respectively.

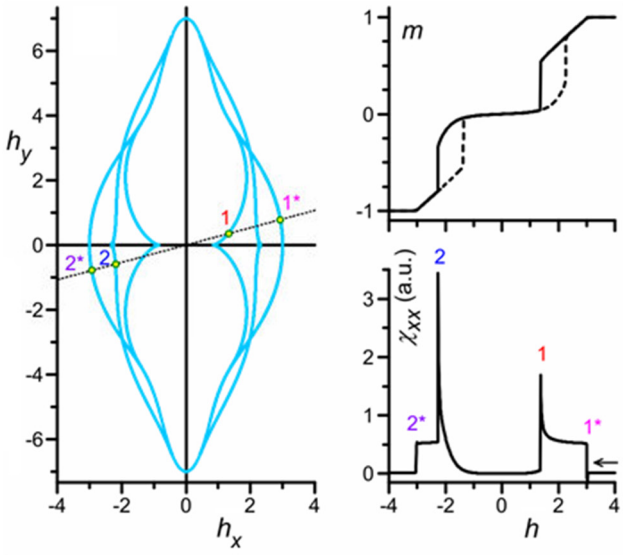

Figure 8. Simulated static CC determined from simulated susceptibility's curves (bottom right), as the in-plane dc field is applied at different orientations θ, and the simulated hysteresis loop (top right) for the indicated orientation. Simulation parameters are $h_J = 2$, $\xi = 3$, and $r = 2/3$.

the parameter r to describe the curvature of the static CC, the classical astroid for a single-domain magnetic particle being obtained as the particular case $\xi = 1$ and $r = 1$.

The static CC for a system of two coupled pseudo-single ferromagnetic particles/layers was obtained through the solutions of the system: $\partial F/\partial\theta_1 = \partial F/\partial\theta_2 = 0$ and $\left(\partial^2 F/\partial\theta_1^2\right)\left(\partial^2 F/\partial\theta_2^2\right) - \left(\partial^2 F/\partial\theta_1\partial\theta_2\right)^2 = 0$ [15, 43] where F is the free energy of the system, while θ_1,θ_2 describe the in-plane magnetization orientation of the two ferromagnetic layers with respect to the easy axis. In figure 8 we present the simulated CC for $h_J = 2$, $\xi = 3$, and $r = 2/3$, where h_J describes the antiferromagnetic coupling strength between the two layers [22]. The magnetic fields are normalized by the anisotropy field $H_k = 2K/M_s$, while the magnetization is normalized by the saturation magnetization M_s. As the $\xi > 1$ the SAF's static CC evolves into a more intricate curve (see CC from figure 8 compared with CC from figure 3 of [15]). In figure 8 we also present the hysteresis loop and the corresponding susceptibility curve for the orientation $\theta = 15^\circ$ of the applied magnetic field. We observe that as the applied magnetic field is swept from positive to negative saturation, the susceptibility curve has two peaks corresponding to discontinuous changes in the hysteresis curve, and two shoulders corresponding to the negative saturation field at which the two moments become parallel and to the positive saturation field

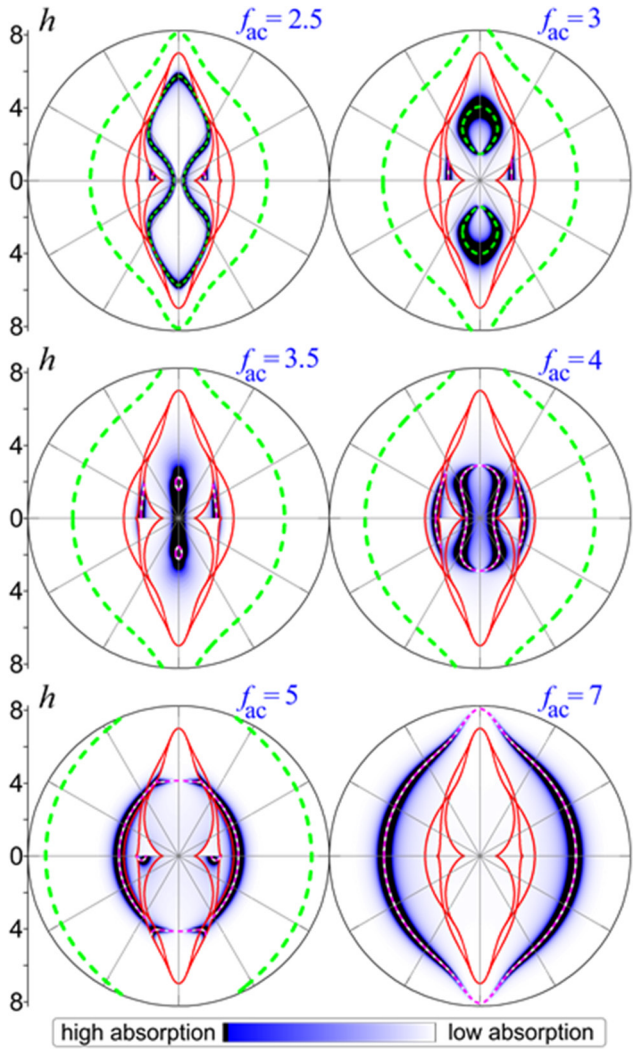

Figure 9. Simulated imaginary susceptibility χ'' computed on the descending branch of MHL for $h_J = 2$, $\xi = 3$, $r = 2/3$, for a damping constant $\alpha = 0.01$, for $h_{ac,max} = 10^{-3}$, and for different values of the ac frequency f_{ac}. The magnetic fields are measured in units of anisotropy field H_k and the ac field frequency in units of Kittel frequency $\gamma_0 H_k/2\pi$, where $\gamma_0/2\pi = 2.8$ MHz Oe^{-1}. The continuous lines represent the static CCs. The dashed lines (extracted as contour lines from figure 10) represent the locus of in-plane dc fields at which the natural frequencies of the system are equal to f_{ac}. For $f_{ac} = 2.5$ and 3 the absorption mainly takes place when f_{ac} matches the second natural frequency, while for the other frequencies the absorption mainly takes place when f_{ac} matches the first natural frequency.

at which the parallel state loses stability. The two shoulders correspond to the outermost part of the static CC (see points 1* and 2* in figure 8). Because such shoulders are difficult to be clearly identified in an experimental curve, only the peaks in the experimental susceptibility versus field plots were used to construct the experimental static CC.

4.2. Dynamic CC dCC

When an additional microwave field is applied the static CC description is no longer adequate. In this case the time evolution of magnetization is found by integrating the coupled

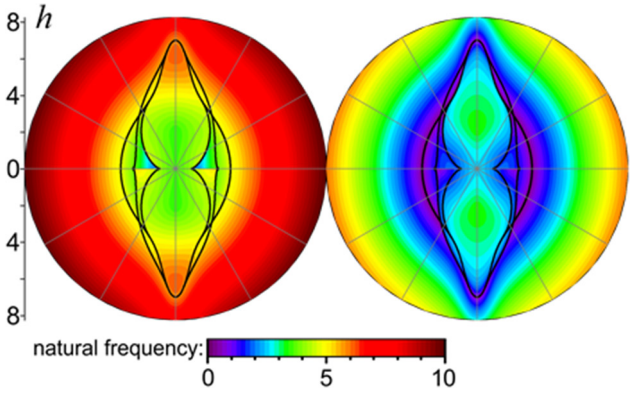

Figure 10. Map of natural frequencies of free oscillations with no ac field excitation, computed on the descending branch of MHL for $\alpha = 0.01$. The position of each point gives the applied dc field, while its colour gives the value of the corresponding natural frequency at which the system oscillate in the absence of a driving field, after the system is disturbed from its equilibrium state. The thin lines represent the static CCs.

Landau–Lifshitz–Gilbert (LLG) equations of the two layers, with the same configuration of the applied magnetic fields as used in experiment. The ac magnetic field acts along y axis (i.e. perpendicular to the easy axis), and the dc magnetic field acts in the xy plane, as shown in figure 8. The imaginary part χ'' of the complex magnetic susceptibility along the ac field is computed as the first harmonic of the normalized induced signal along the ac field direction. The energy absorbed from the ac field by the SAF system is proportional to the product $f_{ac}\chi''$, where f_{ac} is the ac field frequency. More details about complex susceptibility computation are presented in [34, 44–46]. The reversible susceptibility tensor can also be computed using the expressions obtained in [47] if the static equilibrium positions are known.

Because the demagnetizing fields play an important role in the operation of thin magnetic film devices, we have added in our simulations a phenomenological demagnetizing field perpendicular to the xy plane with the demagnetization factor $N_d = 0.5$.

We have simulated the χ'' field variation with the dc field applied at different orientations θ and have built the polar contour representations from figure 9. The ac field frequency $r = 2/3$ is normalized by the Kittel frequency $\gamma_0 H_k/2\pi$, where γ_0 is the gyromagnetic ratio. One observes a remarkable qualitative agreement between the experimental and simulated data. The locus of χ'' peaks coincides with the locus of absorption maxima, i.e. with the locus of the dc fields at which the resonance frequency of the system equals the excitation frequency, the resonance frequency being given by the curvature of the free energy surface and by the damping constant.

The map of calculated natural frequencies of oscillations with no ac field excitation for a damping constant $\alpha = 0.01$ after the system is disturbed from its equilibrium state, is shown in figure 10. When damping constant is small the resonant frequency is approximately equal to the unforced natural frequency of the system. As the frequency increases from zero, there are absorption curves given both by the first and second natural frequencies, the latter curves contracting toward the

hard axis (see $f_{ac} = 2.5$ and 3 cases in figure 9). Subsequently, further absorption curves given by the first natural frequency expand from the hard axis toward the static CC and then outside it. As the frequency increases even more, almost circular non-anisotropic resonant absorption curves are obtained, for which the free energy of the system is dominated by the external field energy.

5. Conclusion

In summary, static and dynamic properties of a FeCoB SAF structure have been used to characterize the anisotropy of the system in a manner reminiscent of the CC. While the CC provides information about the anisotropy through magnetization reversal in each layer, the presence of a microwave field requires a new model, as the CC characterization is no longer valid. We have therefore presented a simulation-supported experimental characterization in the dynamic regime which captures the FMR absorption properties of these multilayered systems.

Acknowledgments

Authors would like to acknowledge Dr Ganping Ju and Dr Erol Girt from Seagate Technology for providing the samples. DJA acknowledges support from the University of New Orleans Graduate School scholarship. LS thanks National Science Foundation for the support provided through the Independent Research and Development (IR/D) program.

ORCID iDs

Daniel J Adams https://orcid.org/0000-0003-1554-1427

References

[1] Byeon S C, Misra A and Doyle W D 2004 Synthetic antiferromagnetic soft underlayers for perpendicular recording media *IEEE Trans. Magn.* **40** 2386–8
[2] Kawato Y, Futamoto M and Nakamoto K 2005 Perpendicular magnetic recording medium and magnetic storage apparatus *Google Patents* 6926974 B2
[3] Pietambaram S V, Janesky J, Dave R W, Sun J J, Steiner G and Slaughter J M 2004 Exchange coupling control and thermal endurance of synthetic antiferromagnet structure for MRAM *IEEE Trans. Magn.* **40** 2619–21
[4] Khvalkovskiy A V *et al* 2013 Basic principles of STT-MRAM cell operation in memory arrays *J. Phys. D: Appl. Phys.* **46** 139601
[5] Savtchenko L, Engel B N, Rizzo N D, Deherrera M F and Janesky J A 2003 Method of writing to scalable magnetoresistance random access memory element *Google Patents* 6545906 B1
[6] Milyaev M, Naumova L, Chernyshova T, Proglyado V, Kamensky I and Ustinov V 2016 Spin-flop in synthetic antiferromagnet and anhysteretic magnetic reversal in FeMn-based spin valves *IEEE Trans. Magn.* **52** 2301104
[7] Jun H, Shoji I, Young Min L, Ryutaro S, Toshiyasu M, Fumihiro M, Hiromasa T and Hideo O 2006 Current-induced magnetization switching in MgO barrier based magnetic tunnel junctions with CoFeB/Ru/CoFeB synthetic ferrimagnetic free layer *Japan. J. Appl. Phys.* **45** L1057
[8] Apalkov D, Dieny B and Slaughter J M 2016 Magnetoresistive Random Access Memory *Proc. IEEE* **104** 1796–830
[9] Chernyshova T, Milyaev M A, Naumova L, Proglyado V V, Bannikova N, Maksimova I K, Petrov I A and Ustinov V 2017 Magnetoresistive sensitivity and uniaxial anisotropy of spin-valve microstrips with a synthetic antiferromagnet *Phys. Met. Metallography* **118** 415–20
[10] Devolder T, Couet S, Swerts J, Liu E, Lin T, Mertens S, Furnemont A and Kar G 2017 Annealing stability of magnetic tunnel junctions based on dual MgO free layers and [Co/Ni] based thin synthetic antiferromagnet fixed system *J. Appl. Phys.* **121** 113904
[11] Lapa P N, Khaire T, Ding J, Pearson J E, Novosad V, Hoffmann A and Jiang J S 2016 Spin valve with non-collinear magnetization configuration imprinted by a static magnetic field *AIP Adv.* **6** 056107
[12] Van Roosbroeck R, Van Roy W, Stakenborg T, Trekker J, D'Hollander A, Dresselaers T, Himmelreich U, Lammertyn J and Lagae L 2014 Synthetic antiferromagnetic nanoparticles as potential contrast agents in MRI *ACS Nano* **8** 2269–78
[13] Bi C, Almasi H, Price K, Newhouse-Illige T, Xu M, Allen S R, Fan X and Wang W 2017 Anomalous spin–orbit torque switching in synthetic antiferromagnets *Phys. Rev.* B **95** 104434
[14] Thiaville A 1998 Extensions of the geometric solution of the two dimensional coherent magnetization rotation model *J. Magn. Magn. Mater.* **182** 5–18
[15] Radu C, Cimpoesu D, Stancu A and Spinu L 2008 Measurement of the critical curve of a synthetic antiferromagnet *Appl. Phys. Lett.* **93** 022506
[16] Schrag B D, Anguelouch A, Xiao G, Trouilloud P, Lu Y, Gallagher W J and Parkin S S P 2000 Magnetization reversal and interlayer coupling in magnetic tunneling junctions *J. Appl. Phys.* **87** 4682–4
[17] Anguelouch A, Schrag B D, Xiao G, Lu Y, Trouilloud P L, Wanner R A, Gallagher W J and Parkin S S P 2000 Two-dimensional magnetic switching of micron-size films in magnetic tunnel junctions *Appl. Phys. Lett.* **76** 622–4
[18] Lu Y *et al* 1999 Observation of magnetic switching in submicron magnetic-tunnel junctions at low frequency *J. Appl. Phys.* **85** 5267–9
[19] Wernsdorfer W 2006 Classical and quantum magnetization reversal studied in nanometer-sized particles and clusters *Handbook of Advanced Magnetic Materials* ed Y Liu *et al* (Berlin: Springer) pp 77–127
[20] Radu C, Cimpoesu D, Girt E, Ju G, Stancu A and Spinu L 2007 Reversible susceptibility studies of magnetization switching in FeCoB synthetic antiferromagnets *J. Appl. Phys.* **101** 09D109
[21] Spinu L, Pham H, Radu C, Denardin J C, Dumitru I, Knobel M, Dorneles L S, Schelp L F and Stancu A 2005 Probing two-dimensional magnetic switching in Co/SiO_2 multilayers using reversible susceptibility experiments *Appl. Phys. Lett.* **86** 012506
[22] Fujiwara H W, Wang S Y and Sun M 2004 Magnetization behavior of synthetic antiferromagnet and toggle-magnetoresistance random access memory *Trans. Magn. Soc. Japan* **4** 121–9
[23] Fernandez-Pacheco A, Ummelen F C, Mansell R, Petit D, Lee J H, Swagten H J M and Cowburn R P 2014 Dynamic selective switching in antiferromagnetically-coupled bilayers close to the spin reorientation transition *Appl. Phys. Lett.* **105** 092405

[24] Kong Y C, Lim S H and Lee K J 2009 Ferromagnetic resonance frequency of a patterned synthetic antiferromagnet *J. Korean Phys. Soc.* **54** 1630–4
[25] Gonzalez-Chavez D E, Dutra R, Rosa W O, Marcondes T L, Mello A and Sommer R L 2013 Interlayer coupling in spin valves studied by broadband ferromagnetic resonance *Phys. Rev.* B **88** 104431
[26] Zhang Z, Zhou L, Wigen P E and Ounadjela K 1994 Angular dependence of ferromagnetic resonance in exchange-coupled Co/Ru/Co trilayer structures *Phys. Rev.* B **50** 6094–112
[27] Layadi A and Artman J O 1997 Study of antiferromagnetic coupling by ferromagnetic resonance (FMR) *J. Magn. Magn. Mater.* **176** 175–82
[28] Layadi A 2015 A theoretical investigation of ferromagnetic resonance linewidth and damping constants in coupled trilayer and spin valve systems *AIP Adv.* **5** 057113
[29] Lindner J, Kollonitsch Z, Kosubek E, Farle M and Baberschke K 2001 *In situ* detection of two ferromagnetic resonance modes in coupled Ni/Cu/Co/Cu(0 0 1) trilayer structures *Phys. Rev.* B **63** 094413
[30] Jin Q Y, Zhai H R, Xu Y B, Zhai Y, Lu M, Zhou S M, Payson J S, Dunifer G L, Naik R and Auner G W 1995 A study of interlayer coupling in Co/Cu multilayers *J. Appl. Phys.* **77** 3971–4
[31] Li S, 2016 Engineering optical mode ferromagnetic resonance in FeCoB films with ultrathin Ru insertion *Sci. Rep.* **6** 33349
[32] Backes D, Bedau D, Liu H, Langer J and Kent A D 2012 Characterization of interlayer interactions in magnetic random access memory layer stacks using ferromagnetic resonance *J. Appl. Phys.* **111** 07C721
[33] Pham H, Cimpoesu D, Plamada A-V, Stancu A and Spinu L 2009 Dynamic critical curve of a synthetic antiferromagnet *Appl. Phys. Lett.* **95** 222513
[34] Cimpoesu D, Ding J J, Stoleriu L, Adeyeye A, Stancu A and Spinu L 2013 Angular resonant absorption curves in magnetic nanowire arrays *Appl. Phys. Lett.* **102** 232401
[35] Slonczewski J C 1956 Theory of magnetic hysteresis in films and its applications to computers *Research Memorandum* R.M. 003.111.224 IBM Research Center Poughkeepsie
[36] Stoner E C and Wohlfarth E P 1948 A mechanism of magnetic hysteresis in heterogeneous alloys *Phil. Trans. R. Soc.* A **240** 599–642
[37] Adams D J, Khan M A, Poudyal P and Spinu L 2017 Angular dependence of resonant absorption in FeCoB synthetic antiferromagnets *AIP Adv.* **7** 056322
[38] Neudecker I, Woltersdorf G, Heinrich B, Okuno T, Gubbiotti G and Back C H 2006 Comparison of frequency, field, and time domain ferromagnetic resonance methods *J. Magn. Magn. Mater.* **307** 148–56
[39] Ding Y, Klemmer T J and Crawford T M 2004 A coplanar waveguide permeameter for studying high-frequency properties of soft magnetic materials *J. Appl. Phys.* **96** 2969–72
[40] Bilzer C, Devolder T, Crozat P, Chappert C, Cardoso S and Freitas P P 2007 Vector network analyzer ferromagnetic resonance of thin films on coplanar waveguides: comparison of different evaluation methods *J. Appl. Phys.* **101** 074505
[41] Głowiński H, Schmidt M, Gościańska I, Ansermet J-P and Dubowik J 2014 Coplanar waveguide based ferromagnetic resonance in ultrathin film magnetic nanostructures: impact of conducting layers *J. Appl. Phys.* **116** 053901
[42] Cimpoesu D, Stoleriu L and Stancu A 2013 Generalized Stoner–Wohlfarth model accurately describing the switching processes in pseudo-single ferromagnetic particles *J. Appl. Phys.* **114** 223901
[43] Chang H 1964 Coupled biaxial films *J. Appl. Phys.* **35** 770–1
[44] Spinu L, Cimpoesu D, Stoleriu L and Stancu A 2003 Micromagnetic calculation of the transverse susceptibility of patterned media *IEEE Trans. Magn.* **39** 2516–8
[45] Cimpoesu D, Stancu A, Dumitru I and Spinu L 2005 Micromagnetic simulation of the imaginary part of the transverse susceptibility *IEEE Trans. Magn.* **41** 3121–3
[46] Cimpoesu D, Stancu A and Spinu L 2007 Physics of complex transverse susceptibility of magnetic particulate systems *Phys. Rev.* B **76** 054409
[47] Cimpoesu D, Stancu A and Spinu L 2007 The reversible susceptibility tensor of synthetic antiferromagnets *J. Appl. Phys.* **101** 09D112

Temperature dependence of exchange bias in $(NiFe/IrMn)_n$ multilayer films studied through static and dynamic techniques

Daniel J. Adams,[1,2] Shankar Khanal,[1,2] Mohammad Asif Khan,[1,2] Artur Maksymov,[2] and Leonard Spinu[1,2,a]
[1]*Department of Physics, University of New Orleans, New Orleans, LA 70148, USA*
[2]*Advanced Materials Research Institute, University of New Orleans, New Orleans, LA 70148, USA*

(Presented 7 November 2017; received 22 September 2017; accepted 16 October 2017; published online 4 December 2017)

The in-plane temperature dependence of exchange bias was studied through both dc magnetometry and ferromagnetic resonance spectroscopy in a series of $[NiFe/IrMn]_n$ multilayer films, where n is the number of layer repetitions. Major hysteresis loops were recorded in the temperature range of 300 K to 2 K to reveal the effect of temperature on the exchange bias in the static regime while temperature-dependent continuous-wave ferromagnetic resonance for frequencies from 3 to 16 GHz was used to determine the exchange bias dynamically. Strong divergence between the values of exchange bias determined using the two different types of measurements as well as a peak in temperature dependence of the resonance linewidth were observed. These results are explained in terms of the slow-relaxer mechanism.
https://doi.org/10.1063/1.5006168

I. INTRODUCTION

The phenomenon of exchange bias discovered over 60 years ago[1] remains a topic of interest in applications and basic research. Marked by a shifted major hysteresis loop (MHL), exchange-biased systems display subtle properties requiring deeper exploration, including a non-monotonic variation of the ferromagnetic resonance (FMR) linewidth (ΔH) as a function of temperature. This property had been observed in rare-earth (RE)-doped iron garnets,[2–7] and a theory was developed by Teale and Tweedale[2] and Van Vleck and Orbach[8] based on earlier work of Galt[9] and Clogston,[10] describing a slow-relaxation due to the paramagnetic impurities.

The slow-relaxer theory was later adapted by McMichael *et al.*[11] and supported by Lubitz *et al.*[12] to explain these occurrences in exchange-biased systems, identifying the slow-relaxing impurities as antiferromagnetic grains. Others have suggested that the impurities are paramagnetic ions present at the interface of the ferromagnetic and antiferromagnetic layers.[13–15] In this work, the theory of paramagnetic ion relaxation is used to describe experimental observations.

II. EXPERIMENT

Three multilayer samples of $[Ni_{80}Fe_{20}$ (t nm)/IrMn (20 nm)$]_n$ were deposited on silicon wafers by the method described in Ref. 16. A 250 Oe magnetic field was applied in the plane of the samples during deposition to induce a magnetic anisotropy. The thickness of each antiferromagnetic layer in all samples was 20 nm. The thickness of ferromagnetic layers was adjusted between the samples

[a]Corresponding Author: Leonard Spinu (email: LSpinu@uno.edu)

according to the number of layers to hold the total sample thickness constant. Thickness of the individual ferromagnetic layers and number of repetitions across the samples are given by t = 20, 60, 80 nm and n = 10, 5, 4, and the samples are named S1, S2, S3, respectively (see Table 1 in Ref. 16). The samples were cut to similar sizes for experiments. Room temperature studies of these samples are presented in Refs. 16 and 17.

MHLs were measured along the exchange bias (H_{EB}) axis using a Quantum Design Magnetic Properties Measurement System (MPMS) in the temperature range 300 K to 2 K. In the dynamic regime, FMR was measured using a NanOsc CryoFMR spectrometer capable of broadband FMR by individually probing a continuous range of frequencies. Integration of CryoFMR with Quantum Design's Physical Properties Measurement System (PPMS) using a probe with a coplanar waveguide (CPW) allows for low-temperature FMR measurements. FMR was measured in the range 3 GHz to 16 GHz at temperatures from 300 K to 2 K in 25 K increments. The sample was placed on the CPW with microwave magnetic field perpendicular to the exchange bias and the dc field (H_{dc}) of the PPMS along the exchange bias, both fields in the plane of the films. H_{dc} was ramped from 3000 Oe to -3000 Oe while probing the transmission coefficient.

III. RESULTS AND DISCUSSION

The temperature-dependence of the MHLs is seen in Fig. 1 at selected temperatures, from which H_{EB} can be extracted. The similar coercivities between samples at room temperature but largely differing H_{EB} values are consistent with previous studies.[16] H_{EB} can be determined dynamically from the FMR measurements taking half of the sum of resonance fields, H_R, at a given frequency for fields along (0°) H_{EB} as well as antiparallel to (180°) H_{EB}.

Fig. 2 shows a comparison between the values of H_{EB} determined through FMR and MHL. Near room temperature, static and dynamic measurements produce similar values of H_{EB}. This agreement is broken for temperatures below 250 K. Static measurements yield an expected increase in the value of H_{EB} as temperature decreases which has been explained as temperature dependence of the number of grains contributing to H_{EB}.[14,18] FMR shows a gradual decrease in H_{EB} after reaching some peak value, the most obvious peak observed in the sample with the most layer repetitions. The difference in H_{EB} determined through static and dynamic techniques can be explained based on the results of Gloanec *et al.*[14,15]

Another feature of the FMR measurements is an increase of the linewidth (ΔH) as temperature decreases, leading to a broad peak which occurs for both 0° and 180°, as seen in Fig. 3. The clearest peak occurs in the sample with the highest number of repetitions. This feature is explained through the slow-relaxer mechanism as an anisotropic exchange field between the ferromagnet and the impurities.[8]

Reminiscent of the work of Teale and Tweedale for iron-garnets containing Yb,[2] we define a dynamic shift $S_D(\omega,T)$ (see Fig. 4 in Ref. 4) as,

$$|S_D(\omega,T)|_{EB} = |H_{EB}(0,T) - H_{EB}(\omega,T)| \tag{1}$$

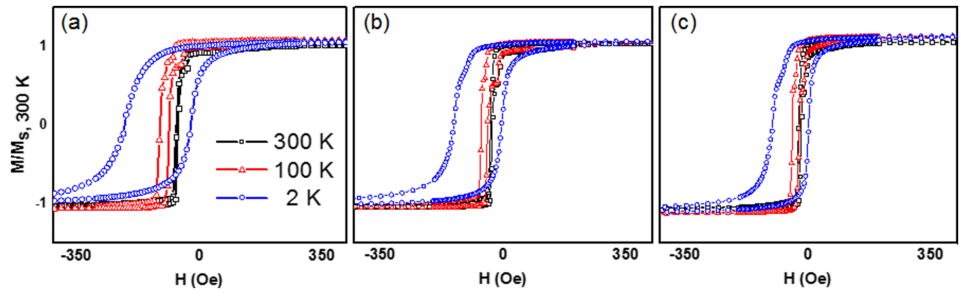

FIG. 1. MHLs at selected temperatures for (a) S1, (b) S2, and (c) S3.

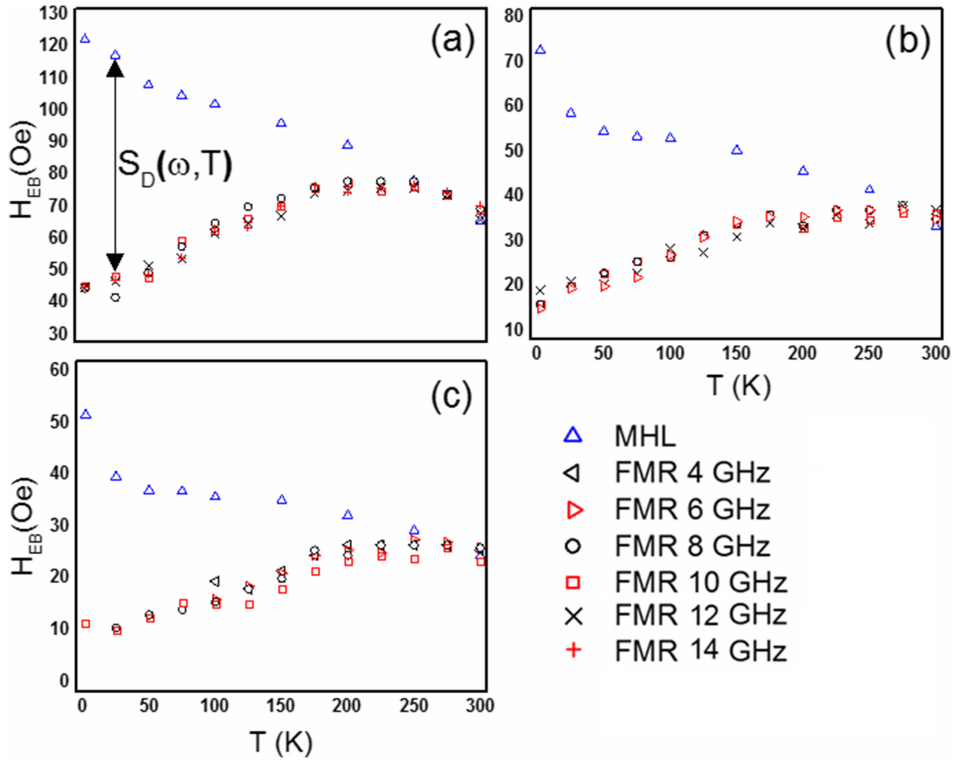

FIG. 2. Exchange bias as a function of temperature for (a) S1, (b) S2, and (c) S3 through MHL (blue triangles) and FMR. S_D is defined in Eq. (1).

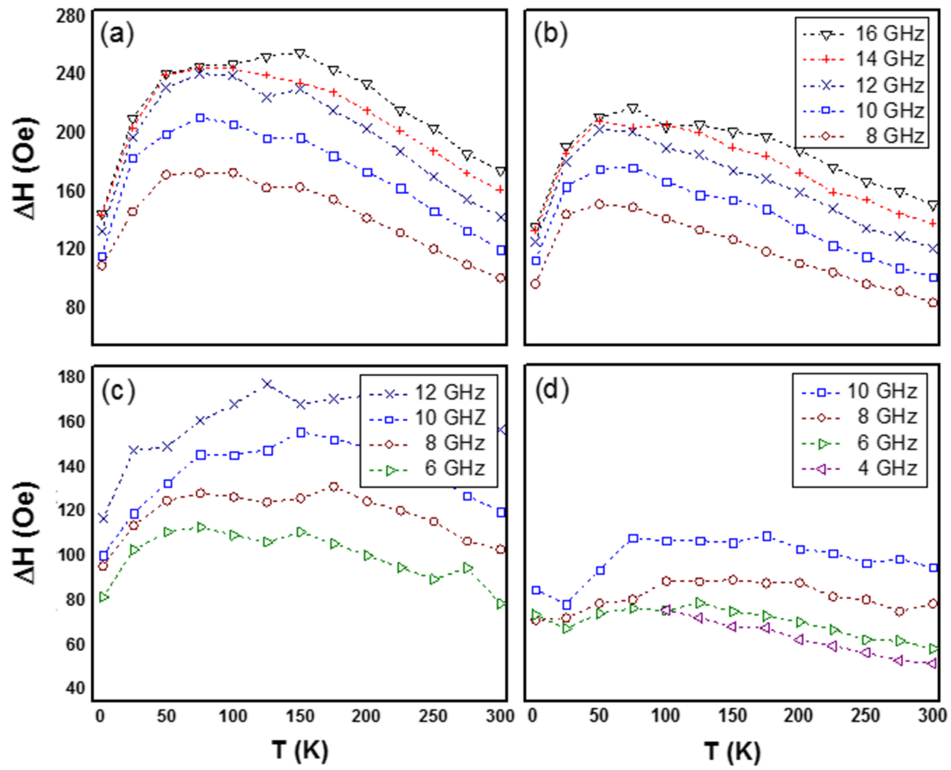

FIG. 3. ΔH as a function of temperature for S1 at (a) 0°, (b) 180°, (c) S2 at 0°, and (d) S3 at 180°.

where $H_{EB}(\omega,T)$ and $H_{EB}(0,T)$ are obtained through FMR and MHL, respectively. The field-shift is anisotropic, therefore affecting $H_{EB}(\omega,T)$ and likely causing the disagreement between the static and dynamic determinations of H_{EB}.

It has been shown that S_D and ΔH take the form

$$|S_D| \propto \frac{C}{2T} \frac{(\omega\tau)^2}{1+(\omega\tau)^2} \tag{2}$$

$$\Delta H \propto \frac{C}{T} \frac{\omega\tau}{1+(\omega\tau)^2} \tag{3}$$

where C is the impurity concentration, ω is the FMR frequency, T is temperature.[4,13] As these terms share constants of proportionality (see Eqs (1) and (2) in Ref. 4 or Eqs (3-16) and (3-17) in Ref. 10), it is clear that

$$\frac{2\,|S_D|}{\Delta H} = \omega\tau \tag{4}$$

where τ is the relaxation time. The ratio $2|S_D|/\Delta H$ is plotted in Fig. 4. The relaxation time

$$\tau = \tau_0 \tanh \frac{\delta}{kT} \tag{5}$$

is taken from Orbach's derivation of spin-lattice relaxation time,[19,20] and is used in fitting the data in Fig. 4. Of the suggested models, this seems to give the best fit, supporting the theory of slow relaxation by paramagnetic ions as suggested by others.[13–15] This model is consistent with that used in Refs. 14 and 15. Fits seen in Fig. 4(b) are examples of other suggested relaxation behaviors. The dotted red line corresponds to exponential dependence of τ from Néel[21] which would indicate slow relaxation of antiferromagnetic grains.[11,12] The solid red line is the thermal dependence suggested by Dubowik *et al.* who used the form $\tau \sim T^{-2}$, although for a more limited temperature range.[13] Based

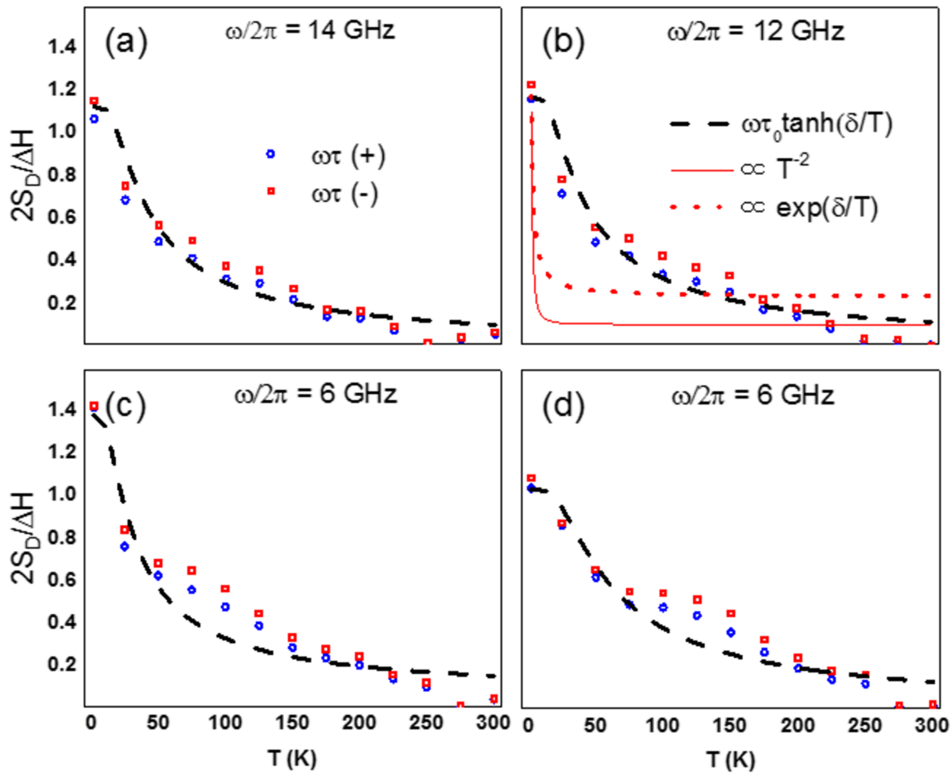

FIG. 4. Temperature dependence of $2|S_D|/\Delta H$ for (a,b) S1, (c) S2, and (d) S3 for $\theta = 0°$ (blue circles) and $\theta = 180°$ (red squares). Dotted black line corresponds to Eq. (4). Solid red and dashed red lines correspond to $\sim T^{-2}$ and $\sim \exp(\delta/T)$ respectively.

on these results, our work supports that the slow-relaxing impurities are paramagnetic ions at the surface boundaries.

It is clear that the model better fits S1 than S2 or S3. The subtle differences in the shape of the curve between samples can be expected since $\omega\tau$ is dependent on ΔH, which becomes flatter as number of layers in the sample is decreased. The fact that this fit is still imperfect may be attributed to difficulties in obtaining an accurate value for ΔH since the FMR spectra for these samples was somewhat asymmetric.

IV. CONCLUSION

In summary, our work gives support to one of the current theories of the slow-relaxer mechanism. We have investigated this model for multilayered samples, which to our knowledge, is the first study of this type to use samples other than bilayers. Another advantage of our study is that a wider range of FMR frequencies is probed. Other studies have been limited to smaller numbers of FMR frequencies, with many using only an X-band frequency between 9 and 10 GHz. The signatures of the slow-relaxation mechanism, namely, enhanced ΔH at low temperature and peak below 100 K and an anisotropic shift are most apparent in the sample with most repetitions and therefore the highest number of surface boundaries, i.e. more possible sites for paramagnetic ions to act as impurities.

ACKNOWLEDGMENTS

D.J.A. and L.S. thank NanOsc Instruments AB for providing the CryoFMR option used for FMR measurements in this work. D.J.A acknowledges support from the University of New Orleans Graduate School scholarship. LS thanks National Science Foundation for the support through the Independent Research and Development Program.

[1] W. H. Meiklejohn and C. P. Bean, Physical Review **102**(5), 1413–1414 (1956).
[2] R. W. Teale and K. Tweedale, Physics Letters **1**(7), 298–300 (1962).
[3] B. H. Clarke, R. F. Pearson, R. W. Teale, and K. Tweedale, J. Appl. Phys. **34**(4), 1269–1270 (1963).
[4] B. H. Clarke, K. Tweedale, and R. W. Teale, Physical Review **139**(6A), A1933–A1943 (1965).
[5] R. C. LeCraw, W. G. Nilsen, J. P. Remeika, and J. H. Van Vleck, Phys. Rev. Lett. **11**(11), 490–493 (1963).
[6] E. G. Spencer, J. P. Remeika, and P. V. Lenzo, Appl. Phys. Lett. **4**(10), 171–172 (1964).
[7] J. F. Dillon and J. W. Nielsen, Phys. Rev. Lett. **3**(1), 30–31 (1959).
[8] J. H. Van Vleck and R. Orbach, Phys. Rev. Lett. **11**(2), 65–67 (1963).
[9] J. K. Galt, W. A. Yager, and F. R. Merritt, Physical Review **93**(5), 1119–1120 (1954).
[10] A. M. Clogston, Bell Sys. Tech. Journal **34** (1955).
[11] R. D. McMichael, C. G. Lee, M. D. Stiles, F. G. Serpa, P. J. Chen, and W. F. Egelhoff, Jr., J. Appl. Phys. **87**(9), 6406–6408 (2000).
[12] P. Lubitz, M. Rubinstein, J. J. Krebs, and S.-F. Cheng, J. Appl. Phys. **89**(11), 6901–6903 (2001).
[13] J. Dubowik, F. Stobiecki, I. Gościańska, Y. P. Lee, A. Paetzold, and K. Röll, Eur. Phys. J. B **45**(2), 283–288 (2005).
[14] M. Gloanec, S. Rioual, B. Lescop, R. Zuberek, R. Szymczak, P. Aleshkevych, and B. Rouvellou, Physical Review B **80**(22), 220404 (2009).
[15] M. Gloanec, S. Rioual, B. Lescop, R. Zuberek, R. Szymczak, P. Aleshkevych, and B. Rouvellou, Physical Review B **82**(14), 144433 (2010).
[16] S. Khanal, A. Diaconu, J. M. Vargas, D. R. Lenormand, C. Garcia, C. A. Ross, and L. Spinu, J. Phys. D-Appl. Phys. **47**(25), 255002 (2014).
[17] R. Gallardo, S. Khanal, J. Vargas, L. Spinu, C. Ross, and C. Garcia, "Angular dependent FORC and FMR of exchange-biased NiFe multilayer films" (2016).
[18] T. Gredig, I. N. Krivorotov, and E. D. Dahlberg, Physical Review B **74**(9), 094431 (2006).
[19] R. Orbach, Proceedings of the Royal Society of London. Series A. Mathematical and Physical Sciences **264**(1319), 458–484 (1961).
[20] R. Orbach, J. Appl. Phys. **33**(6), 2144 (1962).
[21] L. Neel, Ann. Geophys **5** (1949).

Angular dependence of resonant absorption in FeCoB synthetic antiferromagnets

Daniel J. Adams, Mohammad Asif Khan, Pratik Poudyal,
and Leonard Spinu
Department of Physics and Advanced Materials Research Institute, University of New Orleans, New Orleans, Louisiana 70148, USA

(Presented 3 November 2016; received 21 September 2016; accepted 26 November 2016; published online 1 March 2017)

Magnetization dynamics in a series of FeCoB/Ru/FeCoB coupled samples were investigated using a critical-curve-like approach through angular dependent broadband microwave absorption spectroscopy. Two samples were selected in this study, with ferromagnetic and antiferromagnetic coupling between the FeCoB layers. The dynamic critical curves (DCC) were obtained by systematically probing the angular-dependent FMR absorption at selected frequencies for both samples to show the effect of layer coupling both as a function of frequency and of angle. The DCC representation has the advantage of offering a direct and complete visual representation of anisotropy, interactions, and magnetization dynamics effects. The DCC is compared with static critical curve measured using a reversible susceptibility experiment. [http://dx.doi.org/10.1063/1.4977881]

I. INTRODUCTION

Magnetically-coupled thin films have received much attention due to their importance in technological applications, and synthetic antiferromagnets (SAF) are of particular interest. Due to shape anisotropy, thermal stability,[1–4] controllable coupling strength and capacity for spin transfer,[5] SAF has applications in magnetic sensors,[6] perpendicular recording media,[7,8] exchange coupled composite media,[9] and MRAM cells.[4,10,11] The use of SAF in such applications is dependent on its interlayer exchange coupling, which determines the individual magnetic reversal of the ferromagnetic layers.[12]

With the goal of shrinking device dimensions, such structures are often two-dimensional, with interesting properties, such as magnetization switching, studied in the plane of the sample. Layer switching in SAF structures has been extensively characterized using the concept of critical curves (CC)[12–14] which is the locus of in-plane fields at which the irreversible magnetization reversal occurs. The method previously proposed to determine experimentally the CC in SAF is based on reversible susceptibility experiments and provides the static picture of the switching fields. The behavior of magnetization switching is critically dependent on the time scale,[15] and it is very important to characterize SAF in conditions similar to the ones in which they are operating in devices. A few studies explored SAF high-frequency properties through ferromagnetic resonance (FMR) spectroscopy.[16,17] However, these studies were limited in exploring the magnetization dynamics only along a particular direction, usually the easy axis. Recently, we proposed a method to characterize the magnetization dynamics in arrays of magnetic nanowires using a critical-curve-like approach through angular dependent microwave absorption spectroscopy.[18] This representation has the advantage of offering a direct and complete visual representation of anisotropy, interactions, and magnetization dynamics effects. In this paper we propose to use the same approach to experimentally measure the dynamic critical curves (DCC) of a series of FeCoB/Ru/FeCoB coupled samples.

II. EXPERIMENT

A series of trilayer films of FeCoB/Ru/FeCoB with a protective layer of C were deposited on glass disks at room temperature using dc magnetron sputtering with a base vacuum pressure below 3×10^{-9} Pa, such that the full thickness of the three-layer samples was approximately 30 nm. The thickness of the Ru spacer which would provide the coupling, t_{Ru}, was systematically varied from 0.8 to 2.0 nm among the samples. As a result, some of the samples produced in this series were ferromagnetically-coupled while others displayed antiferromagnetic coupling. Each sample was cut in squares of 5 mm × 5 mm. To contrast ferromagnetically- and antiferromagnetically-coupled structures, we chose to focus on two samples, $t_{Ru} = 0.8$ nm and $t_{Ru} = 1.6$ nm, which we called R08 and R16, respectively.

Major hysteresis loops (MHL) were measured for both samples using a vibrating sample magnetometer (VSM) in order to identify an easy axis and the type of coupling present. Broadband FMR absorption was then measured along the easy axis using a coplanar waveguide (CPW) in the range 0.5 – 8 GHz by measuring the S_{21} transmission parameter through the CPW using a vector network analyzer (VNA).

Systematic, angular-dependent FMR absorption was then measured at selected frequencies for both samples to show the effect of layer coupling both as a function of frequency and of angle. The rf magnetic field of the CPW was directed along the sample's hard axis, while the dc magnetic field was applied in the plane of the sample at a sequence of angles θ relative to the easy axis. For each angle, the applied dc magnetic field was ramped down starting from positive saturation, and the S_{21} parameter was measured at each field increment. These measurements were then repeated for different θ in increments of 5° for a full 360° characterization.

The static critical curves for SAF were obtained by probing the susceptibility for different dc fields applied in the plane of the thin film using the same tunnel diode oscillator (TDO) method proposed in reference 12. The samples under study were placed in a sensing coil such that the coil axis was perpendicular to the easy axis, with both the ac and dc magnetic fields in the plane of the sample. The susceptibility signal was recorded for different orientations of the dc field from 0° to 180° with respect to the easy axis in 2° increments, while the sensing coil remained fixed in place. The dc field was ramped down from positive saturation, and then up from negative saturation while the susceptibility was recorded as a function of field. From both measurements, ramp-down and ramp-up, a complete 360° characterization can be obtained.

III. RESULTS AND DISCUSSION

It is observed in Fig. 1 that the splitting of the broadband signature in the SAF is directly related to the separation of the MHL, and the frequency range at which the broadband curve is affected by the antiferromagnetic coupling is evident. A schematic of the sample on the CPW is shown in Fig. 2 for the broadband measurement (θ=0), as well as all further FMR measurements. A clearer look at this "splitting region" is seen in Fig. 3, which shows the FMR absorption in each sample for several continuous-wave (CW) frequencies with the dc field applied along the easy axis. These graphs can be thought of as slices taken horizontally from the broadband curves of Fig. 1. Comparing R16 to R08, one can see the effect of the coupling between the FeCoB layers on the absorption of lower frequencies, while the resonant absorption becomes more comparable between the two samples at higher frequencies.

Fig. 4 shows the angular dependence of FMR for the two samples at selected frequencies. All of the information provided by the measurements is contained in compact polar contour representations which completely characterizes the anisotropy of the system. The lower frequency scans show the obvious differences between the two samples, with coupling effects evident between the major branches of the absorption curves. A superimposed x-axis on the figure indicates the easy axis. As before, a horizontal slice taken from any one of the polar charts across this axis corresponds to a slice taken from the easy-axis broadband curve of Fig. 1 at that particular frequency. In both samples, the polar contour takes on a more circular shape at higher frequencies. Virtually no difference between samples is observed in the 5 GHz scan, which can be expected based on the 5 GHz scan seen in Fig. 3.

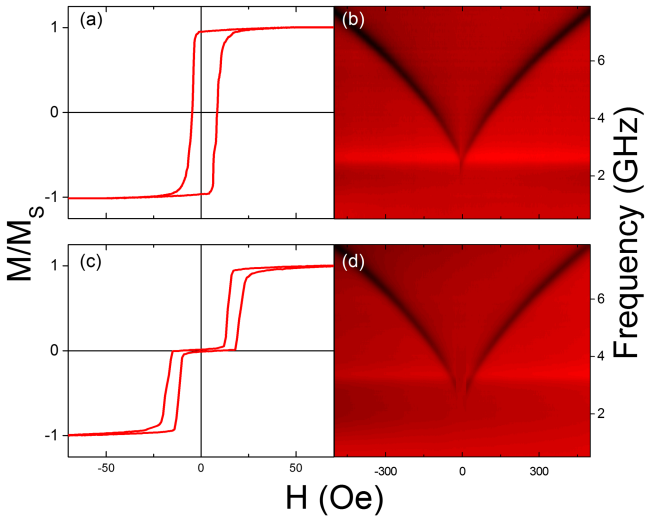

FIG. 1. MHLs (left) and broadband FMR (right) for (a, b) R08, and (c, d) R16.

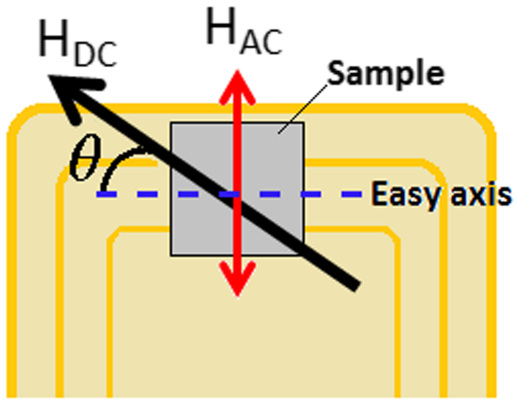

FIG. 2. Schematic representation of the geometry of the ac and dc magnetic fields relative to the easy axis of the sample.

An advantage of this representation is that FMR absorption can be compared to the static CC, as in Fig. 5. For SAF, the CC contains two envelopes.[13] The outermost envelope describes the saturation field, in which both layers have a magnetization parallel to one another while the inner contains the critical fields for switching. When compared to the polar FMR representation, it is evident how the DCC evolves from the static CC, with the lowest frequency DCC taking on a similar shape to the CC. This result is consistent with one of our previous papers,[19] which shows theoretically that

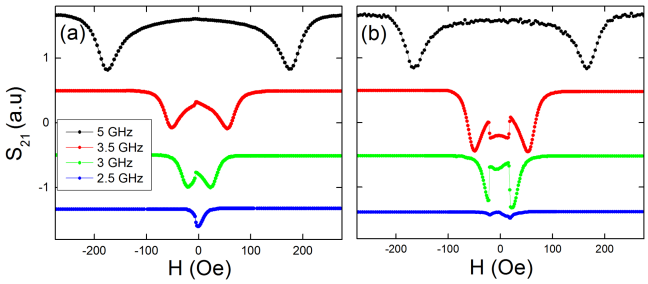

FIG. 3. CW FMR signals at different frequencies for (a) R08, and (b) R16.

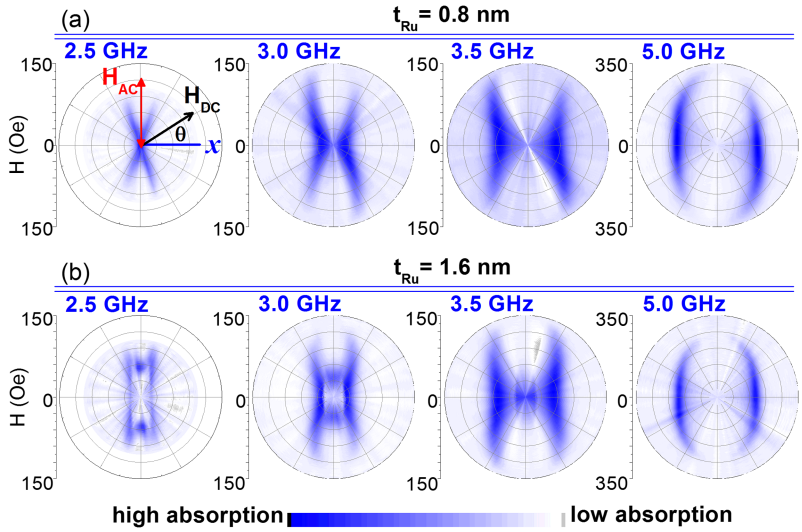

FIG. 4. Polar contour graphs of experimental CW FMR measurements for different frequencies and t_{Ru} for (a) R08, and (b) R16. For all samples, the easy axis is directed along the indicated x-direction.

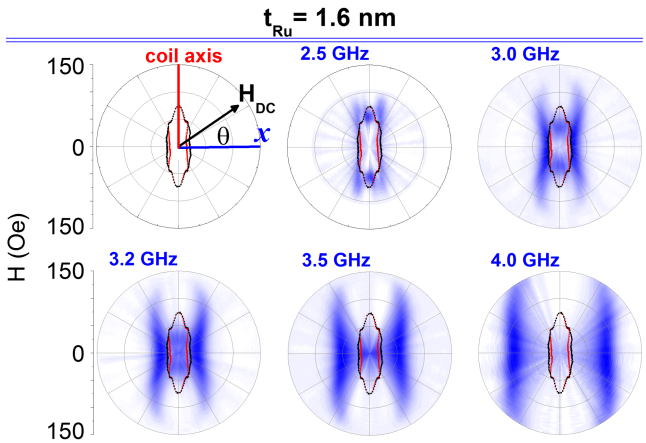

FIG. 5. SAF static critical curve obtained by TDO compared to the dynamic critical curve for several frequencies.

susceptibility is the zero-frequency-limit of FMR. The anisotropy observed in the static case is also preserved in the dynamic case.

IV. CONCLUSION

In this work, we report an alternative method to characterize the anisotropy in coupled magnetic systems. This is based on the variation of FMR along different directions in the plane of the sample. We show that our FMR curve can be compared to the CC constructed by susceptibility measurements along different directions. Our method therefore gives a DCC by accounting for FMR.

ACKNOWLEDGMENTS

We would like to acknowledge Dr. Ganping Ju and Dr. Erol Girt from Seagate Technology for providing the samples as well as Dr. Dorin Cimpoesu for his helpful input and advice on this project.

[1] H. He, Z. Z. Zhang, B. Ma, and Q. Y. Jin, IEEE Trans. Magn. **46**(6), 1327–1330 (2010).
[2] M. A. Milyaev, L. I. Naumova, V. V. Proglyado, T. A. Chernyshova, D. V. Blagodatkov, I. Y. Kamenskii, and V. V. Ustinov, Phys. Metals Metallogr. **116**(11), 1073–1079 (2015).
[3] Z. R. Tadisina, S. Gupta, P. LeClair, and T. Mewes, J. Vac. Sci. Technol. A **26**(4), 735–738 (2008).
[4] S. V. Pietambaram, J. Janesky, R. W. Dave, J. J. Sun, G. Steiner, and J. M. Slaughter, IEEE Trans. Magn. **40**(4), 2619–2621 (2004).
[5] N. C. Emley, F. J. Albert, E. M. Ryan, I. N. Krivorotov, D. C. Ralph, R. A. Buhrman, J. M. Daughton, and A. Jander, Appl. Phys. Lett. **84**(21), 4257–4259 (2004).
[6] A. Veloso and P. P. Freitas, J. Appl. Phys. **87**(9), 5744–5746 (2000).
[7] S. C. Byeon, A. Misra, and W. D. Doyle, IEEE Trans. Magn. **40**(4), 2386–2388 (2004).
[8] Y. Kawato, M. Futamo, and K. Nakamoto, patent No. US2002/0 028 356 A1.
[9] S. Hernandez, M. Kapoor, and R. H. Victora, Appl. Phys. Lett. **90**(13), 3 (2007).
[10] A. V. Khvalkovskiy, D. Apalkov, S. Watts, R. Chepulskii, R. S. Beach, A. Ong, X. Tang, A. Driskill-Smith, W. H. Butler, P. B. Visscher, D. Lottis, E. Chen, V. Nikitin, and M. Krounbi, J. Phys. D-Appl. Phys. **46**(7), 20 (2013).
[11] L. Savtchenko, B. N. Engel, N. D. Rizzo, M. F. Deherrera and J. A. Janesky (Google Patents, 2003).
[12] C. Radu, D. Cimpoesu, A. Stancu, and L. Spinu, Appl. Phys. Lett. **93**(2), 3 (2008).
[13] H. Fujiwara, S. Y. Wang, and M. Sun, Transactions of the Magnetics Society of Japan **4**, 121–129 (2004).
[14] C. Radu, D. Cimpoesu, E. Girt, G. P. Ju, A. Stancu, and L. Spinu, J. Appl. Phys. **101**(9), 3 (2007).
[15] H. Pham, D. Cimpoesu, A. V. Plamada, A. Stancu, and L. Spinu, Appl. Phys. Lett. **95**(22), 222513 (2009).
[16] Y. C. Kong, S. H. Lim, and K. J. Lee, J. Korean Phys. Soc. **54**(4), 1630–1634 (2009).
[17] D. E. Gonzalez-Chavez, R. Dutra, W. O. Rosa, T. L. Marcondes, A. Mello, and R. L. Sommer, Physical Review B **88**(10) (2013).
[18] D. Cimpoesu, J. J. Ding, L. Stoleriu, A. Adeyeye, A. Stancu, and L. Spinu, Appl. Phys. Lett. **102**(23), 5 (2013).
[19] L. Spinu, I. Dumitru, A. Stancu, and D. Cimpoesu, Journal of Magnetism and Magnetic Materials **296**(1), 1–8 (2006).